ABSTRACT

Title of Dissertation	COVARIABILITY OF WINTER AND SUMMER PRECIPITATION IN CENTRAL AMERICA AND MEXICO WITH TROPICAL SEA SURFACE TEMPERATURES UNDER A WARMING CLIMATE
	Yutong Pan, Doctor of Philosophy, 2025
Dissertation directed by	Professor Ning Zeng Department of Atmospheric and Oceanic Science

This dissertation investigates the influence of tropical sea surface temperatures (SSTs) on precipitation variability and the regional hydrological cycle in Central America and Mexico (CAM), focusing on both winter and summer. As global climate change progresses, the understanding of how tropical SSTs affect regional precipitation patterns has become crucial for improving seasonal climate predictions and assessing future climate risks. The study examines the relationships between CAM precipitation and tropical SSTs, with particular attention to the contributions of the Pacific and Atlantic Oceans. Through a combination of historical observational data, atmospheric model simulations, and climate projections, the research identifies significant covariability between CAM precipitation and tropical SSTs during both the winter and summer seasons. In the winter, ENSO-related SSTs in the Pacific and warming trends in the Atlantic Ocean are shown to modulate precipitation patterns, with both oceans contributing to precipitation variability. In summer, tropical SST warming, particularly in the Atlantic, is found to dominate precipitation variability, while ENSO still plays a secondary role. A key feature of CAM's seasonal cycle, the mid-summer drought (MSD), is characterized in detail, revealing its sensitivity to both ENSO events and long-term trends. Future projections from climate models suggest a warmer, drier future for the region, with reductions in precipitation, soil moisture, and runoff, exacerbating challenges related to water resources and agriculture. The dissertation concludes that tropical SSTs, especially in the Pacific and Atlantic, are critical drivers of CAM precipitation and provides valuable insights for improving seasonal climate predictions. Further research is recommended to refine regional climate models, explore long-term trends in precipitation patterns, and better understand the socio-economic implications of projected hydrological changes.

COVARIABILITY OF WINTER AND SUMMER PRECIPITATION IN CENTRAL AMERICA AND MEXICO WITH TROPICAL SEA SURFACE TEMPERATURES UNDER A WARMING CLIMATE

by

Yutong Pan

Dissertation submitted to the Faculty of the Graduate School of the
University of Maryland, College Park, in partial fulfillment
of the requirements for the degree of
Doctor of Philosophy
2025

Advisory Committee:
Professor Ning Zeng, Chair/Advisor
Professor E. Hugo Berbery
Professor James A. Carton
Professor Da-Lin Zhang
Dr. Zeng-Zhen Hu
Associate Professor Kuishuang Feng, Dean's Representative

Acknowledgements

I would like to express my deepest gratitude to my advisor, Prof. Ning Zeng, for his invaluable guidance, unwavering support, and insightful advice throughout my Ph.D. journey. His patience and encouragement have been instrumental in shaping both my research and professional growth.

I am also sincerely grateful to my dissertation committee members, Prof. Hugo Berbery, Prof. Jim Carton, Prof. Da-Lin Zhang, Dr. Zeng-Zhen Hu, and Prof. Kuishuang Feng, for their constructive feedback and support, which have significantly enhanced the quality of this work.

Special thanks go to Graduate Program Director Prof. Jonathan Poterjoy, Assistant Program Director Mrs. Tammy Hendershot, and Prof. Sumant Nigam in the Department of Atmospheric and Oceanic Science at the University of Maryland, and Dr. Annarita Mariotti at the NOAA Climate Program Office, for their immense help and support throughout this process.

I extend my heartfelt appreciation to my family for their unconditional love and support. Their endless encouragement and belief in me have been my greatest motivation and a constant source of strength.

This dissertation is dedicated to all those who have supported me on this journey. Thank you!

Table of Contents

List of Tables

List of Figures

Figure 4.5 Winter (DJF) circulation anomalies of (a, b) 200-hPa height (shading, gpm) and vorticity (contour, s^{-1}), (c, d) 850-hPa wind (vector, m s^{-1}), and 925-hPa divergence (contour, s^{-1}) associated with one standard deviation of the SVD SST time series. The anomalies are obtained through linear regression against the SVD SST time series (red bars in Figure 4.2) for (a, c) mode 1 and (b, d) mode 2 using observational data. The contour interval in (a, b) is 1.0×10^{-6} s^{-1}, with negative values dashed. The contour interval in (c, d) is 2.0×10^{-7} s^{-1}, with positive values in red, negative values in blue, and the zero contour in thick black. The height anomalies circled by red (positive) and blue (negative) lines in (a, b) are significantly correlated with the SVD SST time series at the 99% confidence level.

Figure 4.6 Winter (DJF) 200-hPa stream function anomalies (units: 10^6 m^2 s^{-1}) associated with one standard deviation of the SVD SST time series for (a) mode 1 and (b) mode 2. The anomalies are obtained through linear regression against the SVD SST time series (red bars in Figure 4.2) using observational data. The stream function anomalies circled by red (positive) and blue (negative) lines are significantly correlated with the SVD SST time series above the 99% confidence level.

Figure 4.7 Winter (DJF) 200-hPa velocity potential anomalies (shadings, units: 10^6 m) and divergent wind anomalies (vectors, units: m s^{-1}) associated with one standard deviation of the SVD SST time series for (a) mode 1 and (b) mode 2. The anomalies are obtained through linear regression against the SVD SST time series (red bars in Figure 4.2) using observational data. The divergence anomaly field is also shown based on the divergent wind anomalies, with a contour interval of 2 × 10-7 s-1. Positive divergence anomalies are represented by thick red contours, negative anomalies by thick blue contours, and zero divergence by thin gray contour.

Figure 4.8 Homogeneous correlation maps of (a, b) the first and (c, d) second SVD modes between (a, c) winter (DJF) SST in the tropical Pacific and Atlantic and (b, d) precipitation in CAM based on the 18-member ensemble mean AMIP simulations from 1957 to 2018. The correlations, shown in shadings (> 0.3), are statistically significant above the 99% confidence level. The percentage of total variance explained by each mode for SST (a, c) and precipitation (b, d) is displayed in the top right corner of each panel. The green box in (a, c) highlights the tropical Pacific and Atlantic regions where SST data are used in the SVD analysis.

Figure 4.9 Normalized SVD time series of winter (DJF) SST (red bars) and precipitation (green bars) for (a) the first and (b) second modes from the 18-member ensemble mean data of the 1957–2018 AMIP simulations. The correlation (R) between each pair of SVD time series is displayed at the top of each panel.

Figure 4.10 Anomaly correlation between observed 1948–2024 DJF precipitation and reconstructed precipitation anomalies based on (a) SVD mode 1 SST time series, (b) SVD

indicate individual model members, and pink shading represents one standard deviation of the inter-member spread around the MME means.

Figure 7.13 CAM domain-averaged total runoff anomalies (units: %) relative to the 1980–2005 climatology, from 1865 to 2095 for (a, b) winter and (c, d) summer. Panels (a) and (c) show the CMIP5 MME means (red lines), while panels (b) and (d) display the CMIP6 MME means (red lines). CNRM observations are represented by black lines. Gray lines indicate individual model members, and pink shading represents one standard deviation of the inter-member spread around the MME means.

List of Abbreviations

AMIP	Atmospheric Model Intercomparison Project
CAM	Central America and Mexico
CFS	Climate Forecast System
CFSR	Climate Forecast System Reanalysis
CMIP5	Coupled Model Intercomparison Project Phase 5
CMIP6	Coupled Model Intercomparison Project Phase 6
CNRM	National Centre for Meteorological Research
CPC	Climate Prediction Center
CRU	Climate Research Unit
DJF	December, January, and February
EOF	Empirical Orthogonal Function
ENSO	El Niño–Southern Oscillation
ERSSTv5	Extended Reconstructed SST version 5
ESM	Earth System Model
ET	Evapotranspiration
GFS	Global Forecast System
HadCRUT4	Met Office Hadley Centre and CRU
HadISST	Hadley Centre Sea Ice and SST
ITCZ	Intertropical Convergence Zone
JJA	June, July, and August
MME	Multi-Model Ensemble
MSD	Mid-summer drought
NAO	North Atlantic Oscillation
NCAR	National Center for Atmospheric Research
NCEP	National Centers for Environmental Prediction
NOAA	National Oceanic and Atmospheric Administration

ONI	Oceanic Niño Index
PC	Principal Component
RCP	Representative Concentration Pathway
PREC/L	Precipitation Reconstruction over Land
R1	NCEP–NCAR Reanalysis
SSP	Shared Socioeconomic Pathway
SST	Sea Surface Temperature
SVD	Singular Value Decomposition
WMO	World Meteorological Organization

Chapter 1: Introduction

1.1 Background

Since the beginning of the 21st century, widespread droughts have repeatedly struck Central America, resulting in severe social and economic consequences (Robjhon and Thiaw 2015; Steffens 2018, McGillivray and Salisbury 2023). Reports from the United Nations (e.g., OCHA 2014; Fion 2018; UNDRR 2024) indicate that more than two million people in the region are at the risk of food insecurity due to crop failures caused by these droughts. United Nations agencies, including the Food and Agriculture Organization and the World Food Programme, along with the U.S. Government, have expressed particularly concern about the drought's effect on migration patterns (e.g., Barrett 2019; Angelo 2022; Linke et al. 2023). It is argued that the ongoing food security crisis in Honduras, Guatemala, and El Salvador, driven by droughts and water shortages, may be a primary factor behind the current migration from Central America to the United States.

Further to the north, Mexico has also been experiencing a prolonged drought (e.g., Salazar and Rodriguez 2011; Bnamericans 2016; Thiem 2024), which has led to a 40% reduction in the country's agricultural production (e.g., Rodriguez 2012). Additionally, water supplies in Mexico are becoming increasingly strained due to the combined effects of drought and population growth (Climate Reality 2018; Wagner et al. 2024). The ongoing drought in Central America and Mexico (CAM) raises an important question: what are the contributing factors driving the drought in the CAM region?

1.2 Motivation

Sea surface temperatures (SSTs) in the surrounding oceans have been identified as key factors influencing precipitation patterns in CAM (e.g., Cavazos and Hastenrath 1990; Enfield

1996; Enfield and Alfaro 1999; Pavia et al. 2006; Karnauskas and Busalacchi 2009; Mendez and Magana 2010; Bhattacharya and Chiang 2014; Wright et al. 2022), with the El Niño–Southern Oscillation (ENSO) in the tropical Pacific and SSTs in the tropical Atlantic being particular important. The former plays a major role in modulating interannual variability in CAM precipitation (e.g., Giannini et al. 2000), while the latter is associated with climate variability on timescales ranging from interannual to multi-decadal (e.g., Handoh et al. 2006; Enfield et al. 2001; Ting et al. 2011), as well as serving as a proxy for global warming in future climate projections for the CAM region (e.g., Fuentes-Franco et al. 2015).

The relationship between CAM precipitation and Pacific SSTs has been well documented in previous studies. It is well-established that winter precipitation across most of Mexico tends to be above normal during El Niño events and below normal during La Niña events, while precipitation anomalies in Central America generally show the opposite trend (e.g., Cavazos and Hastenrath 1990; Magana et al. 2003; Seager et la. 2009). For example, the 2015 El Niño event, the strongest warm event of the 21st century, was identified as a key driver of a new drought following the 2014 drought in Central America (Fion 2018). Studies also highlight different effects of ENSO on CAM precipitation during winter and summer seasons (e.g., Bravo-Cabrera et al. 2017).

In addition to the Pacific SSTs, there is a strong association between CAM precipitation and Atlantic SSTs (e.g., Enfield 1996; Enfield and Alfaro 1999; Taylor et al. 2002). However, most studies have focused on the influence of the Atlantic SSTs at the interannual timescale. In recent decades, the warming of the tropical Atlantic, especially at the basin-wide level, has been closely linked to global warming (Wang and Dong 2010). Global warming has accelerated in recent years, with 2024 being the hottest year on record (Igini 2024; Bateman 2025). According to the World Meteorological Organization (WMO, 2025), the years 2015–2024 have been the warmest ten years on record.

Given that all of the warmest years have occurred in the past decade, it remains unclear how the ongoing warming of Atlantic SSTs, driven by global climate change, is affecting precipitation in CAM, particularly in relation to the recent droughts. From a historical perspective, it is also crucial to assess the relative importance of SSTs in the tropical Pacific versus the tropical Atlantic in driving CAM precipitation variability, particularly as Atlantic SSTs are increasingly influenced by the long-term warming trend.

Another important issue related to precipitation variability and water availability in CAM is the regional hydrological cycle. The region is characterized by a diverse range of climate regimes, including semi-arid, monsoon, and tropical rainforest climates (Durán-Quesada et al. 2010), leading to geographically and seasonally variable water cycles. While previous studies have examined climate change projections for CAM (e.g., Karamalkar et al. 2011; Lyra et al. 2017; Imbach et al. 2018), none have explicitly addressed the implications for the regional hydrological cycle. Mariotti et al. (2015) demonstrate that hydrological cycle is a key process for understanding climate change projections in the Mediterranean region. Similarly, this study will use a comparable approach to analyze the changes in the water cycle in CAM under global warming.

1.3 Objectives

The primary goal of this dissertation is to understand how tropical SSTs under a warming climate influence precipitation variability and the hydrological cycle in CAM. Specifically, the study will explore the following objectives:

1. To quantify the relationships between CAM precipitation and tropical SSTs during the winter and summer based on historical observations.

2. To determine the relative importance of tropical Pacific and Atlantic SSTs to the variability of CAM precipitation, with particular focus on the contribution of the Atlantic SST warming trend associated with global warming.
3. To characterize the seasonality of the relationships between CAM precipitation and tropical SSTs.
4. To investigate the relationships between CAM precipitation and tropical SSTs by examining the associated atmospheric circulation in observations and reproducing these observed relationships in SST-forced simulations using an atmospheric model.
5. To characterize the mid-summer drought in CAM and its climate variability.
6. To assess projected changes in CAM precipitation and the regional hydrological cycle by comparing present-day climate simulations with future climate projections using coupled global climate models.

This dissertation is primarily focused on describing and understanding the relationships between CAM precipitation and tropical SSTs in both winter and summer, through analyses of observations and model outputs from an atmospheric model and coupled climate models. In line with these objectives, the research will also aim to demonstrate that, in addition to the tropical Pacific ENSO SST, tropical Atlantic SSTs, particularly the warming trend associated with global warming, exerts a significant influence on CAM precipitation. A better understanding of the relationships between CAM precipitation and tropical Pacific/Atlantic SSTs will contribute to improving seasonal climate predictions. Furthermore, the results of this research are expected to provide valuable insights into CAM precipitation change under a warmer climate, future climate projections for the region, and practical information for local governments and policymakers in making climate adaptation decisions, addressing migration, ensuring sustainable food and nutrition security, and developing rainwater harvesting and storage systems.

1.4 Structure of the Dissertation

This thesis is structured as follows:

Chapter 2 outlines the data sources and methods used in this study, including descriptions of the observational datasets, climate models, and statistical techniques employed.

Chapter 3 describes the climatology and variability of winter and summer precipitation in CAM, as well as the variability of tropical SSTs based on observational data.

Chapter 4 presents the results of the data analysis for winter, focusing on the historical covariability between tropical SSTs and precipitation in the CAM region, associated atmospheric circulation patterns, and their relationships captured in atmospheric model simulations.

Chapter 5 replicates the analysis from Chapter 4, but for summer season.

Chapter 6 explores the characteristics and climate variability of the mid-summer drought in Central America.

Chapter 7 compares regional hydrological cycles in the present-day climate and future warmer climate, using historical climate simulations and future projections.

Chapter 8 concludes the dissertation by summarizing the key findings, discussing their significance, and offering recommendations for future research.

Chapter 2: Data and Methodology

2.1 Data

The data used in this dissertation include observational data, reanalysis data, and climate model outputs. The primary variables analyzed are seasonal mean precipitation, SST, atmospheric wind, geopotential height, surface air temperature (2-m temperature), evaporation, soil moisture, and runoff. The analysis focuses on both winter and summer seasons. Seasonal means are calculated by averaging the monthly values from December, January, and February (DJF) for winter and from June, July, and August (JJA) for summer. Note that DJF 2024 refers to December 2023 and January and February 2024.

2.1.1 Observational Data and Reanalysis Data

For the observational data used to study the covariability between CAM precipitation and tropical SSTs, CAM precipitation is sourced from the National Oceanic and Atmospheric Administration (NOAA) Precipitation Reconstruction over Land (PREC/L) dataset (Chen et al. 2002). This dataset provides monthly rainfall data at three horizontal resolutions: $0.5^{o} \times 0.5^{o}$, $1^{o} \times 1^{o}$, and $2.5^{o} \times 2.5^{o}$ (latitude × longitude). This allows us to assess how the resolution of precipitation data might influence the characteristics of precipitation statistics. The tropical SST data are taken from the NOAA Extended Reconstructed SST version 5 (ERSSTv5) on a $2^{o} \times 2^{o}$ grid (Huang et al. 2017). The atmospheric wind and geopotential height data are from the National Centers for Environmental Prediction–National Center for Atmospheric Research (NCEP–NCAR) Reanalysis (R1) products (Kalnay et al. 1996), available at a $2.5^{o} \times 2.5^{o}$ resolution. These datasets cover a common 77-year period from 1948 to 2024, during which all of them are available. The Climate Forecast System Reanalysis (CFSR; Saha et al. 2010) is a next-generation reanalysis product with a higher resolution (T382, ~38km), but is available only from 1979 onward. Additionally, there is a discontinuity in the CFSR data in the year 1999, which results in a shift in the characteristics of the tropical Pacific SST (Xue et al. 2013). Therefore, the R1 product is used in this study. Anomaly values are defined as the deviation of seasonal mean data (DJF, JJA) from the corresponding 77-year long-term climatology.

In addition to examining the atmospheric wind and height fields directly obtained from R1, the 200-hPa stream function and velocity potential are also used to gain insight into teleconnections, atmospheric wave propagation, and upper-level divergence or convergence. The stream function represents the rotational component of the atmospheric flow and is useful for analyzing large-scale, wave-like patterns, while the velocity potential is related to the divergence of the wind field and describes the non-rotational component of the wind. It reflects the divergence or convergence at upper levels of the atmosphere. Both variables are derived by solving the inverse Laplace equations for vorticity and divergence, based on the 200-hPa zonal and meridional winds.

For the study of the mid-summer drought (MSD) over CAM, daily precipitation data are used to examine the temporal evolution of the MSD, which has a timescale shorter than a month. These data are sourced from the NOAA Climate Prediction Center (CPC) Global Unified Gauge-based Analysis of Daily Precipitation dataset (Chen et al. 2008), available on a $0.5^o \times 0.5^o$ (latitude $\times$ longitude) grid. This dataset spans a 42-year period from January 1, 1982, to December 31, 2023.

Longer records of observations are also used for comparisons with the 20th century historical climate simulations. For this purpose, both land precipitation and surface air temperature are obtained from the Climate Research Unit (CRU) dataset for 1901–2009, with a $0.5^o \times 0.5^o$ grid (Jones et al. 2012). Surface air temperatures are also sourced from the Met Office Hadley Centre and CRU (HadCRUT4) dataset for 1850–2012, available on a $5^o \times 5^o$ grid (Morice et al. 2012).

Total soil moisture and land evapotranspiration data are from the National Centre for Meteorological Research (CNRM) datasets (Alkama et al. 2010; Douville et al. 2012).

2.1.2 AMIP Model Data

In addition to the observational analyses, data from global climate model simulations of the Atmospheric Model Intercomparison Project (AMIP) type are used to reproduce the observed relationships between CAM precipitation and tropical SST. In the AMIP simulations, SST is prescribed as a boundary forcing for the model atmosphere, so the precipitation–SST linkage found in the simulations mainly results from the atmospheric response to SST. Therefore, any similarity between the observations and model results can help elucidate the causality of the observed relationship between CAM precipitation and tropical SSTs.

The AMIP model used in this study is the NCEP Global Forecast System (GFS), an atmospheric component of the NCEP Climate Forecast System (CFS) version 2 (Saha et al. 2014), with a horizontal resolution of T126 (~105 km) and 64 vertical layers. The model was driven by observed, time-varying global SSTs from the Hadley Centre Sea Ice and SST (HadISST) dataset (Rayner et al. 2003) for the period 1957–2008, and from the NOAA Optimum Interpolation SST (OISST) v2 dataset (Reynolds et al. 2002) for 2009–2018. The observed monthly mean SSTs were linearly interpolated to daily values and prescribed in the model.

In addition to the SST forcing, the model was also driven by observed, time-varying sea ice and greenhouse gas concentrations. The latter increase over time and contribute to global warming. The analysis includes 18 ensemble runs, each initialized with different initial conditions on 1 January 1957, and integrated through 2018. The AMIP runs are maintained by Dr. Bhaskar Jha, my colleague at CPC. The analysis focuses on 62 years (1957–2018) of winter and summer precipitation in relation to SST forcing, derived from the GFS 18-member ensemble averages.

2.1.3 CMIP Model Data

To assess and project regional climate change, including precipitation and the associated hydrological cycle in the CAM region, simulations from the Coupled Model Intercomparison Project Phase 5 (CMIP5; Taylor et al. 2012) and Phase 6 (CMIP6; Eyring et al. 2016) are analyzed. These simulations include both present-day climate (historical experiments from 1860–2005 for CMIP5 and from 1850–2014 for CMIP6, reflecting changing conditions consistent with observations) and future climate projections (RCP4.5 experiments in CMIP5 from 2005–2100 and SSP2-4.5 in CMIP6 from 2015–2100, both with radiative forcing stabilized at 4.5W m^{-2} after 2100). The RCP4.5 scenario in CMIP5 and SSP2-4.5 in CMIP6 are chosen due to their intermediate greenhouse gas concentrations compared to other scenarios (Taylor et al. 2012, Eyring et al. 2016).

The multi-model ensemble (MME) used in this thesis includes 17 CMIP5 regular climate models and eight CMIP5 Earth system models (ESMs), as well as six CMIP6 models. The eight ESMs share the same experimental configurations as the 17 regular models. The model data were downloaded from the CMIP5 data portal (http://pcmdi9.llnl.gov) and CMIP6 data portal (https://pcmdi.llnl.gov/CMIP6/), and processed into seasonal means for DJF and JJA on a common grid ($2^o \times 2^o$). The CMIP5 data have been used in studies of climate change in the Mediterranean region (Alessandri et al. 2014; Mariotti et al. 2015) and in my M.S. thesis work (Pan 2013) at the University of Maryland. Similar analyses are being conducted for the CAM region using the CMIP5 data in this dissertation and are compared with the results from the CMIP6 data. Further details of the 25 CMIP5 models and six CMIP6 models, including their names, model resolution, number of ensemble members, and periods of integrations, are summarized in Tables 2.1 and 2,2, respectively.

2.2 Methodology

Several statistical techniques are employed in the analysis of both observational data and global climate model outputs. These include basic methods, such as correlation, linear regression, and composite analysis, as well as more advanced methods, such as singular value decomposition (SVD; Bretherton et al. 1992), empirical orthogonal function (EOF; Lorenz 1956) analysis, and Monte Carlo simulations (e.g., Wilks 1995).

2.2.1 Correlation, Linear Regression, and Composite Analysis

At least three approaches are commonly used to measure the statistical associations between two climate variables (Wilks 1995). The first is correlation analysis, where a temporal correlation coefficient is calculated between two time series. This simple technique can reveal a linear relationship between the two variables. However, since normalized correlation coefficients provide no information about the actual amplitudes of anomalies, linear regression and composite analysis are used to determine the amplitudes of anomalies associated with specific climate variability. While regression results reflect a linear relationship, composites of events representing opposite phases or different intensities may reveal nonlinear features.

2.2.2 SVD Analysis

The relationships between CAM precipitation and tropical SSTs are examined using the SVD technique (Bretherton et al. 1992). This method objectively identifies pairs of modes (spatial patterns) of precipitation and SST that exhibit maximum temporal covariance with each other (e.g., Pan et al. 2018). Each SVD mode provides a pair of time series for precipitation and SST, which can serve as two base time series to link the SVD modes to other atmospheric fields through statistical analyses, such as correlation, linear regression, and composite analysis.

While SVD analysis of observational data identifies empirical linkages between precipitation and SST, it does not imply causality. To determine whether the precipitation–SST linkages obtained in the observational data reflect atmospheric responses to SST, the results are further verified using AMIP simulations in which observed SSTs are prescribed as forcing. Thus, the same SVD analysis is also performed using data from the AMIP 18-member ensemble means.

2.2.3 EOF Analysis

EOF analysis is used to objectively identify the dominant modes of precipitation (e.g., Lorenz 1956; Wilks 1995), simplifying the complexity of the MSD by representing it with two leading EOF modes, which facilitates easier analysis and interpretation. Unlike traditional EOF analysis applied to anomaly fields, we apply this method to CAM rainfall after subtracting the annual mean climatology. This approach retains the seasonal precipitation cycle, as reflected by the two leading EOF modes, both of which capture the characteristics of the MSD.

To examine both the spatial and temporal variations of the precipitation seasonal cycle, as well as the MSD over CAM, the EOF approach is applied to CAM precipitation within the domain from 6^{o}N to 18^{o}N and from 85^{o}W to 105^{o}W. The analysis is based on rainfall variance metrics. Before performing the EOF analysis, daily precipitation data are smoothed using a 7-day moving average to eliminate high-frequency fluctuations while preserving the temporal evolution of the MSD. The EOF analysis is conducted on the total rainfall with the climatological annual mean removed. As we will show, the two leading EOF modes effectively capture key features of the seasonal cycle, including the reduced precipitation during July and August, a hallmark of the MSD.

By analyzing the Principal Component (PC) time series of these two EOF modes over 42 years (1982–2023), we assess the long-term changes in the seasonal precipitation cycle across

CAM, as well as the MSD. Composites of the PC time series for El Niño and La Niña years may reveal the impacts of ENSO on the intensity and duration of the MSD.

2.2.4 Analysis of Time Series

To assess projected climate change over the CAM region, the time series of both observational and CMIP5/CMIP6 model data, including historical simulations and RCP4.5/SSP2-4.5 projections, are constructed by averaging the seasonal mean data over the CAM domain (land only). Anomalies are defined relative to the 1980–2005 climatology for both the CMIP5 and CMIP6 data. The seasonality of climate changes is examined by comparing the seasonal mean data between winter (DJF) and summer (JJA).

The uncertainty of the multi-model ensemble (MME) means is estimated as one standard deviation of the spreads across all individual ensemble members, which quantifies inter-member variability. A 10-year low-pass Lanczos filter (Duchon, 1979) is applied to all time series (both observational data and model simulations) to emphasize decadal and longer-term variations.

2.2.5 Statistical Significance and Monte Carlo Test

The significance of the statistical results is assessed using either a two-tailed *t*-test (Snedecor and Cochran, 1989) or the Monte Carlo test (Wilks, 1995). The Monte Carlo test is a resampling technique that generates a large number of new time series (e.g., 1000) by randomly reordering the temporal points of the original data, creating time series of the same length. The test statistics calculated from these resampled series form a reference distribution. If the positive (or negative) result from the original data falls within the top (or bottom) 5% or 1% of this distribution, it is considered significant at the 95% or 99% confidence level, respectively.

Since climate data often exhibit temporal structure or autocorrelation, the resampling process for the Monte Carlo test employs the Moving Block Bootstrap method to preserve these temporal dependencies. In this approach, blocks of consecutive time points are sampled, maintaining the autocorrelated structure of the original time series.

Table 2.1 List of CMIP5 model experiments used in this study, including model name, number of ensemble members, time period of model integrations, and model resolution. A subset of models available for soil moisture analyses are denoted by an "*" for surface soil moisture analysis and by "♦" for total soil moisture analysis. Multi-model ensemble means are computed for the period of January 1860–December 2100, which is common to all models.

Model	Ensemble runs	Historical	RCP4.5	Spatial resolution
GISS- E2-R * ♦	5	1850.01-2005.12	2006.01-2300.12	2.5 º x2 º
IPSL-CM5A-MR *	1	1850.01-2005.12	2006.01-2100.12	2.5 º x1.27 º
MIROC5 *	3	1850.01-2005.12	2006.01-2100.12	1.4 ºx1.4 º
HadGEM2-CC * ♦	1	1859.12-2005.11	2005.12-2100.12	1.875 º x1.25 º
HadGEM2-ES * ♦	4	1859.12-2005.11	2005.12-2100.12	1.875 º x1.25 º
bcc-csm1-1 *	1	1850.12-2005.12	2006.01-2300.12	2.8125 º x2.8125 º
CNRM-CM5 * ♦	1	1850.12-2005.12	2006.01-2300.12	1.40625 º x1.40625 º
inmcm4 * ♦	1	1850.01-2005.12	2006.01-2100.12	2 º x1.5 º
CCSM4 ♦	6	1850.01-2005.12	2006.01-2100.12	1.25 º x0.9375 º
CSIRO-Mk3-6-0 *	10	1850.12-2005.12	2006.01-2100.12	1.875 º x1.875 º
IPSL-CM5B-LR *	1	1850.01-2005.12	2006.01-2100.12	3.75 º x1.89 º
ACCESS1-0 * ♦	1	1850.12-2005.12	2006.01-2100.12	1.875 º x1.25 º
MRI-CGCM3 * ♦	1	1850.01-2005.12	2006.01-2100.12	1.125 º x1.125 º
HadGEM2-AO	1	1860.01-2005.12	2006.01-2099.12	1.875 º x1.25 º
FGOALS-s2 *	1	1850.01-2005.12	2006.01-2100.12	2.8125 º x1.67 º
CMCC-CM ♦	1	1850.12-2005.12	2006.01-2100.12	0.75 º x0.75 º
IPSL-CM5A-LR *	3	1850.01-2005.12	2006.01-2100.12	3.75 º x1.89 º
MPI-ESM-LR ♦	3	1850.01-2005.12	2006.01-2100.12	1.875 º x1.875 º
MIROC-ESM	1	1850.01-2005.12	2006.01-2300.12	2.8125 º x2.8125 º
MPI-ESM-MR ♦	1	1850.01-2005.12	2006.01-2100.12	1.875 º x1.875 º
NorESM1-M * ♦	1	1850.01-2005.12	2006.01-2300.12	2.5 º x1.8947 º
NorESM1-ME * ♦	1	1850.01-2005.12	2006.01-2102.12	2.5 º x1.8947 º
MIROC-ESM-	1	1850.01-2005.12	2006.01-2100.12	2.8125 º x2.8125 º
CanESM2	3	1850.01-2005.12	2006.01-2100.12	2.8125 º x2.8125 º
BNU-ESM * ♦	1	1850.01-2005.12	2006.01-2100.12	2.8125 º x2.8125 º

Table 2.2 List of CMIP6 model experiments used in this study, including model name, number of ensemble members, time period of model integrations, and model resolution. Multi-model ensemble means are computed for the period of January 1850–December 2100.

Model	Ensemble runs	Historical	SSP245	Spatial resolution
BCC-CSM2-MR	1	1850.01-2014.12	2015.01-2100.12	1.125 ^{o} x1.12 ^{o} (Gaussian grid)
CESM2	3	1850.01-2014.12	2015.01-2100.12	1.25 ^{o} x0.942408 ^{o}
CESM2-WACCM	3	1850.01-2014.12	2015.01-2100.12	1.25 ^{o}x0.942408 ^{o}
EC-Earth3-Veg	1	1850.01-2014.12	2015.01-2100.12	0.703125 ^{o} x0.69 ^{o} (Gaussian grid)
IPSL-CM6A-LR	6	1850.01-2014.12	2015.01-2100.12	2.5 ^{o} x1.2676 ^{o}
MIROC6	10	1850.01-2014.12	2015.01-2100.12	1.40625 ^{o} x1.39^o (Gaussian grid)

Chapter 3: Climatology and Variability of CAM Precipitation and Tropical SSTs

The objectives of this chapter are to systematically describe the climatology and variability of CAM precipitation and tropical SSTs, providing a foundation for further analysis of their relationships in the subsequent chapters. Sections 3.1 and 3.2 cover the climatological seasonal mean precipitation, its standard deviation, and long-term trends, as well as time series of area-averaged seasonal mean precipitation over two subregions, for winter (DJF) and summer (JJA), respectively. Section 3.3 examines the climatological seasonal cycle of CAM precipitation, including the mid-summer drought (MSD). Section 3.4 presents the variability (standard deviation) and long-term trends of tropical SSTs.

3.1 Climatology and Variability of Winter Precipitation

The observed long-term average of winter (DJF) seasonal mean precipitation over CAM is shown in Figure 3.1a, derived from 77 years of PREC/L data (1948–2024) with a resolution of $1^{o} \times 1^{o}$ (latitude × longitude). The rainfall climatology is characterized by abundant precipitation (> 2 mm day^{-1}) over Central America and relatively dry conditions (< 1 mm day^{-1}) across Mexico. Winter mean precipitation contributes about 10%–30% of the annual total over most of CAM, except in Baja California, where winter precipitation contributes 40%–60% of the annual total (Figure 3.1b). The variability of winter precipitation (Figure 3.1c), quantified by the standard deviation of DJF seasonal mean precipitation, shows strong variability in Central America and weak variability to the north. The long-term linear trend indicates decreasing precipitation at rates of -0.2 to -0.8 mm day^{-1} per decade in Central America, with rates of about -0.2 mm day^{-1} per decade along the Pacific Coast and in Northern Mexico (Figure 3.1d). In contrast, trends of increasing precipitation at rates of 0.2 mm day^{-1} per decade are observed in the Yucatan Peninsula, Central Mexico, and northwestern regions.

To examine how data resolution may affect precipitation statistics, we perform the same analysis as in Figure 3.1, but using PREC/L data with resolutions of $0.5^o \times 0.5^o$ and $2.5^o \times 2.5^o$, as shown in Figures 3.2 and 3.3. Compared to the results in Figure 3.1 based on the 1^o resolution data, the higher-resolution data (0.5^o, Figure 3.2) captures finer spatial variations, allowing for a more detailed representation of precipitation patterns at smaller scales (e.g., DJF mean precipitation over Central America in Figures 3.1a and 3.2a). In contrast, the lower-resolution data (2.5^o, Figure 3.3) averages out these finer features, leading to a less accurate representation of regional precipitation extremes or gradients, particularly in areas with complex terrain (Figure 3.3a). Additionally, localized areas of higher or lower precipitation can be smoothed out in lower-resolution data, resulting in lower variability, as reflected in the smaller standard deviation in Central America shown in Figure 3.3c. Although the results with all three data resolutions display similar overall large-scale distributions of precipitation statistics (Figures 3.1, 3.2, 3.3), the results with the 1^o data are more comparable to those with the 0.5^o data than the 2.5^o data, particularly in terms of local maximum values and finer spatial structures.

The variability of winter precipitation is further explored by examining the time series of area-average DJF seasonal mean precipitation anomalies. Given the distinct precipitation patterns and characteristics between Central America and Mexico, as shown in Figure 3.1, two time series are constructed by averaging precipitation anomalies in two subregions: south of 17^oN for Central America and north of 17^oN for Mexico. Figure 3.4 shows these two time series from 1948 to 2024, along with their linear trends, using PREC/L data at three different resolutions: $1^{o} \times 1^{o}$, $0.5^{o} \times 0.5^{o}$, and $2.5^{o} \times 2.5^{o}$ (latitude × longitude).

The time series of area-averaged winter precipitation in Central America shows larger interannual variability than in Mexico (Figure 3.4a), with corresponding standard deviations of 0.54 and 0.26 mm day^{-1} (Table 3.1), respectively, using the $1^{o} \times 1^{o}$ data. The correlation between the two time series is 0.01 (Table 3.1), indicating that the winter precipitation variations over Central America and Mexico are largely independent. Additionally, a trend of decreasing precipitation (-0.13 mm day^{-1} per decade) is found over Central America, while virtually no trend (-0.005 mm day^{-1} per decade) is found for Mexico, likely due to the cancellation of opposing positive and negative trends over southern and northern Mexico (Figure 3.1d). Precipitation anomalies averaged over Central America have been largely negative since 2000 (Figure 3.4a), consistent with the prolonged drought in the region in recent decades.

The results from the time series using the $0.5^{o} \times 0.5^{o}$ and $2.5^{o} \times 2.5^{o}$ data (Figures 3.4b and 3.4c, Table 3.1) are quantitatively similar to those with the $1^{o} \times 1^{o}$ data (Figure 3.1a, Table 3.1). In particular, the correlations among the time series derived from different resolution data are highly significant, with correlation coefficients exceeding 0.93 for Central America and 0.99 for Mexico, all surpassing the 99% significance level. Therefore, the statistics of area-averaged precipitation are not sensitive to the resolution of the data used.

3.2 Climatology and Variability of Summer Precipitation

The observed 77-year (1948–2024) mean summer (JJA) precipitation over CAM generally decreases from south to north (Figure 3.5a), based on the $1^{o} \times 1^{o}$ PREC/L data. Maximum precipitation exceeds 10 mm day^{-1} over Central America and southern Mexico. Compared to Figure 3.1a, climatological summer seasonal precipitation is about twice as much as winter precipitation across CAM. Although mean summer precipitation is lower in Mexico north of 20^{o}N (Figure 3.5a), it contributes significantly (greater than 50%) to the annual total over the western half of the country (Figure 3.5b), highlighting the importance of the summertime North American monsoon precipitation in this region. Similar to the seasonal mean precipitation (Figure 3.5a), the interannual variability of summer precipitation is strong in Central America and southern Mexico, but weak in northern Mexico, as measured by the standard deviation of JJA seasonal mean precipitation (Figure 3.5c). Long-term trends show a decrease in summer precipitation across most of CAM, with rates ranging from -0.2 to -1.0 mm day^{-1} per decade (Figure 3.5d), except in some regions of central Mexico and along the U.S.–Mexico border, where upward trends are observed at 0.2 mm day^{-1} per decade.

We also compare summer precipitation statistics using PREC/L data at different resolutions: 1^o × 1^o (Figure 3.5), 0.5^o × 0.5^o (Figure 3.6), and 2.5^o × 2.5^o (Figure 3.7). In general, high-resolution data (Figures 3.5 and 3.6) tend to provide more accurate, detailed, and localized precipitation statistics, revealing small-scale patterns and trends that may be lost in low-resolution data (Figure 3.7). While low-resolution data is useful for capturing large-scale patterns, it may miss or smooth out significant regional features and variability (Figure 3.7). In Chapters 4 and 5, the PREC/L data with the 1^o × 1^o resolution is used in the analysis, as it aligns with the 0.5^o × 0.5^o data in describing rainfall statistics.

The time series of area-averaged summer precipitation (1^o × 1^o resolution) in Central America (red line, Figure 3.8a) shows larger interannual anomaly amplitudes than in Mexico (blue line), with standard deviations of 1.00 and 0.55 mm day^{-1} (Table 3.1), respectively. The correlation between the two time series is 0.52 (Table 3.1), suggesting that the variations in summer precipitation over Central America and Mexico are somewhat related. For example, the two time series exhibit similar variations during the 2000s. Notably, precipitation anomalies in both regions were largely negative during this period (Figure 3.8a), consistent with the prolonged drought in CAM. Central America also shows a long-term trend of decreasing precipitation at a rate of -0.19 mm day^{-1} per decade. In contrast, no significant trend is found in Mexico (-0.03 mm day^{-1} per decade). Thus, summer precipitation in the two regions displays distinct long-term trends.

Similar to the results for winter season, both the standard deviation and linear trend, as well as the correlation between the two time series of summer precipitation derived from either higher-resolution (0.5° × 0.5°) data or lower-resolution (2.5° × 2.5°) data (Figures 3.8b and 3.8c, Table 3.1), agree well with those using the (1° × 1°) data (Figure 3.8a, Table 3.1). The correlations among the time series from the data at the three resolutions are over 0.97 for Central America and 0.98 for Mexico, all well above the 99% significance level. Again, the results of the summer precipitation suggest that the statistics of area-averaged precipitation are not sensitive to the resolution of the data used.

3.3 Climatological Seasonal Cycle of CAM Precipitation and Mid-summer Drought

Figure 3.9a presents the long-term mean (1948–2024) monthly precipitation from January to December, averaged over CAM (green), Central America (red), and Mexico (blue), using PREC/L data at different resolutions: 1° × 1° (solid), 0.5° × 0.5° (dotted), and 2.5° × 2.5° (dashed). The seasonal cycle of precipitation in southern CAM (Central America, red) shows a dry season (less than 4 mm day^{-1}) from December to April, and a wet season (above 8 mm day^{-1}) from June to October. The wet season has two peaks in June and September, with precipitation around 9 mm day^{-1}. Between these two peaks, there is a mid-summer dry period, characterized by relatively dry conditions and minimum precipitation around 8 mm day^{-1}, a feature of the mid-summer drought

(MSD). The seasonal evolutions of area-averaged precipitation at the three resolutions show a consistent pattern and similar magnitudes.

In northern CAM (Mexico, blue lines in Figure 3.9a), the seasonal cycle also includes a dry season (< 1 mm day^{-1} from November to May) and a wet season (3–4 mm day-1 from June to September), with considerably less precipitation. However, no MSD is observed over Mexico in the climatological monthly precipitation evolution. The seasonal cycle of precipitation averaged over the entire CAM is similar to that over Mexico, with a slight increase of 0.5–1 mm day^{-1} throughout the year (green, Figure 3.9a). Again, no MSD is evident in the seasonal cycle of the CAM precipitation using monthly rainfall data.

To capture the evolution of the MSD at a subseasonal timescale, monthly mean precipitation may not provide sufficient resolution. Therefore, we use daily rainfall data, the NOAA CPC Global Unified Gauge-based Analysis of Daily Precipitation dataset (Chen et al. 2008), to illustrate the seasonal precipitation cycle with higher temporal resolution. Figure 3.9b presents the long-term mean (1982–2024) time series of the 7-day running mean climatological daily precipitation, averaged for regions south of 17°N (Central America, red), north of 17°N (Mexico, blue), and over the CAM (green), from January 1 to December 31. The 7-day running mean helps smooth out day-to-day fluctuations, providing a clearer representation of the seasonal cycle.

The seasonal cycle of precipitation derived from daily data (Figure 3.9b) reveals much finer details compared to that derived from monthly data (Figure 3.9a). In Central America (Figure 3.9b, red line), the seasonal cycle shows a dry season (less than 2 mm day^{-1}) from mid-December to mid-April and a wet season (above 4 mm day^{-1}) from mid-May to mid-November. The wet season has two peaks, one in June and another at the end of September, with precipitation reaching or exceeding 7 mm day^{-1}. Between these peaks, there is a minimum precipitation period (MSD) around the end of July, where precipitation drops below 5 mm day^{-1}.

In contrast, north of 17°N, the area-average precipitation (Figure 3.9b, blue line) also shows wet and dry seasons, but the contrast is less pronounced. The two summer precipitation peaks reach about 4–5 mm day^{-1}, significantly lower than those observed south of 17°N. The relatively wet period, with precipitation above 3 mm day^{-1}, lasts from mid-June to mid-October, approximately one-third of the year, which is shorter than the wet period in Central America (mid-May to mid-November). Between the two peaks, a minimum precipitation of 3.5 mm day^{-1} is noticeable, indicating a weaker MSD in Mexico that is not detectable in the monthly data (Figure 3.9a).

The seasonal cycle of precipitation averaged over the CAM (Figure 3.9b, green line) is more similar to that in Mexico than to Central America. This is due to the larger size of Mexico, which carries more weight in the area-averaged precipitation compared to Central America. Overall, the higher temporal resolution of the daily data provides a more accurate representation of the timing of wet and dry seasons, as well as the MSD.

3.4 Variability and Long-term Trends of Tropical SSTs

To illustrate the spatial distribution of SST variability, Figure 3.10a shows the standard deviation of winter (DJF) seasonal mean SST anomalies, calculated from 77 years of the ERSSTv5 data (1948–2024). In winter, large SST variability is found in the eastern and central equatorial Pacific. These SST fluctuations are primarily brought about by El Niño and La Niña events, which dominate tropical SST variations on interannual timescales. The maximum SST standard deviations (~ 1.2 K) are located along the equator between 120^{o}W and 160^{o}W. The region coincides with the area of largest SST anomalies during the mature phase of an ENSO event (e.g., Rasmusson and Carpenter 1982). Relatively large standard deviations of winter SST (> 0.6 K) are also observed in the North Pacific and North Atlantic.

Figure 3.10b shows the linear trend of winter SST over the 77-year period. Warming trends greater than 0.1 K per decade are observed primarily in the Indian and Atlantic Oceans, as well as in the western Pacific. In contrast, the linear trends in the central tropical Pacific are relatively weak (0.06–0.08 K per decade), where winter SSTs exhibit large interannual variability (Figure 3.10a). The distinction between regions with high variability and those with strong warming trends is useful for studying their separate impacts on CAM precipitation. Since the standard deviations shown in Figure 3.10a are derived from total SST anomalies, they include the contribution from warming trends. To isolate the interannual variability, we calculated the standard deviations using detrended SST anomalies, as shown in Figure 3.10c. Although there is a slight deduction in values where the warming trends are relatively strong, the spatial distribution of standard deviation remains largely unchanged between Figures 3.10a and 3.10c.

The distribution of the standard deviation of JJA SST reveals the largest SST variability along the coast of South America near 5°S (Figure 3.11a). The maximum values (~1.2 K) in summer are comparable to those in winter (Figure 3.10a), though they are more confined to the coastline. In the middle latitudes around 40°N, a broad band of high SST variability is also present. The amplitude of extratropical SST standard deviation is larger in summer than in winter. Similar to the winter season, summer SST warming trends greater than 0.1 K per decade are observed in the Indian and Atlantic Oceans, as well as the western Pacific (Figure 3.11b), with warming trends being stronger in JJA. Similar to the winter season, there is no significant change in the SST standard deviation after detrending the SST anomalies for the summer season (Figures 3.11a vs. 3.11c).

3.5 Summary

This chapter provides an analysis of mean seasonal precipitation patterns and variability over CAM and tropical SSTs. Winter precipitation is characterized by abundant rainfall in Central America and drier conditions in northern Mexico, with a significant decreasing trend observed in Central America since 2000. In summer, precipitation is generally higher across CAM, with a notable decline in Central America and no significant trend in Mexico. The seasonal cycle is characterized by a mid-summer drought (MSD) in Central America, which is more clearly captured using daily data compared to monthly data.

Tropical SST variability is largely influenced by ENSO events, with significant fluctuations observed in the equatorial Pacific. Warming trends are evident in the Indian and Atlantic Oceans in both the winter and summer seasons. The analysis of precipitation and SST trends highlights key patterns and changes that will serve as a foundation for exploring their relationships and regional climate impacts in subsequent chapters.

Table 3.1 List of standard deviations (mm day^{-1}) and linear trends (mm day^{-1} per decade) of the time series (1948–2024) of seasonal mean precipitation area-averaged over Central America and Mexico for winter (DJF) and summer (JJA), using PREC/L data at three resolutions: 1° × 1°, 0.5° × 0.5°, and 2.5° × 2.5° (latitude × longitude), respectively. The table also includes the correlation between these two time series, as well as the correlation between the time series derived from three different resolution data.

Season and Subregion	Resolution	Standard Deviation	Linear Trend	Correlation between 2 Subregions	Correlation among 3 Resolution Data
DJF Central America	1° × 1°	0.54	-0.13	0.01	0.93 (1° vs. 0.5°)
	0.5° × 0.5°	0.44	-0.07	-0.04	0.98 (0.5° vs. 2.5°)
	2.5° × 2.5°	0.40	-0.07	0.03	0.95 (2.5° vs. 1°)
DJF Mexico	1° × 1°	0.26	-0.005		0.997 (1° vs. 0.5°)
	0.5° × 0.5°	0.26	-0.006		0.995 (0.5° vs. 2.5°)
	2.5° × 2.5°	0.30	-0.006		0.998 (2.5° vs. 1°)
JJA Central America	1° × 1°	1.00	-0.19	0.52	0.98 (1° vs. 0.5°)
	0.5° × 0.5°	1.06	-0.21	0.57	0.99 (0.5° vs. 2.5°)
	2.5° × 2.5°	1.03	-0.20	0.60	0.97 (2.5° vs. 1°)
JJA Mexico	1° × 1°	0.55	-0.03		0.98 (1° vs. 0.5°)
	0.5° × 0.5°	0.60	-0.07		0.99 (0.5° vs. 2.5°)
	2.5° × 2.5°	0.58	-0.07		0.98 (2.5° vs. 1°)

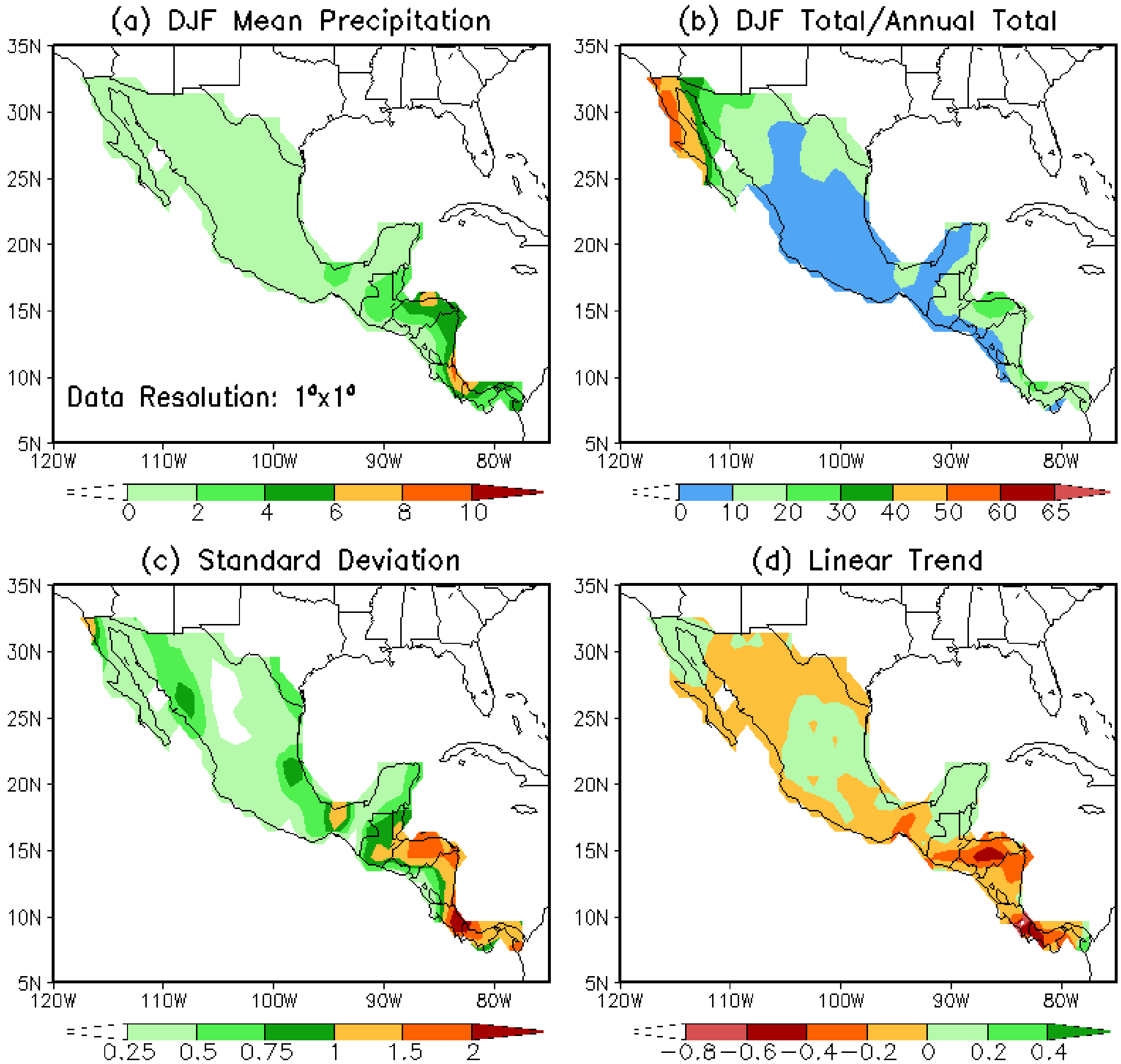

Figure 3.1 (a) Climatological winter (DJF) seasonal mean precipitation (mm day^{-1}) in Central America and Mexico, (b) the ratio (%) of climatological DJF total to climatological annual total precipitation, (c) standard deviation of DJF precipitation (mm day^{-1}), and (d) long-term linear trend of DJF precipitation (mm day-1 per decade), based on 1948–2024 PREC/L data with a resolution of 1^{o} x 1^{o} (latitude × longitude).

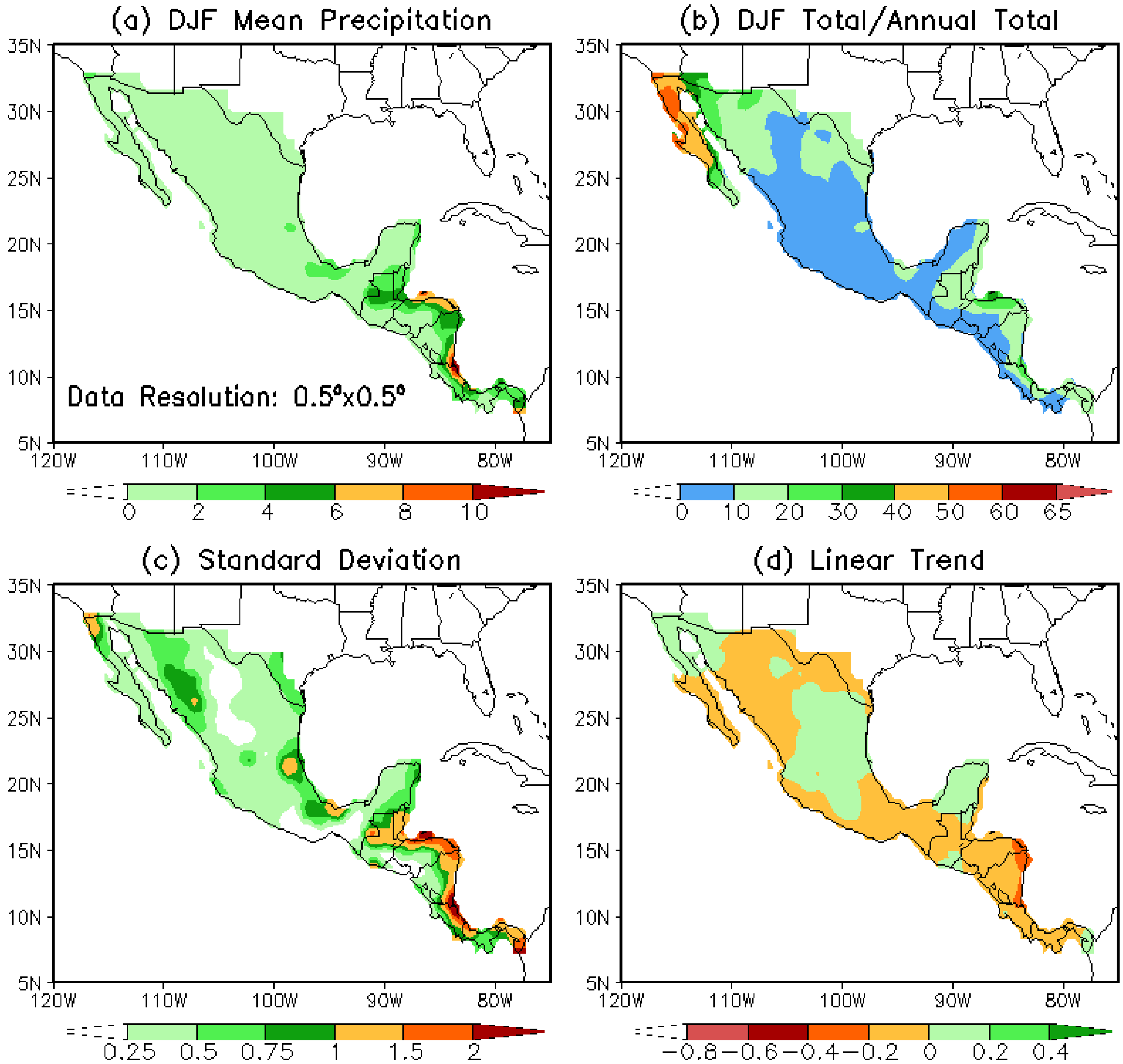

Figure 3.2 Same as Figure 3.1, but using precipitation data with a resolution of 0.5º x 0.5º (latitude × longitude).

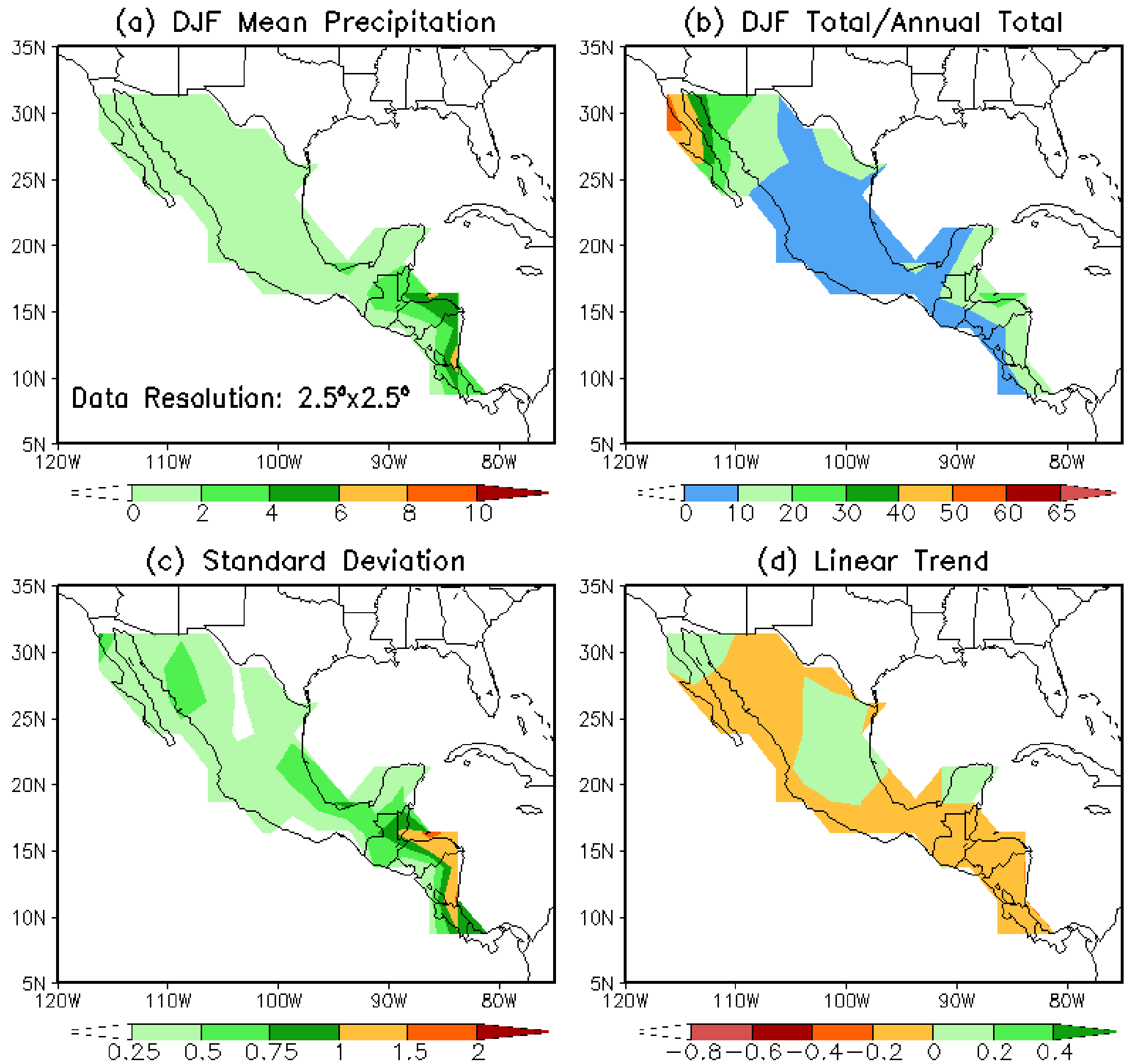

Figure 3.3 Same as Figure 3.1, but using precipitation data with a resolution of 2.5º x 2.5º (latitude × longitude).

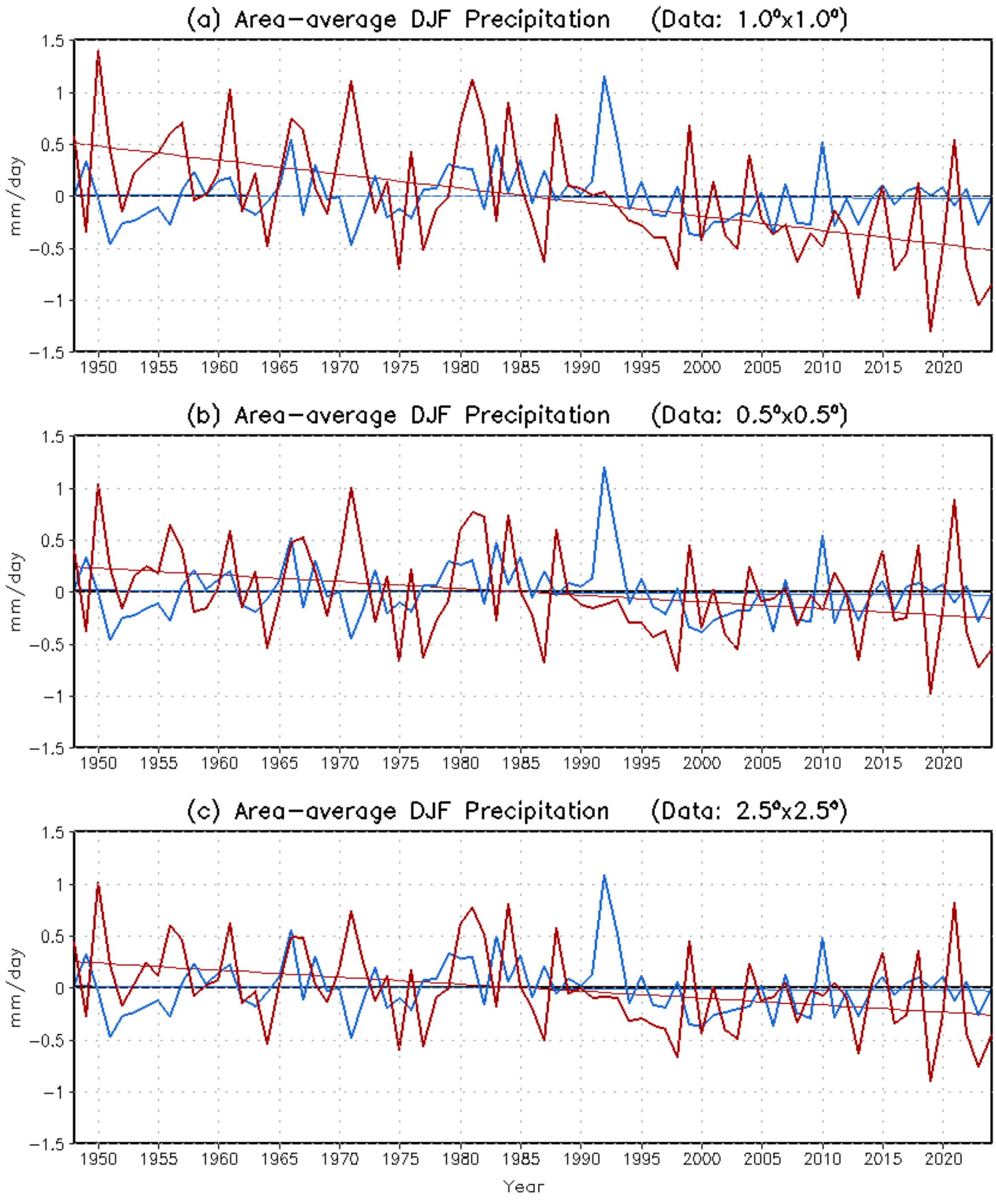

Figure 3.4 Time series (1948–2024) of DJF seasonal mean precipitation anomalies (mm day^{-1}) averaged over Central America (south of 17°N, thick red line) and Mexico (north of 17°N, thick blue line), derived from PREC/L data with spatial resolutions of (a) 1° × 1°, (b) 0.5° × 0.5°, and (c) 2.5° × 2.5° (latitude × longitude). The thin red and blue lines represent the corresponding linear trends (mm day^{-1} per decade).

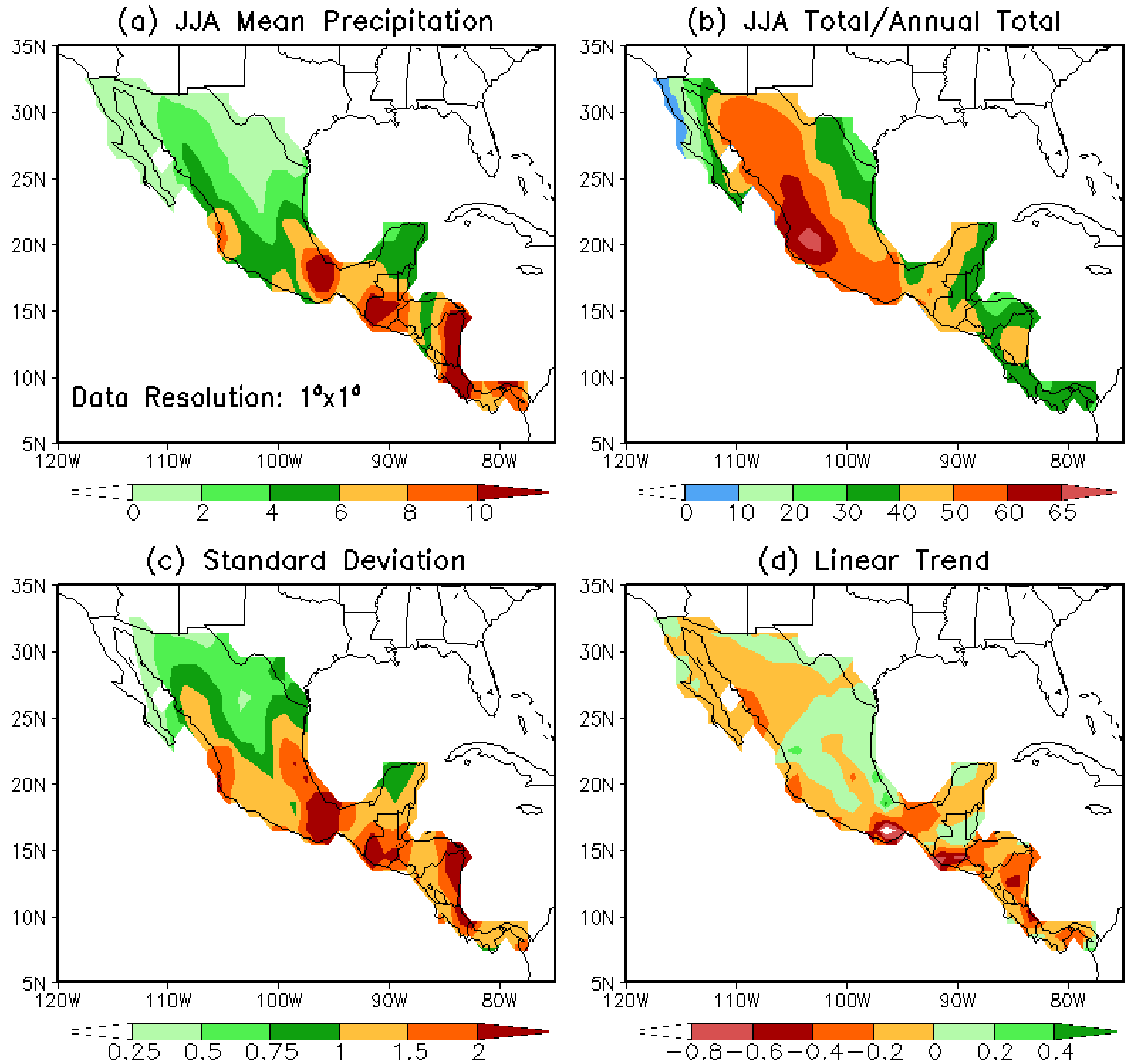

Figure 3.5 (a) Climatological summer (JJA) seasonal mean precipitation (mm day^{-1}) in Central America and Mexico, (b) the ratio (%) of climatological JJA total to climatological annual total precipitation, (c) standard deviation of JJA precipitation (mm day^{-1}), and (d) long-term linear trend of JJA precipitation (mm day-1 per decade), based on 1948–2024 PREC/L data with a resolution of 1° x 1° (latitude × longitude).

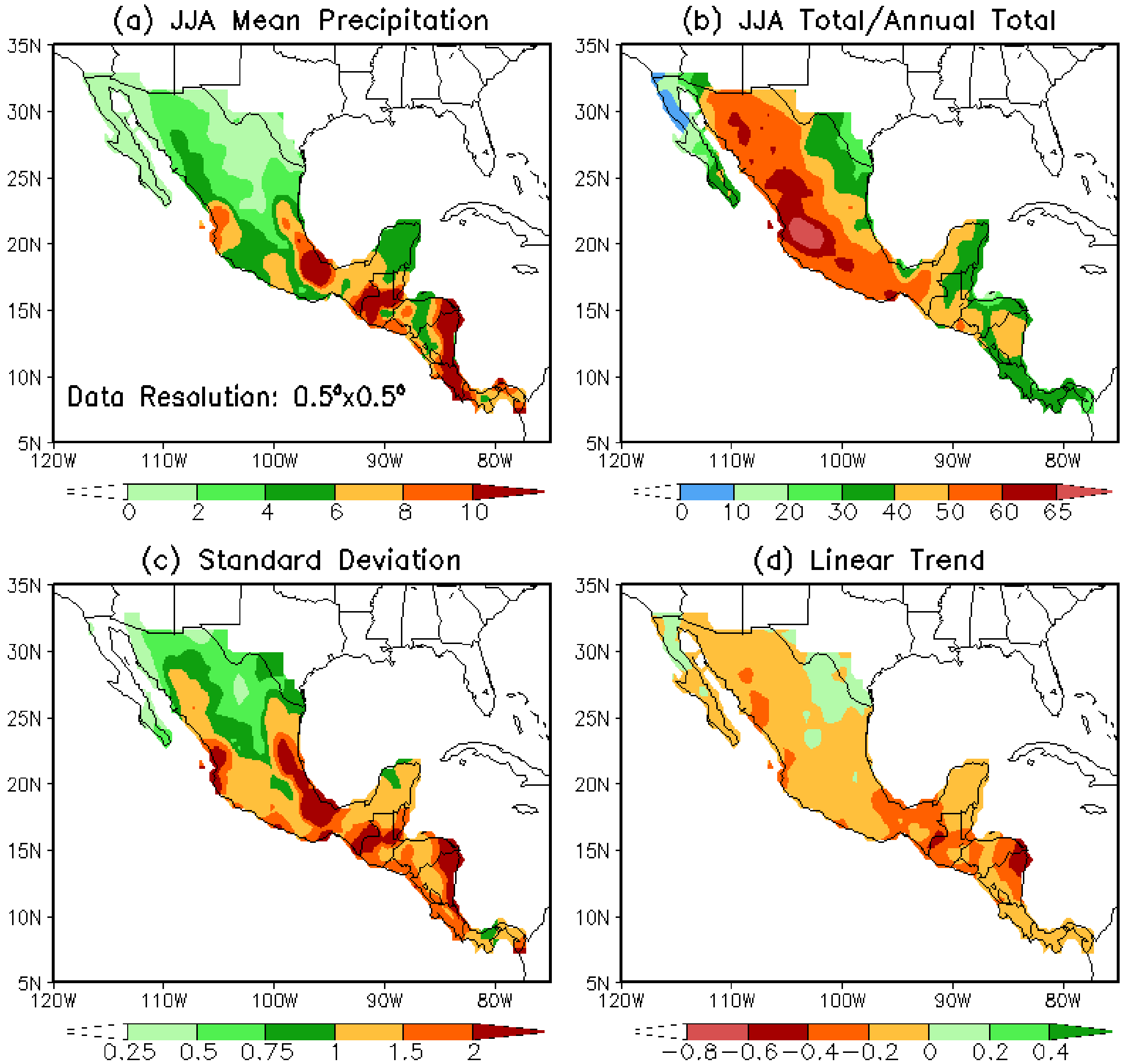

Figure 3.6 Same as Figure 3.5, but using precipitation data with a resolution of 0.5º x 0.5º (latitude × longitude).

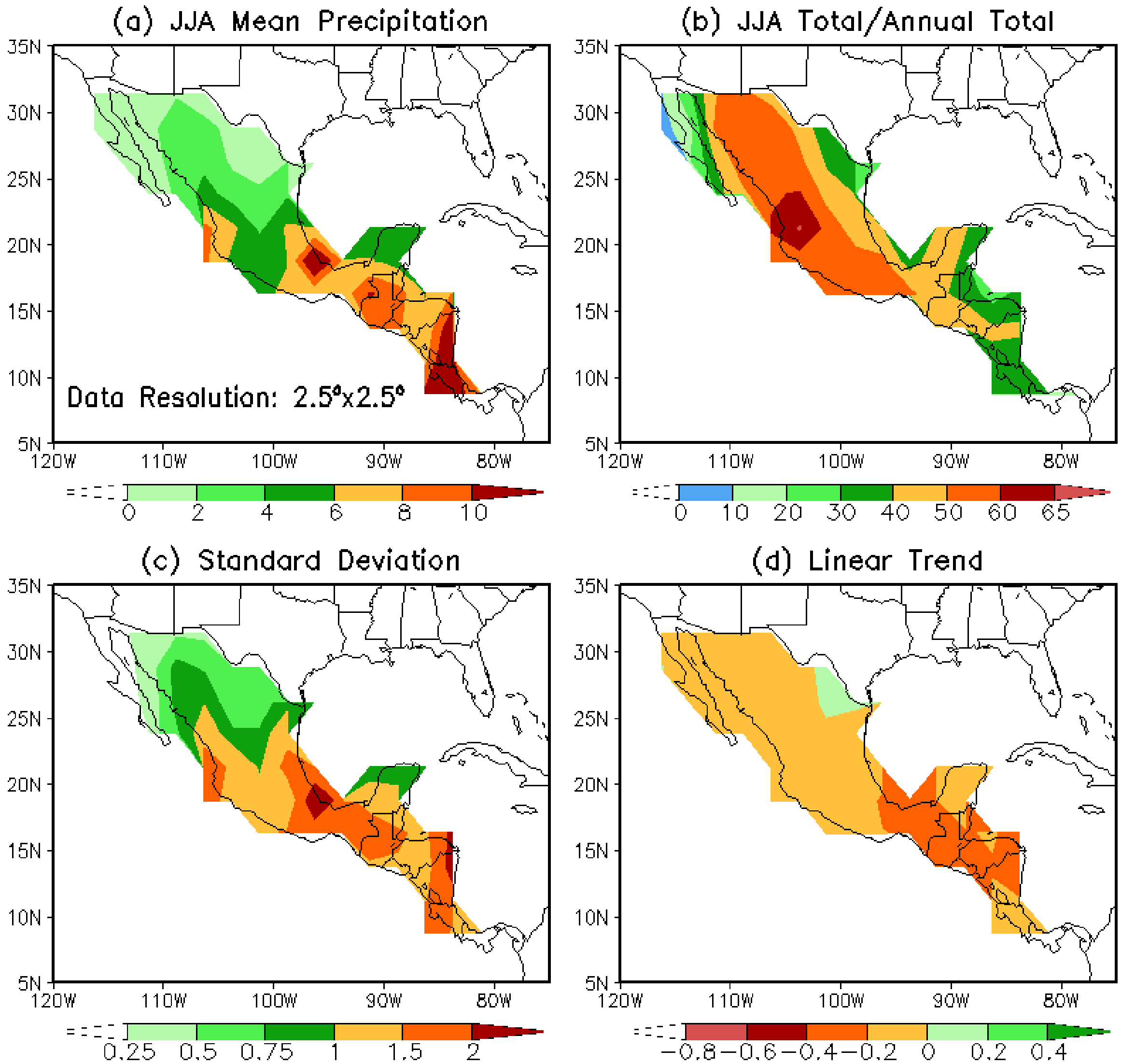

Figure 3.7 Same as Figure 3.5, but using precipitation data with a resolution of 2.5° x 2.5° (latitude × longitude).

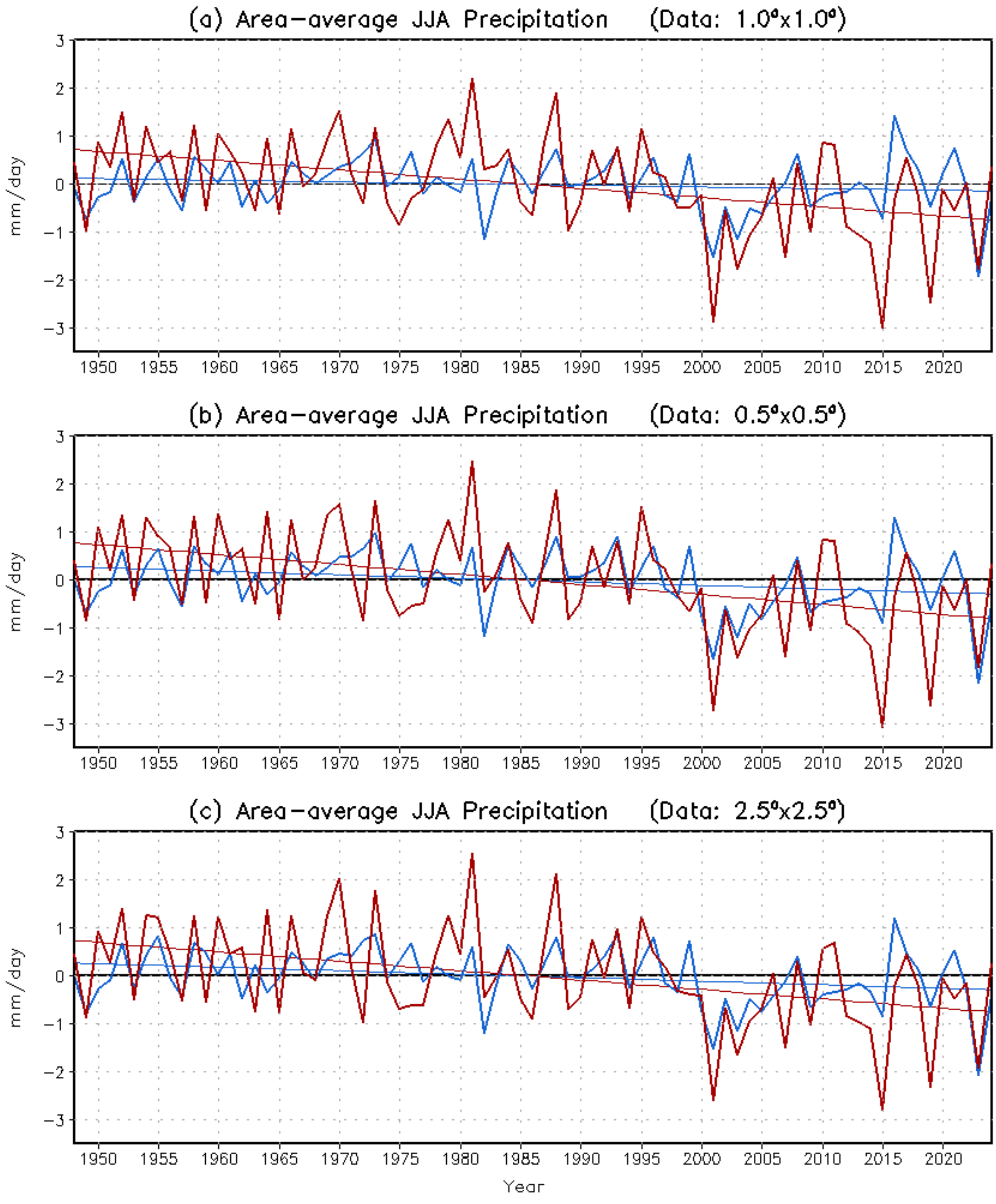

Figure 3.8 Time series (1948–2024) of JJA seasonal mean precipitation anomalies (mm day^{-1}) averaged over Central America (south of 17^{o}N, thick red line) and Mexico (north of 17^{o}N, thick blue line), derived from PREC/L data with spatial resolutions of (a) 1^{o} × 1^{o}, (b) 0.5^{o} × 0.5^{o}, and (c) 2.5^{o} × 2.5^{o} (latitude × longitude). The thin red and blue lines represent the corresponding linear trends (mm day^{-1} per decade).

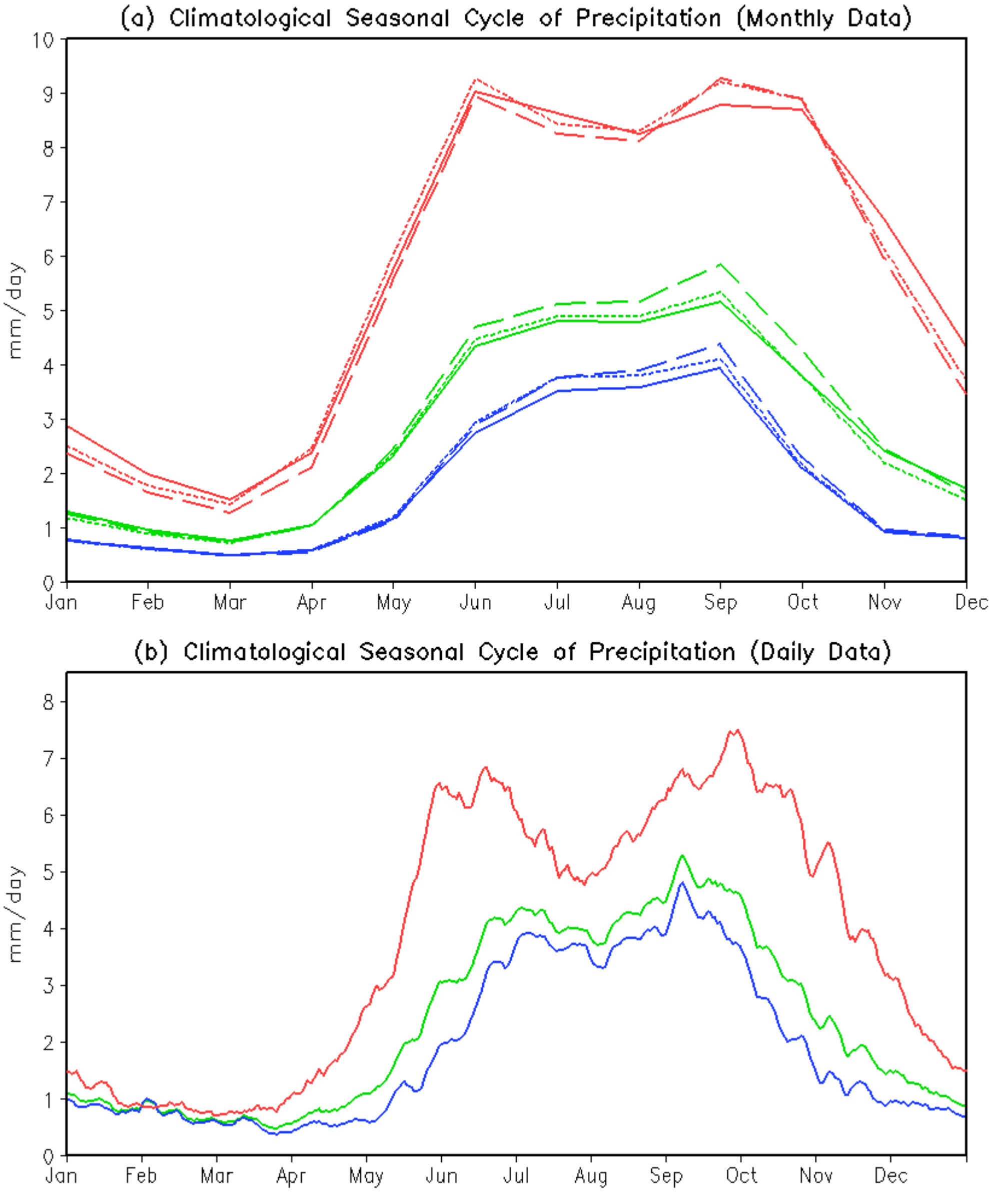

Figure 3.9 Climatological seasonal cycle of precipitation averaged over CAM (green), Central America (red), and Mexico (blue), derived from (a) 77 years of monthly PREC/L data (1948–2024) and (b) 43 years of daily precipitation (1982–2024) from NOAA CPC Global Unified Gauge-based Analysis. In panel (a), solid, dotted, and dashed lines represent monthly precipitation data at $1^{o} \times 1^{o}$, $0.5^{o} \times 0.5^{o}$, and $2.5^{o} \times 2.5^{o}$ resolution, respectively.

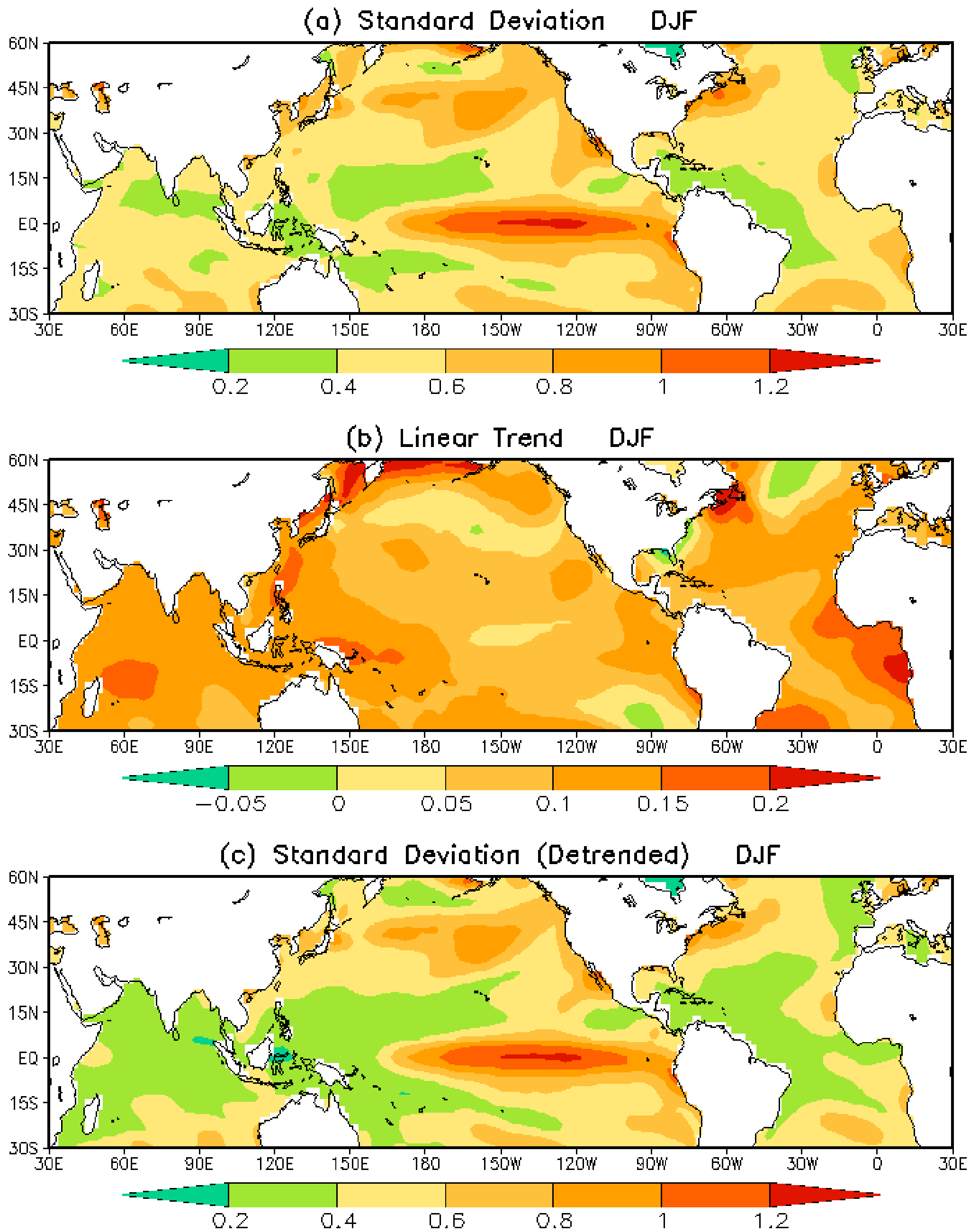

Figure 3.10 (a) Standard deviation of winter (DJF) seasonal mean SST (K), (b) linear trend of DJF SST (K per decade), and (c) standard deviation of detrended DJF SST (K), calculated from 77 years of ERSSTv5 data (1948–2024).

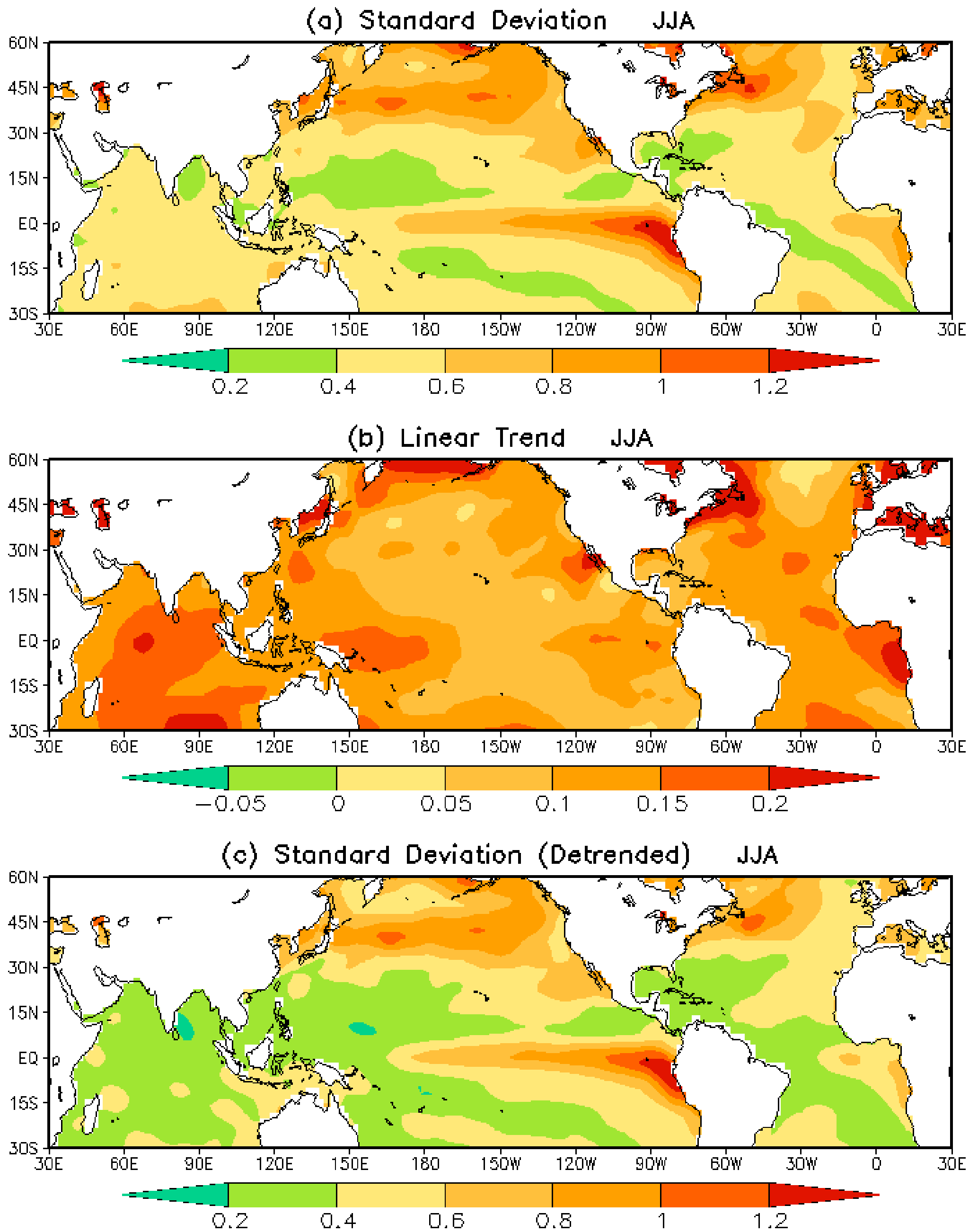

Figure 3.11 (a) Standard deviation of summer (JJA) seasonal mean SST (K), (b) linear trend of JJA SST (K per decade), and (c) standard deviation of detrended JJA SST (K), calculated from 77 years of ERSSTv5 data (1948–2024).

Chapter 4: Covariability of CAM Precipitation and Tropical SSTs in Winter

The objectives of this chapter are to explore the relationships between wintertime CAM precipitation and tropical SSTs, and to understand these linkages by examining the connections with atmospheric circulation. While similar results were presented in Pan et al. (2018), this analysis extends the dataset from 68 years (1948–2015) to 77 years (1948–2024) and focuses specifically on the DJF season, as opposed to the January–March period used previously. The first section applies SVD analysis to the 77-year seasonal mean SST (ERSSTv5) and precipitation (PREC/L) fields, allowing for the objective identification and quantification of the coupling between CAM precipitation and SSTs in the tropical Pacific and Atlantic. Section 4.2 explores the nonlinear relationship between winter CAM precipitation and ENSO SST. Section 4.3 investigates the atmospheric circulation associated with the identified SVD modes to provide insights into the dynamics underlying air-sea interactions. Section 4.4 examines AMIP model simulations to assess whether the observed relationships reflect an atmospheric response to tropical SST forcing. Section 4.5 evaluates the potential predictability of CAM winter precipitation based on tropical SST distribution. Finally, Section 4.6 concludes with a summary of the findings.

4.1 Observed Relationships between Winter CAM Precipitation and Tropical SSTs

To quantify the relationships between CAM precipitation and tropical SSTs, an SVD analysis is performed using the covariance matrices of winter (DJF) CAM precipitation and SSTs in the tropical Pacific and Atlantic basins (30^{o}S–30^{o}N, 120^{o}E–30^{o}E). Table 1 summarizes the statistics of two leading SVD modes, including the percentage of covariance explained by each mode, the temporal correlation coefficient between each pair of SVD time series, and the percentage of variance explained by each mode in the individual fields. Together the two modes explain 95% of the covariance between the SST and precipitation fields during winter, with the corresponding components accounting for 60% of the SST variance and 41% of the precipitation variance, respectively.

Figure 4.1 illustrates the spatial patterns of the two leading SVD modes as homogeneous correlation maps (Wallace et al. 1992) for both SST and precipitation. The first SVD mode of SST (Figure 4.1a) reveals a typical La Niña SST pattern, with large negative correlations in the eastern and central tropical Pacific. Negative correlations are also observed along the west coast of North America, while positive correlations appear in the central North Pacific. In association with La Niña, negative SST anomalies extend across the tropical Atlantic and Indian Oceans, consistent with documented interactions between ENSO and these regions (e.g., Wang et al. 2013; Zhu et al. 2015; Terray et al. 2016). This mode explains 41% of the total variance in tropical Pacific and Atlantic SSTs (Table 4.1). The precipitation component of the first SVD mode accounts for 23% of the total winter precipitation variance in CAM (Table 4.1). The precipitation pattern (Figure 4.1b) shows significant negative correlations in northern and central Mexico, and positive correlations in Central America. Thus, during La Niña, winters tend to be drier than normal in Mexico, but wetter than normal in Central America, which aligns with previous findings (Cavazos and Hastenrath 1990; Magaña et al. 2003; Seager et la. 2009).

The second SVD mode of SST is characterized by two broad regions of positive correlations, spanning the tropical Atlantic basin and the tropical Indian Ocean–western Pacific sector (Figure 4.1c). The precipitation pattern associated with this mode shows coherent, strong negative correlations in Central America and southern Mexico (Figure 4.1d), regions that typically receive substantial winter precipitation (Figure 3.1a). Negative correlations are also observed in northern Mexico. Thus, the second mode represents a connection between general warming in the tropical oceans and winter drought in Central America, southern Mexico, and northern Mexico. This mode explains 19% of the SST variance, considerably less than the first mode (41%, Table 4.1). However, it accounts for 18% of the precipitation variance, which is closer to the precipitation variance explained by mode 1 (23%).

The two pairs of SVD time series for SST and precipitation are shown in Figure 4.2. The temporal correlation between the SST and precipitation time series in mode 1 (Figure 4.2a) is 0.61, which is well above the 99% significance level. The SST time series (red bars) shows large positive and negative values exceeding one standard deviation during La Niña years (1950, 1951, 1955, 1956, 1968, 1971, 1974, 1975, 1976, 1989, 2000, 2008, and 2011) and El Niño years (1973, 1983, 1988, 1992, 1995, 1998, 2003, 2010, 2016, 2019, 2020, and 2024), respectively. Additionally, the correlation between the SVD SST time series and Nino 3.4 index is -0.94, indicating that mode 1 SST provides a strong representation of ENSO.

The mode 1 precipitation time series (Figure 4.2a, green bars) also exhibits coherent positive and negative fluctuations corresponding to La Niña and El Niño events. Moreover, the area-averaged precipitation anomalies over both Central America and Mexico (Figure 3.4a) show strong correlations with the SVD mode 1 precipitation time series, with correlation coefficients of 0.73 and -0.55, respectively.

Both the spatial patterns (Figures 4.1a and 4.1b) and the time evolution (Figure 4.2a) of the first SVD mode suggest a strong relationship between the cold (warm) phase of ENSO and wet (dry) conditions in Central America, as well as dry (wet) conditions in Mexico. This mode explains 60% of the covariance between the SST and precipitation fields (Table 4.1), highlighting the dominant role of ENSO in the covariability between winter tropical SST and CAM precipitation.

The correlation between the SST and precipitation time series for the second SVD mode (Figure 4.2b) is 0.79, well above the 99% significance level. This mode explains 35% of the covariance between the two fields (Table 4.1). Both time series exhibit an upward trend, with the SST transitioning from cold anomalies to warm anomalies in the 1990s. This shift coincides with the unprecedented global warming observed in the late twentieth century (IPCC 2007). In parallel with the SST warming trend, the precipitation time series for mode 2 shows persistent large positive values in the most recent decades (2006–2024). Thus, the second SVD mode links the prolonged drought in CAM in recent decades to the warming of tropical SST. The correlations between the mode 2 precipitation time series and the DJF precipitation time series averaged over Central America and Mexico (Figure 3.4a) are -0.63 and -0.50, respectively, consistent with the negative correlations observed in the spatial pattern of mode 2 precipitation (Figure 4.1d).

The SVD analysis confirms the established relationship between wintertime CAM precipitation and tropical Pacific ENSO SST, as documented in numerous previous studies. It also links the increased intensity of droughts in the CAM region over the last 20 years to the warming of SSTs in the tropical Atlantic, western Pacific, and Indian Ocean. Additionally, the analysis quantifies these relationships and their relative contributions to the variability of CAM winter precipitation (Table 4.1).

4.2 Nonlinearity in the Relationship between Winter CAM Precipitation and ENSO

The SVD analysis reveals the linear relationship between tropical SST and CAM precipitation. To identify potential nonlinearity in the relationship between CAM precipitation and ENSO, composite analysis is conducted for different intensities and phases of ENSO events. If the magnitude or pattern of precipitation anomalies differs significantly between weak and strong ENSO events, or between El Niño and La Niña events, this may suggest a nonlinear relationship.

To classify ENSO events, the Oceanic Niño Index (ONI) is used to quantify the strength of El Niño and La Niña. It is defined as the three-month running mean of SST anomalies in the Niño 3.4 region (5^{o}N–5^{o}S, 120^{o}W–170^{o}W). Table 4.2 presents the criteria for El Niño and La Niña events, as well as for strong and weak events, along with the number of events in each category based on DJF ONI values. A total of 27 warm events and 29 cold events occurred during the 1948–2024 period, including 13 strong El Niño, 14 weak El Niño, 13 strong La Niña and 16 weak La Niña events.

Figure 4.3 shows the composites of DJF SST anomalies for all El Niño and La Niña events, as well as for strong and weak events. Overall, the positive and negative SST anomalies in the eastern and central tropical Pacific are symmetric between the El Niño and La Niña composites for each category. The maximum amplitudes of warm SST anomalies are slightly higher than the cold anomalies, with 1.5 K for all events (Figure 4.3a) and 2 K for strong events (Figure 4.3b), compared to 1.25 K and 1.75 K for cold anomalies in all (Figure 4.3d) and strong (Figure 4.3e) La Niña composites, respectively. The amplitudes of weak events are relatively small, around ±0.75 K (Figures 4.3c, f).

The corresponding composites of DJF CAM precipitation anomalies are shown in Figure 4.4. Consistent with the SVD results (Figure 4.1b), precipitation anomalies are out of phase between Central America and Mexico in the composites for all (Figures 4.4a, d) and strong (Figures 4.4b, e) events, with positive rainfall anomalies in Central America and negative anomalies in Mexico associated with La Niña (Figures 4.4d, e). The overall opposite signs of precipitation anomalies between El Niño and La Niña events (Figures 4.4a, b vs. d, e) indicate that their relationship is largely linear, except in Honduras, where rainfall anomalies remain below normal during both El Niño and La Niña events. However, a closer inspection reveals that the spatial patterns of precipitation anomalies lack symmetry between weak El Niño and La Niña events (Figures 4.4c vs. f), indicating some nonlinearity in their relationship. The nonlinearity is also evident in the non-proportional response of precipitation anomalies (Figures 4.4b vs. c, and 4.4e vs. f) to the intensity of SST anomalies between strong and weak ENSO events (Figures 4.3b vs. c, and 4.3e vs. f).

4.3 Associated Atmospheric Circulations

To understand the physical processes linking CAM precipitation to tropical SST, Figure 4.5 shows the DJF seasonal mean circulation anomalies of 200-hPa height and vorticity, 850-hPa wind, and 925-hPa divergence associated with the SVD mode 1 and mode 2 SSTs. These anomalies are obtained through linear regression of 77 years of data (1948–2024) against the corresponding SVD SST time series. The 200-hPa height anomalies related to mode 1 SST exhibit a typical Pacific/North American (PNA) pattern (Figure 4.5a). This teleconnection pattern is characterized by an anomalous high over the North Pacific, a low over Canada, and another high over the southern U.S., indicating a wave train originating from the tropical Pacific in response to La Niña (Figure 4.1a). The distribution of 200-hPa vorticity anomalies is consistent with the height anomaly pattern.

Associated with mode 2 SST, the 200-hPa height field is dominated by positive anomalies in both tropics and extratropics (Figure 4.5b), consistent with the overall warming of tropical SST (Figure 4.1c). Two wave trains are also visible in both height and vorticity fields: one originating from the tropical western Pacific and Indian Ocean, where the warming signal is strongest, extending across Asia and North America, and another from the tropical eastern Pacific. Positive height anomalies downstream over the CAM region (Figure 4.5b) favor local dry conditions. Additionally, two centers of 925-hPa divergence (Figure 4.5d) coincide with the precipitation deficits in Figure 4.1d. The consistency between the circulation anomalies associated with SST and the precipitation anomalies in CAM suggests that the atmospheric circulation links the variations between tropical SST and CAM precipitation as depicted by the two SVD modes.

Teleconnection circulation patterns are more clearly observed in the 200-hPa stream function anomaly field, as shown in Figure 4.6. Associated with the mode 1 La Niña SST (Figure 4.1a), a wave train originates in the central tropical Pacific and crosses the Pacific/North American region. The stream function anomalies related to the mode 2 SST display two wave trains. One originates from the tropical Indian Ocean, and the other from the eastern tropical Pacific. Downstream over CAM, positive stream function anomalies are dynamically consistent with the rainfall deficits captured by the SVD mode 2 (Figure 4.1d).

Figure 4.7 shows the corresponding 200-hPa velocity potential and divergent wind anomalies, as well as upper-level divergence. Associated with the two leading SVD SST modes, there are positive upper-level velocity potential anomalies over the CAM region. The distribution of upper-level convergence and divergence anomalies is consistent with the distribution of precipitation anomalies in the two SVD modes (Figures 4.1b, d). Both the upper-level stream function and velocity potential enhance the representation of large-scale atmospheric circulation that links tropical SSTs to CAM precipitation. The stream function helps illustrate wave patterns and teleconnections, while the velocity potential highlights divergent flow patterns.

4.4 Relationships between CAM Precipitation and Tropical SSTs in AMIP Simulations

To determine whether the precipitation anomalies identified in the observational analysis (Figures 4.1b, d) are atmospheric responses to tropical SSTs (Figures 4.1a, c), the SVD analysis is also applied to the 18-member ensemble mean DJF CAM precipitation from the AMIP simulations (1957–2018) and the SSTs in the tropical Atlantic and Pacific. The SSTs were prescribed as lower boundary forcing to drive the model atmosphere. Therefore, any signals in the ensemble mean precipitation may indicate a precipitation response to the SSTs.

Figure 4.8 shows the spatial distribution of the homogeneous correlations (Wallace et al., 1992) of the two leading SVD modes for both the wintertime (DJF) SST and precipitation fields. The first SVD mode (Figures 4.8a, b) displays similar SST and precipitation patterns to the observations (Figures 4.1a, b), suggesting that the out-of-phase precipitation anomalies in Central America and Mexico are a response to the ENSO SST. Unlike the correlations in the observations (Figure 4.1a), no large areas of negative correlations are found in the Atlantic (Figure 4.8a). Additionally, the correlations for precipitation in northern Mexico in the model (Figure 4.8b) are stronger than in the observations (Figure 4.1b), likely due to ensemble averaging, which enhances the signal-to-noise ratio.

In the second mode, the SST correlation pattern (Figure 4.8c) also resembles the observations (Figure 4.1c), with positive correlations across the western Pacific, Indian Ocean, and Atlantic. In response to the second mode of tropical SSTs (Figure 4.8c), negative correlations are found in the precipitation field over Central America and southern Mexico (Figure 4.8d), which are also observed in the observational data (Figure 4.1d). However, the negative correlations in northern Mexico seen in the observations are not captured by the second SVD mode of precipitation in the model, where precipitation shows strong correlations in the ENSO-related first SVD mode (Figure 4.8b).

The time series of the two SVD modes are shown in Figure 4.9. Both the SST (red bars) and model precipitation (green bars) exhibit strong interannual variability in the first mode (Figure 4.9a) and an upward trend in the second mode (Figure 4.9b). The correlation between the SST time series of the first mode in the model and observations (red bars, Figures 4.9a and 4.2a) is 0.69 over the common period of 1957–2018, indicating that the ENSO-related mode in the observations is well captured in the AMIP simulations. The correlation between the SST time series of the second mode in the observations (red bars, Figure 4.2b) and the second mode in the AMIP simulations (red bars, Figure 4.9b) is 0.63, exceeding the 99% significance level. The model results (Figures 4.8c, d) suggest that the prolonged droughts in Central America in recent decades (Figure 3.4a) are indeed responses to the warming of SST in the tropical Atlantic, western Pacific, and Indian Ocean.

Table 4.3 summarizes the statistics of the two SVD modes. Together, the two modes account for 98% of the covariance between the SST and precipitation fields, similar to the two leading modes in the observations (95%, Table 4.1). However, the first mode in the AMIP simulations explains 91% of the covariance, much higher than the observations (60%). The correlation between each pair of the SVD time series is highly significant, with correlation coefficients of 0.67 and 0.70. The total SST variance explained by the two modes is 49%, lower than that in the observations (60%). However, the precipitation variance explained by the two modes in the model is much higher than in the observations (77% vs. 41%). The higher percentages of the covariance between mode 1 SST and precipitation (91%) and the precipitation variance (59%) explained by the first SVD mode indicate strong covariations between ENSO and CAM precipitation, highlighting the dominant role of ENSO in driving precipitation in the model. Generally speaking, AMIP models tend to overreact to ENSO and exaggerate the atmospheric response compared to observations. This may also be due to the ensemble averaging, which reduces internal variability and enhances the signal-to-noise ratio (Kumar and Hoerling, 1995).

The SVD analyses were also conducted between DJF tropical SSTs and CAM precipitation from each member of the AMIP simulations. The statistics of the two leading modes were then averaged over the 18 SVD analyses, and the results are included in Table 4.3. Unlike the SVD analysis using the ensemble mean precipitation, the percentage of covariance explained by the first mode decreases from 91% to 82%, and the correlation between the mode 1 SST and precipitation time series drops from 0.67 to 0.57. While the SST variance explained by mode 1 remains nearly the same (40% vs. 39%), the ENSO SST-forced precipitation variance significantly decreases from 59% to 34%. It is clear that the ensemble mean procedure reduces internal atmospheric variability, increases the signal-to-noise ratio, and enhances the covariations between ENSO SST and CAM precipitation.

4.5 Potential Predictability of Winter CAM Precipitation

The observational analysis presented in this chapter suggests that the variability of winter CAM precipitation is strongly linked to tropical Atlantic and Pacific SSTs through the atmospheric circulation. The AMIP simulations further confirm that CAM precipitation associated with tropical SSTs represents atmospheric responses to SST forcing. Thus, tropical SSTs have potential predictive value for CAM precipitation. Given tropical Atlantic and Pacific SST patterns, such as those from operational seasonal climate forecasts, CAM precipitation can be predicted based on the relationships depicted by the SVD analysis. This proposed forecasting method is similar to the approach used by Wang et al. (1999) for predicting U.S. precipitation.

Under the assumption that a coupled global climate model can accurately predict global SSTs, the potential predictability of winter CAM precipitation can be assessed by (a) reconstructing precipitation anomalies based on the SVD SST time series with the target year removed from the training period, and (b) comparing the reconstructed precipitation with observations. First, a regression coefficient is obtained by regressing observed DJF precipitation against the SVD SST time series for each CAM grid point, excluding the target year. Precipitation anomalies for the target year are then reconstructed by multiplying the regression coefficient by the corresponding SVD SST PC values. The process is repeated for each target season, constructing a time series of precipitation anomalies.

Figure 4.10 shows the anomaly correlation between the observed precipitation and the reconstructed precipitation in CAM based on the first two individual SVD SST time series, as well as both modes together. Considerable potential predictability is found in southern Central America, northern and central Mexico, associated with tropical Pacific SST (SVD mode 1, Figure 4.1a), and in Central America, northern and southern Mexico, associated with the warming of tropical SSTs (SVD mode 2, Figure 4.1c). Significant anomaly correlations exceeding the 99% confidence level cover 50% and 41% of CAM for mode 1 and mode 2, respectively. When combining the two modes together (Figure 4.10c), anomaly correlations exceeding the 99% significance level cover 82% of the CAM region. These results suggest significant potential predictability of CAM winter precipitation using tropical SST information.

4.6 Summary

The covariability between winter CAM precipitation and tropical SSTs was objectively identified through SVD analysis. Both tropical Pacific and Atlantic SSTs are linked to the variability in CAM precipitation. The first SVD mode captures ENSO-related precipitation and associates droughts in northern Mexico with La Niña SSTs. The second mode links droughts in Central America to the warming of tropical Atlantic SSTs, as well as to warming in the tropical western Pacific and Indian Ocean. Each SVD precipitation pattern aligns with upper-level atmospheric circulation and low-level wind anomalies associated with the SVD SSTs, demonstrating the atmospheric bridge that links CAM precipitation to tropical SSTs. The SVD analysis shows that 23% of the CAM precipitation variance is related to Pacific SSTs and 18% to

Atlantic SSTs, suggesting that both play significant roles in modulating winter CAM precipitation. Furthermore, the SVD analysis indicates that recent droughts in Central America are linked to the persistent warming of SSTs in the tropical Atlantic, western Pacific, and Indian Ocean. AMIP simulations driven by observed SSTs confirm that these precipitation anomalies in the CAM region are responses to tropical SSTs at interannual and longer time scales. Therefore, tropical SSTs provide a source of predictability for CAM winter precipitation. Given the distribution of tropical SSTs, CAM winter precipitation can be predicted based on its relationship to the SSTs identified by the SVD analysis.

Table 4.1 Statistics of the two leading SVD modes of winter (DJF) tropical Pacific/Atlantic SSTs and CAM precipitation (Pr) based on observational data from 1948 to 2024. These statistics include the percentage of covariance explained by each mode, the temporal correlation between pairs of SVD time series, and the variance explained by each mode for the individual fields.

SVD Mode	Covariance	Correlation	SST Variance	Pr Variance
Mode 1	60%	0.61	41%	23%
Mode 2	35%	0.79	19%	18%

Table 4.2 Number of winter (DJF) El Niño and La Niña events of different intensities based on the DJF Oceanic Niño Index (ONI) values, as defined by NOAA CPC. The ONI data is available at https://origin.cpc.ncep.noaa.gov/products/analysis_monitoring/ensostuff/ONI_v5.php.

ONI for El Niño	All Events ONI $\geq$ 0.5°C	Strong Events ONI $\geq$ 1°C	Weak Events 0.5 $\leq$ ONI < 1°C
El Niño Events	27	13	14
ONI for La Niña	All Events ONI $\leq$ -0.5°C	Strong Events ONI $\leq$ -1°C	Weak Events -1 < ONI $\leq$ -0.5°C
La Niña Events	29	13	16

Table 4.3 Statistics of the two leading SVD modes of winter (DJF) tropical Pacific/Atlantic SSTs and 18-member ensemble mean CAM precipitation (Pr) in AMIP simulations from 1957 to 2018. These statistics include the percentage of covariance explained by each mode, the temporal correlation between pairs of SVD time series, and the variance explained by each mode for the individual fields. Values in parentheses represent the averages from 18 SVD analyses using precipitation data from each member of the AMIP simulations.

SVD Mode	Covariance	Correlation	SST Variance	Pr Variance
Mode 1	91% (82%)	0.67 (0.57)	40% (39%)	59% (34%)
Mode 2	7% (8%)	0.70 (0.59)	9% (9%)	18% (14%)

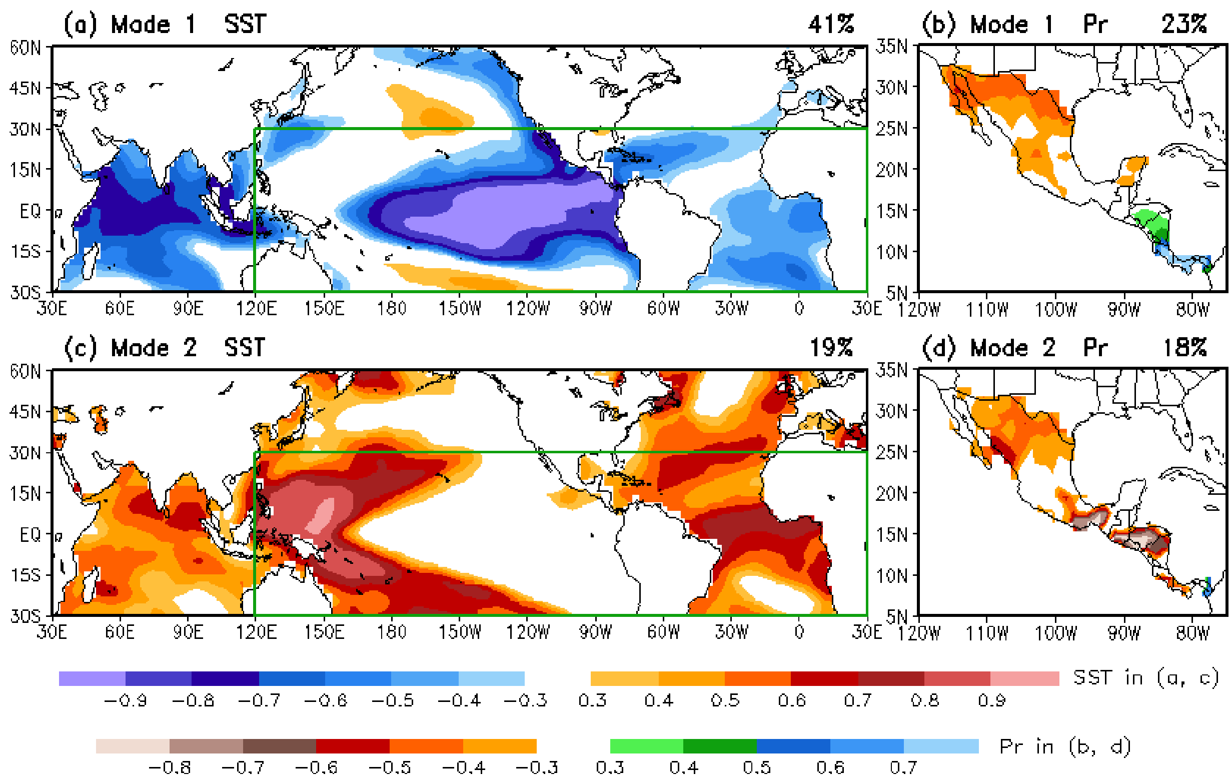

Figure 4.1 Homogeneous correlation maps of (a, b) the first and (c, d) second SVD modes between (a, c) winter (DJF) SSTs in the tropical Pacific and Atlantic and (b, d) precipitation in CAM, based on observational data. The correlations shown in shading (> 0.3) are statistically significant above the 99% confidence level. The percentage of total variance explained by each mode for SST (a, c) and precipitation (b, d) is displayed at the top right of each panel. The green box in (a, c) highlights the tropical Pacific and Atlantic regions where SST data are used in the SVD analysis.

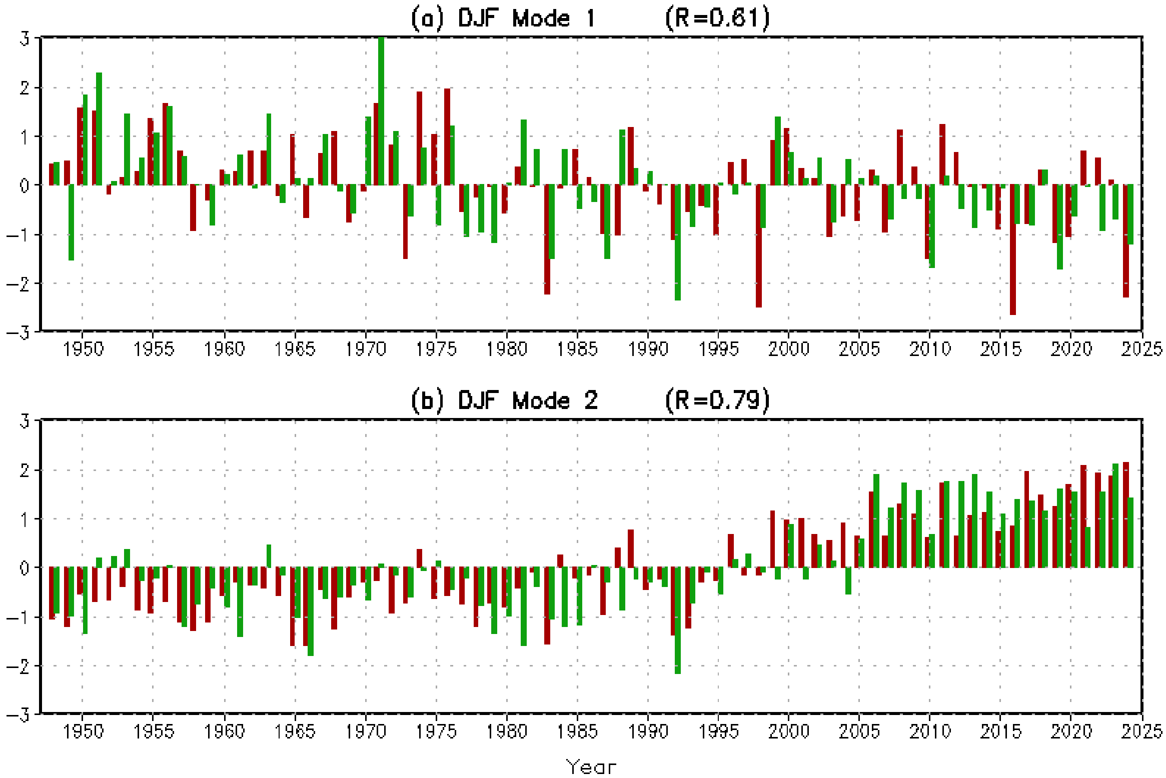

Figure 4.2 Normalized SVD time series of winter (DJF) SST (red bars) and precipitation (green bars) from 1948 to 2024 for (a) the first mode and (b) the second mode. The correlation (R) between each pair of SVD time series is provided at the top of each panel.

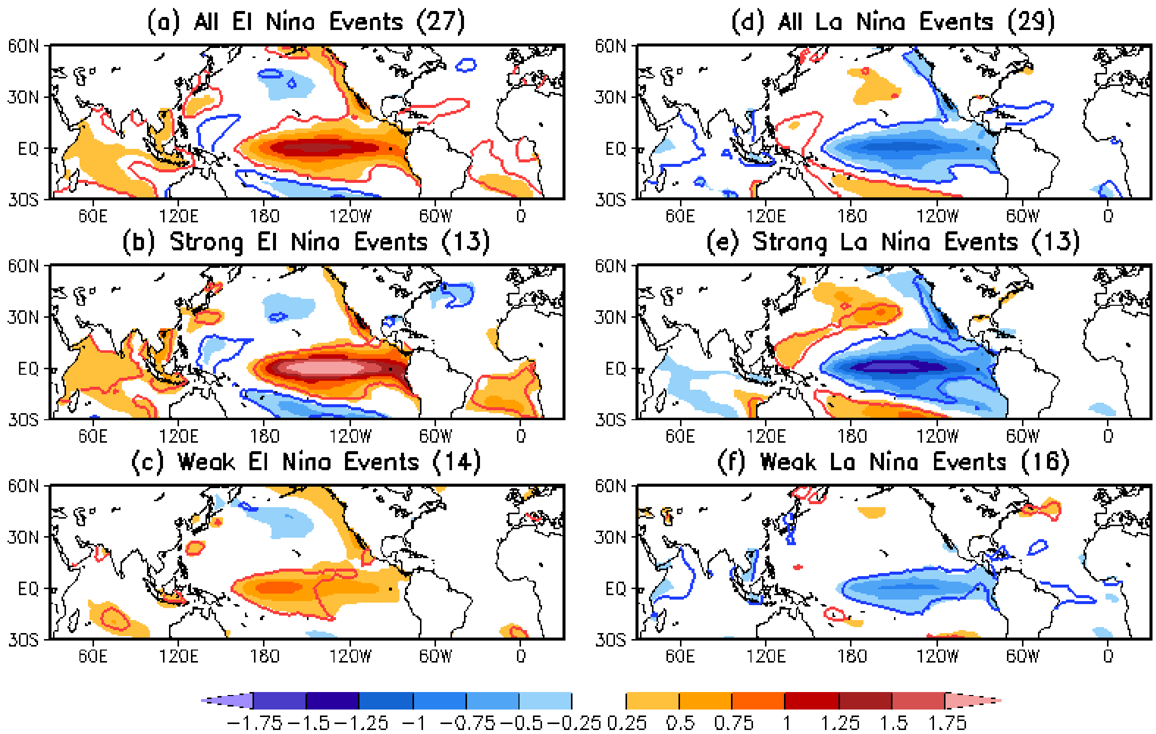

Figure 4.3 Composite of DJF seasonal mean SST anomalies (units: K) for (a) all El Niño, (b) strong El Niño, (c) weak El Niño, (d) all La Niña, (e) strong La Niña, and (f) weak La Niña events. The number of events for each ENSO category is indicated at the top of each panel (in parentheses), as defined by the DJF ONI (Table 4.2). Red and blue contours represent the 99% significance level for positive and negative anomalies, respectively, as determined by the Monte Carol test. To apply the Moving Block Bootstrap method for the Monte Carlo test, the 77 years of data are divided into 7 blocks, each containing 11 consecutive years.

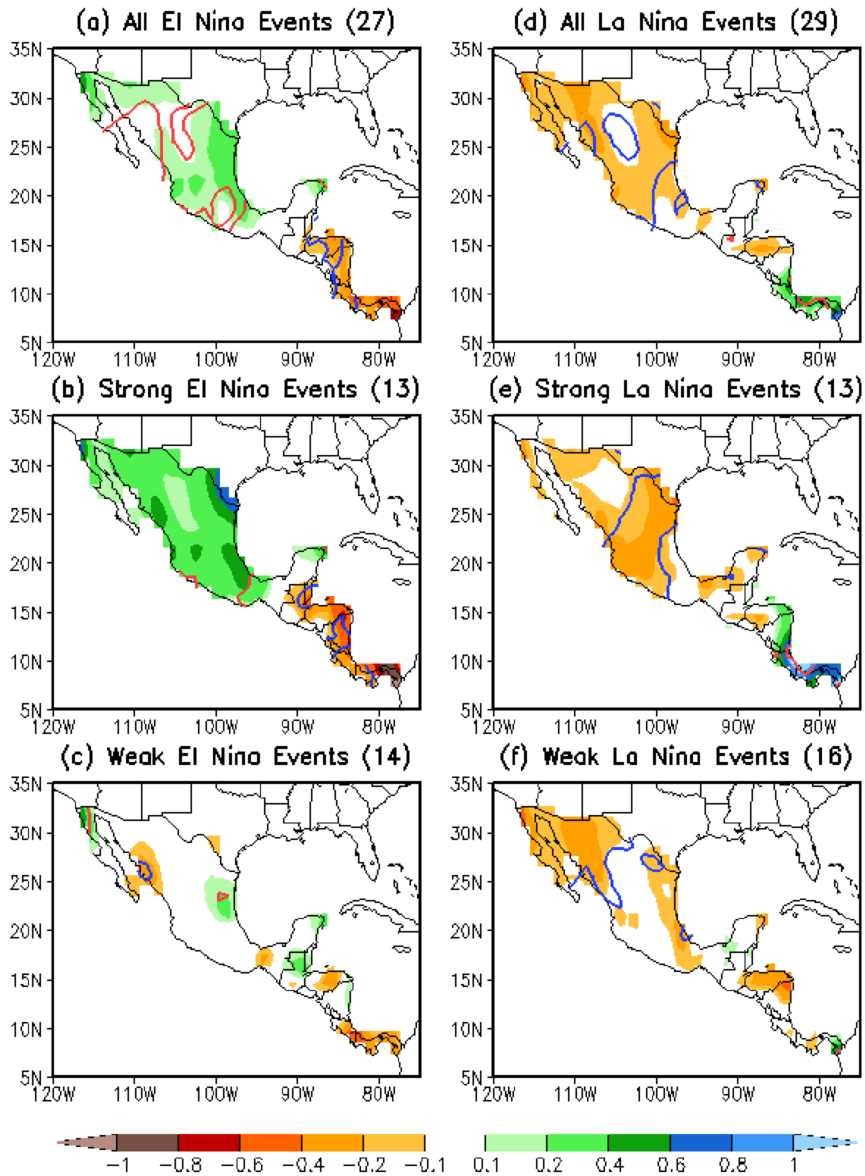

Figure 4.4 Composite of DJF seasonal mean precipitation anomalies (units: mm day^{-1}) for (a) all El Niño, (b) strong El Niño, (c) weak El Niño, (d) all La Niña, (e) strong La Niña, and (f) weak La Niña events. The number of events for each ENSO category is indicated at the top of each panel (in parentheses), as defined by the DJF ONI (Table 4.2). Red and blue contours represent the 99% significance level for positive and negative anomalies, respectively, as determined by the Monte Carol test. To apply the Moving Block Bootstrap method for the Monte Carlo test, the 77 years of data are divided into 7 blocks, each containing 11 consecutive years.

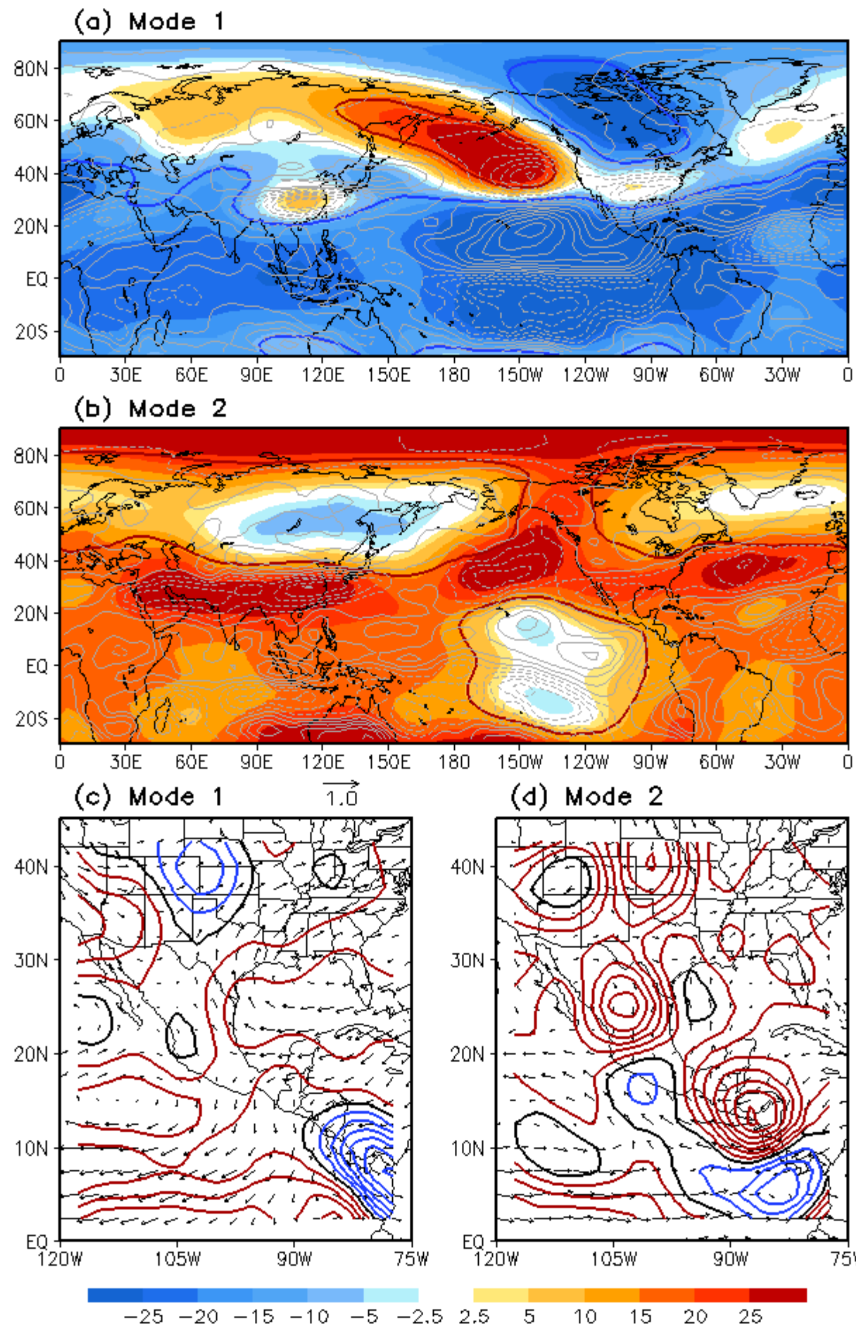

Figure 4.5 Winter (DJF) circulation anomalies of (a, b) 200-hPa height (shading, gpm) and vorticity (contour, s^{-1}), (c, d) 850-hPa wind (vector, m s^{-1}), and 925-hPa divergence (contour, s^{-1}) associated with one standard deviation of the SVD SST time series. The anomalies are obtained through linear regression against the SVD SST time series (red bars in Figure 4.2) for (a, c) mode 1 and (b, d) mode 2 using observational data. The contour interval in (a, b) is 1.0×10^{-6} s^{-1}, with negative values dashed. The contour interval in (c, d) is 2.0×10^{-7} s^{-1}, with positive values in red, negative values in blue, and the zero contour in thick black. The height anomalies circled by red

(positive) and blue (negative) lines in (a, b) are significantly correlated with the SVD SST time series at the 99% confidence level.

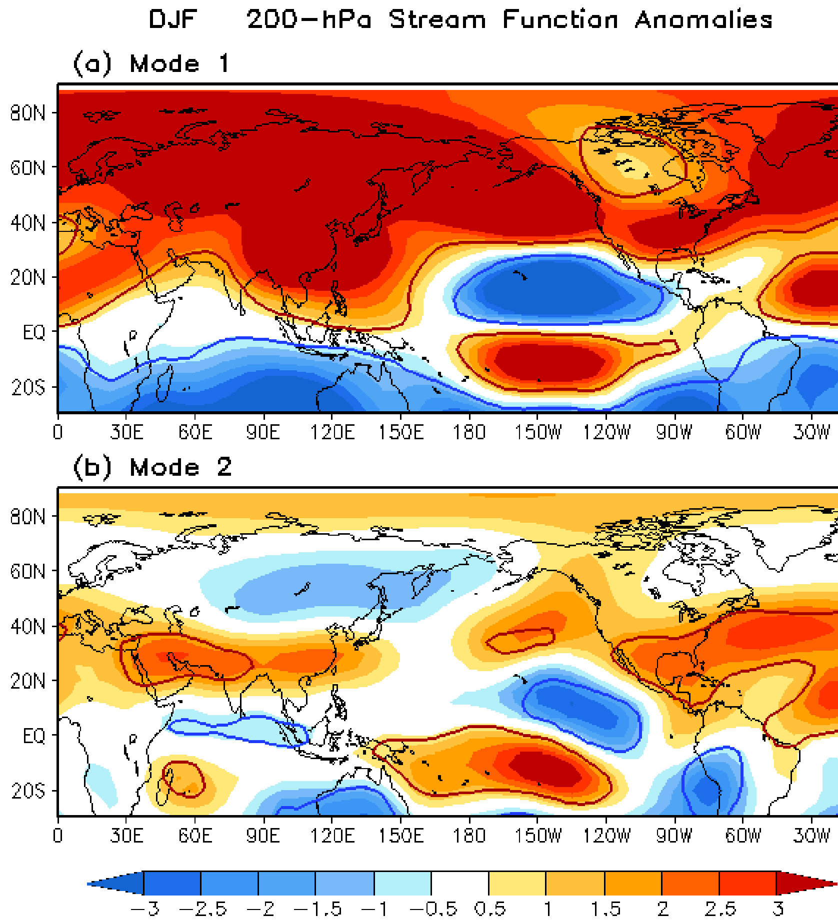

Figure 4.6 Winter (DJF) 200-hPa stream function anomalies (units: 10^6 m^2 s^{-1}) associated with one standard deviation of the SVD SST time series for (a) mode 1 and (b) mode 2. The anomalies are obtained through linear regression against the SVD SST time series (red bars in Figure 4.2) using observational data. The stream function anomalies circled by red (positive) and blue (negative) lines are significantly correlated with the SVD SST time series at the 99% confidence level.

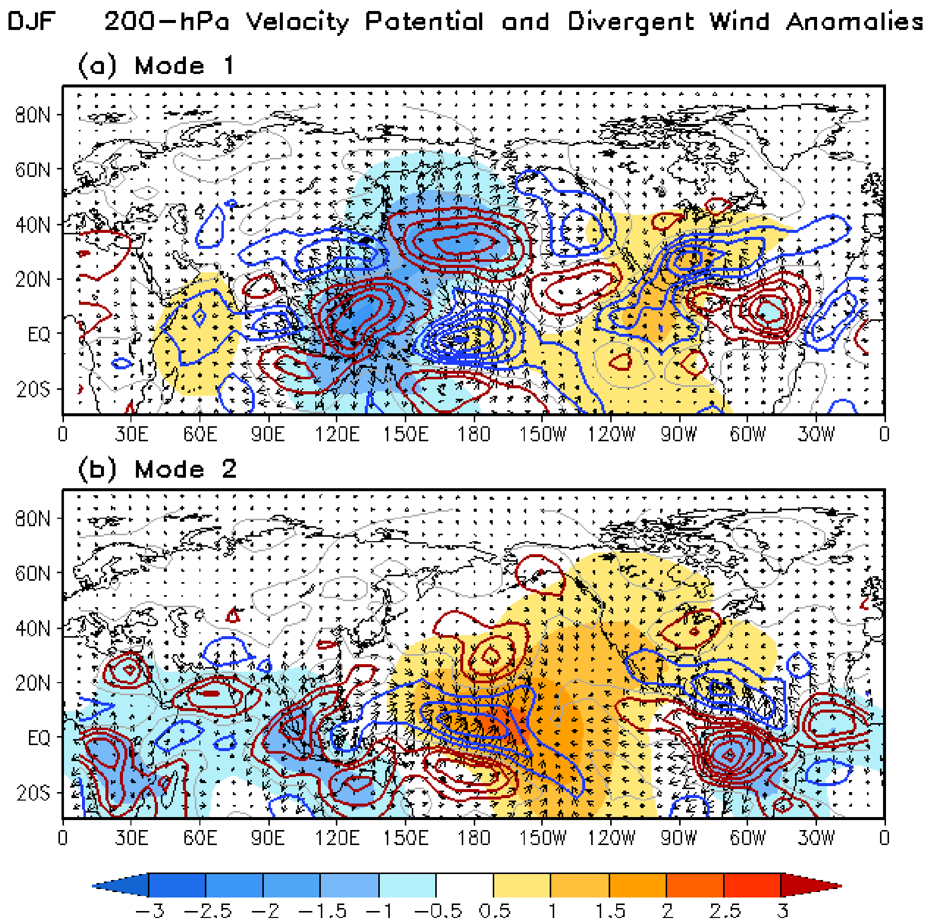

Figure 4.7 Winter (DJF) 200-hPa velocity potential anomalies (shadings, units: 10^6 m) and divergent wind anomalies (vectors, units: m s^{-1}) associated with one standard deviation of the SVD SST time series for (a) mode 1 and (b) mode 2. The anomalies are obtained through linear regression against the SVD SST time series (red bars in Figure 4.2) using observational data. The divergence anomaly field is also shown based on the divergent wind anomalies, with a contour interval of 2×10^{-7} s^{-1}. Positive divergence anomalies are represented by thick red contours, negative anomalies by thick blue contours, and zero divergence by thin gray contour.

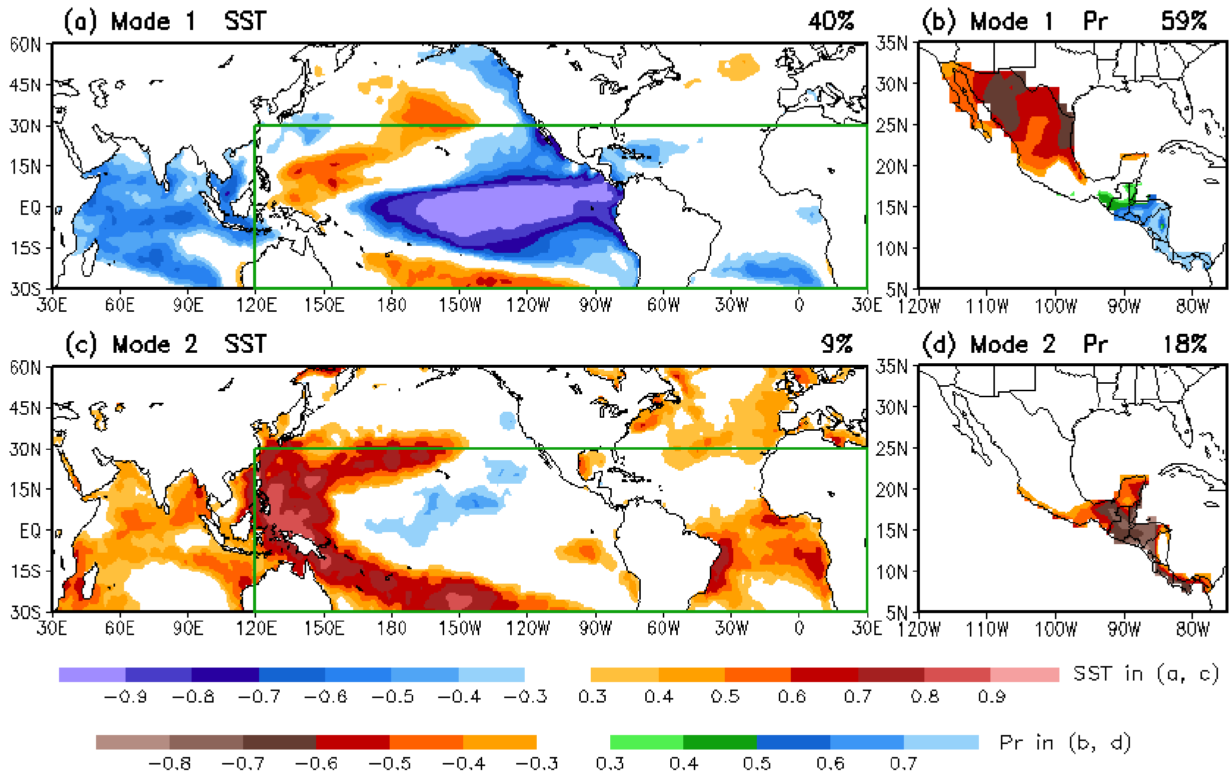

Figure 4.8 Homogeneous correlation maps of (a, b) the first and (c, d) second SVD modes between (a, c) winter (DJF) SST in the tropical Pacific and Atlantic and (b, d) precipitation in CAM based on the 18-member ensemble mean AMIP simulations from 1957 to 2018. The correlations, shown in shadings (> 0.3), are statistically significant above the 99% confidence level. The percentage of total variance explained by each mode for SST (a, c) and precipitation (b, d) is displayed in the top right corner of each panel. The green box in (a, c) highlights the tropical Pacific and Atlantic regions where SST data are used in the SVD analysis.

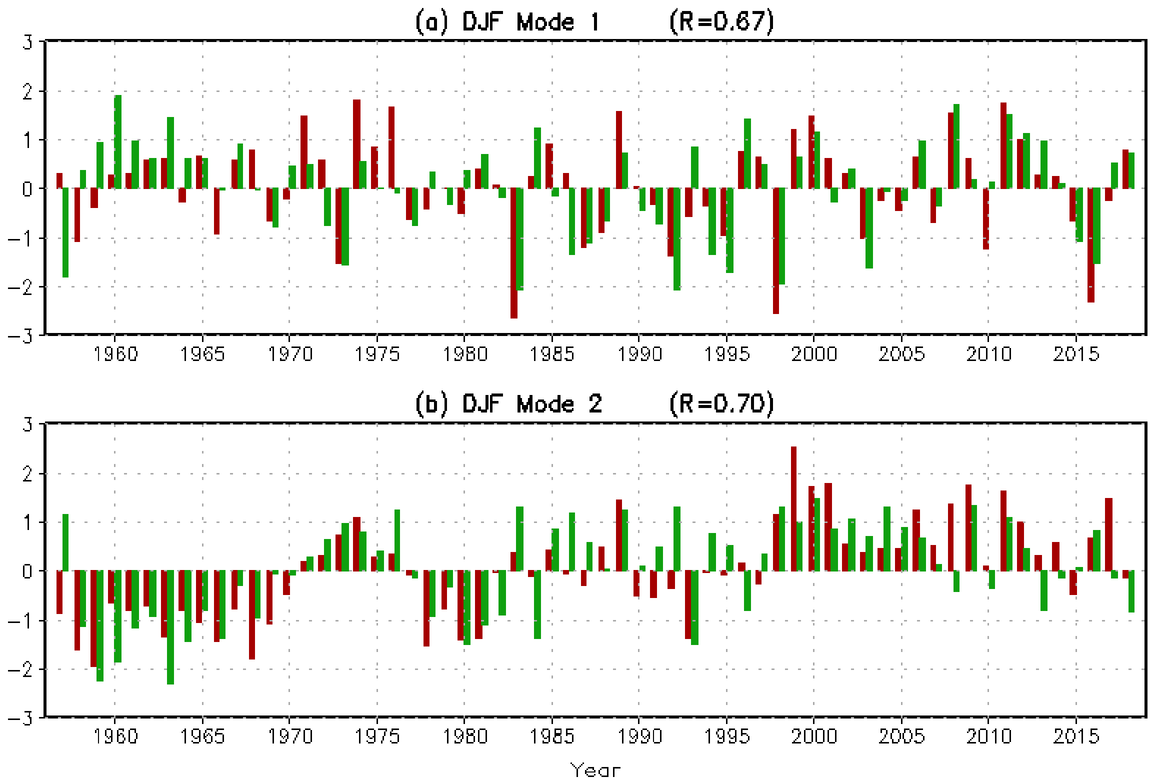

Figure 4.9 Normalized SVD time series of winter (DJF) SST (red bars) and precipitation (green bars) for (a) the first and (b) second modes from the 18-member ensemble mean data of the 1957–2018 AMIP simulations. The correlation (R) between each pair of SVD time series is displayed at the top of each panel.

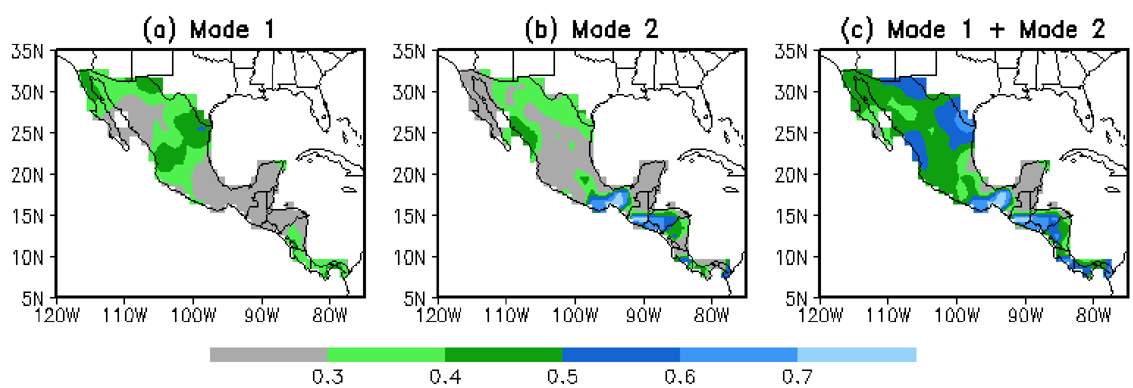

Figure 4.10 Anomaly correlation between observed 1948–2024 DJF precipitation and reconstructed precipitation anomalies based on (a) SVD mode 1 SST time series, (b) SVD mode 2 SST time series, and (c) both mode 1 and mode 2 SST time series. Color shadings denote the correlations greater than 0.3, which are above the 99% significance level.

Chapter 5: Covariability of CAM Precipitation and Tropical SSTs in Summer

The objectives of this chapter are to document and analyze the relationships between summertime CAM precipitation and SSTs in the tropical Pacific and Atlantic. The analysis methods are similar to those used in Chapter 4. Section 5.1 presents the results of the SVD analysis on summer (JJA) precipitation and SSTs, with a discussion on the relative importance of tropical Pacific and Atlantic SSTs. Section 5.2 examines the nonlinearity in the relationship between summer precipitation and ENSO SST. Section 5.3 explores the atmospheric circulation associated with the leading SST and precipitation SVD modes. Section 5.4 investigates AMIP model simulations to verify whether the observed relationships are the atmospheric response to tropical SST forcing. The potential predictability of summer precipitation based on tropical SSTs is discussed in Section 5.5. Finally, a summary is provided in Section 5.6.

5.1 Observed Relationships between Summer CAM Precipitation and Tropical SSTs

The relationships between CAM summer precipitation and tropical SSTs are also examined using the SVD method. Table 5.1 presents the statistics for the first two SVD modes. Together, these two modes explain 88% of the covariance between the SST and precipitation fields, accounting for 54% of the variance in SST and 40% in precipitation.

SVD mode 1 SST (Figure 5.1a) is characterized by positive correlations across the tropical oceans, indicating warming of the tropics when the SVD SST time series is positive. The strongest signals (highest correlations) are observed in the eastern tropical Pacific and Indian Oceans, which contrasts with winter, where the strongest signals are found in the western tropical Pacific (Figure 4.1c). Mode 1 precipitation shows large negative correlations in Central America and along

Mexico's Pacific coast (Figure 5.1b). Thus, tropical warming is associated with a decrease in precipitation in these regions. The first SVD mode explains 66% of the covariance between tropical SST and CAM precipitation, and 32% and 25% of variance for individual SST and precipitation fields, respectively (Table 5.1). These results highlight a strong link between tropical ocean warming and drought conditions over CAM.

Mode 2 SST exhibits an El Niño pattern in the tropical Pacific, along with negative correlations in the Atlantic (Figure 5.1c). The associated mode 2 precipitation shows significant negative correlations in Mexico (Figure 5.1d). This second SVD mode links drier summers in Mexico to El Niño SSTs in the tropical Pacific and colder SSTs in the tropical Atlantic. It explains 22% of the covariance between tropical SSTs and CAM precipitation (Table 5.1). Unlike the dominate covariation between ENSO and CAM precipitation in winter, their relationship becomes secondary during the summer. The second SVD mode accounts for 22% of the variance in SST and 15% of the variance in precipitation.

Figure 5.2 displays two pairs of normalized time series of SST and precipitation for the two SVD modes. The correlation between the SVD SST and precipitation time series is 0.62 for mode 1 (Figure 5.2a). Both the SST and precipitation time series show a dominant upward trend, reflecting persistent warm SST anomalies in the tropical oceans (Figure 5.1a) starting in the 1990s, along with prolonged summer rainfall deficits in Central America and southern and western Mexico (Figure 5.1b) since 2000. The correlations of the mode 1 precipitation time series (Figure 5.2a, green bars) with the area-averaged summer precipitation time series over Central America and Mexico (Figure 3.8a) are highly significant, with values of -0.86 and -0.68, respectively. The dry conditions in Central America are more closely related to tropical warming than the dry conditions in Mexico.

Both the mode 2 SST and precipitation time series show consistent interannual fluctuations in most summers (Figure 5.2b), with a correlation coefficient of 0.56 between them (Table 5.1), which exceeds the 99% significance level. The correlation between the mode 2 SST time series (Figure 5.2b, red bars) and the summer Niño 3.4 index is 0.73, also highly significant. Specifically, all strong summer El Niño events with a JJA Nino 3.4 SST index greater than 1^{o}C (e.g., CPC, 2024), including 1957, 1965, 1972, 1987, 1997, 2015, and 2023, project onto the SVD mode 2 SST pattern (Figure 5.1c) with a projection coefficient greater than or close to one standard deviation (Figure 5.2b). It is also true for strong summer La Niña events (1973, 1975, 1988, 1999, and 2010).

The correlations of the mode 2 precipitation time series (Figure 5.2b, green bars) with the area-averaged summer precipitation time series over Central America and Mexico (Figure 3.8a) are -0.37 and -0.77, respectively. Mode 2 suggests a strong association between the ENSO SST and summer precipitation in Mexico, the summer monsoon region, but a weak connection with precipitation in Central America.

The SVD analysis indicates that summer precipitation in Mexico covaries with both the long-term trend and interannual changes in SST, while precipitation in Central America primarily covaries with the long-term trend in tropical SST. Additionally, the SVD analysis reveals that the SST warming trend dominates the covariability with CAM precipitation in summer, in contrast to the dominance of the ENSO SST in winter.

5.2 Nonlinearity in the Relationship between Summer CAM Precipitation and ENSO

Composite analysis of JJA precipitation for different ENSO phases and intensities is used to examine the potential nonlinear relationship between summer CAM precipitation and ENSO. For the summer season, ENSO is classified into El Niño and La Niña phases, as well as strong and weak events, based on the JJA ONI value (Table 5.2). Over the 1948–2024 period, there are a total of 17 warm events (ONI ≥ 0.5 ºC) and 19 cold events (ONI ≤ -0.5 ºC), which is fewer than the totals observed during the winter season (27 and 29, respectively),. Among these, seven are classified as strong El Niño (ONI ≥ 1 ºC), 10 as weak El Niño (0.5 ºC ≤ ONI < 1 ºC), five as strong La Niña (ONI ≤ -1 ºC), and 14 as weak La Niña (-1 ºC < ONI ≤ -0.5 ºC), as summarized in Table 5.2. The number of strong events is lower than the number of weak events in summer, while in winter, the counts are closer (Table 4.2).

Figure 5.3 shows the composites of JJA SST anomalies for both El Niño and La Niña events, as well as for strong and weak events. In general, cold SST anomalies in the eastern and central tropical Pacific during La Niña (Figure 5.3, right panels) span a broader meridional domain than the warm anomalies during El Niño (Figure 5.3, left panels). Additionally, the maximum SST anomalies are closer to the coast of South America in summer, particularly in all El Niño and strong El Niño composites (Figures 5.3a, b), compared to the winter season (Figure 4.3). The intensities (maximum SST anomalies) of all warm events and strong warm events (Figures 5.3a, b) are higher than those of the corresponding cold events (Figures 5.3d, e), but lower for weak warm events (Figure 5.3c) compared to weak cold events (Figure 5.3f). The asymmetry between the El Niño and La Niña composites for all categories is more pronounced in summer (Figure 5.3) than in winter (Figure 4.3).

Composites of summer precipitation for different ENSO categories are shown in Figure 5.4. The dominant drier conditions across CAM during El Niño (Figure 5.4, left panels) and wetter conditions during La Niña (Figure 5.4, right panels) are consistent with the linear relationship between ENSO and summer CAM precipitation identified by the SVD analysis (Figures 5.1c, d). However, significant changes in the rainfall anomaly patterns between warm and cold events (e.g., Figures 5.4b vs. e) and the non-proportional change in magnitude between weak and strong events (e.g., Figures 5.4b vs. c) suggest nonlinearity in the relationship between summer CAM precipitation and ENSO. The asymmetry and non-proportional responses in the precipitation anomalies may also be partially attributed to the asymmetry in the tropical Pacific SST anomalies between warm and cold events (Figure 5.3).

5.3 Associated Atmospheric Circulations

Figure 5.5 shows the JJA seasonal mean circulation anomalies for 200-hPa height and vorticity, 850-hPa wind, and 925-hPa divergence associated with the SVD mode 1 and mode 2 SSTs. The 200-hPa height field associated with mode 1 SST exhibits positive height anomalies across most regions, except for northeast Asia (Figure 5.5a), primarily driven by the general warming of SSTs in SVD mode 1 (Figure 5.1a). The corresponding vorticity field, however, shows less defined wave patterns.

For mode 2 SST, a wave train is observed over the PNA region in both the 200-hPa height and vorticity fields (Figure 5.5b). In general, the summer upper-level circulations, including the 200-hPa stream function (not shown), are characterized by smaller-scale features compared to the winter season. At the lower level (Figures 5.5c, d), the 925-hPa divergence anomalies align with the negative precipitation anomalies observed in both SVD modes (Figures 5.1b, d).

5.4 Relationships between CAM Precipitation and Tropical SSTs in AMIP Simulations

The SVD method was applied to summer (JJA) CAM precipitation in the AMIP simulations, which are forced by summer SSTs. Figure 5.6 shows the spatial distribution of the homogeneous correlations (Wallace et al., 1992) for the two leading SVD modes of summer SSTs and CAM precipitation. The first SVD mode (Figures 5.6a, b) displays an El Niño SST pattern and negative correlations for precipitation in central CAM and northeastern Mexico. This suggests that the negative precipitation anomalies in these regions are a response to the El Niño SST pattern. The ENSO-affected regions in the model are similar to those in observations, although they correspond to the second SVD mode in the observations (Figures 5.1c, d). Notably, unlike the observations (Figure 5.1c), no significant negative correlations are found in the Atlantic in the model (Figure 5.6a).

The second mode in the model (Figure 5.6c) displays an SST correlation pattern similar to the first SVD model in the observations (Figure 5.1a), with positive correlations across the tropical Pacific, Indian Ocean, and Atlantic. In response to this second mode of tropical SSTs (Figure 5.6c), negative correlations are observed in the precipitation field over the western Mexico (Figure 5.6d), which also appear in the observational data (Figure 5.1b). However, the negative correlations in the eastern Mexico found in the model are not seen in the observations.

The time series of the two SVD modes are presented in Figure 5.7. Both the SST (red bars) and model precipitation (green bars) exhibit interannual variability in the first mode (Figure 5.7a) and an upward trend in the second mode (Figure 5.7b). The correlation between the SST time series of the first mode in the model and the second mode in the observations (red bars, Figures 5.7a and 5.2b) is 0.48 over the common period of 1957–2018. Similarly, the correlation between the SST time series of the second mode in the model (red bars, Figure 5.7b) and the first mode in the observation (red bars, Figure 5.2a) is 0.40, exceeding the 99% significance level. These results indicate that both the ENSO and warming trend related SST-precipitation relationships identified in the observations (Figures 5.1, 5.2) are partially reproduced by the AMIP simulations, suggesting tropical SST forcing to the summer CAM precipitation.

Table 4.3 summarizes the statistics for the two SVD modes. Together, the two modes account for 82% of the covariance between the SST and precipitation fields, which is close to the two leading modes in the observations (88%, Table 5.1). However, in the AMIP simulations, the first mode explains 53% of the covariance, which is lower than the 66% explained in the observations. The correlations between each pair of the SVD time series are also lower, though statistically significant, with correlation coefficients of 0.51 and 0.57. The total SST variance explained by the two modes is 37%, which is lower than the 54% in the observations. On the other hand, the precipitation variance explained by the two modes in the model is considerably higher than in the observations (64% vs. 40%).

The most significant difference between the AMIP simulations and the observations is that the first SVD mode in the model is associated with ENSO, whereas in the observations, it is linked to the warming trend. The higher covariance percentage between mode 1 ENSO SST and precipitation (53%), as well as the higher precipitation variance explained (45%), suggests a strong relationship between ENSO and CAM precipitation, emphasizing ENSO's dominant role in driving precipitation in the model. In contrast, the second SVD mode in the observations explains 22% of the covariance between ENSO SST and precipitation, with a 15% related variance for precipitation (Table 5.1).

One possible explanation for the warming trend-related mode being the second mode in the model is that the AMIP simulations were terminated in 2018, thus excluding the most recent hot years, which weakens the warming trend. While updated AMIP simulations are available, they cover a shorter period starting from 1981. Additionally, there are systematic differences between the two sets of simulations over the overlapping period. As a result, the two datasets cannot be combined.

The SVD analysis was also performed between tropical JJA SSTs and CAM precipitation from each member of the AMIP simulations. The statistics of the two leading modes were averaged over the 18 individual SVD analyses, with the results presented in Table 5.3. In contrast to the analysis using the ensemble mean precipitation, the percentage of covariance explained by the first mode decreases slightly from 53% to 48%, and the correlation between mode 1 SST and precipitation time series drops from 0.51 to 0.44. Although the SST variance explained by mode 1 remains nearly the same (13% vs. 14%), the ENSO SST-forced precipitation variance decreases from 45% to 37%. This suggests that the ensemble mean approach reduces internal atmospheric variability, increasing the signal-to-noise ratio and enhancing the covariations between ENSO SST and CAM precipitation.

5.5 Potential Predictability of Summer CAM Precipitation

The potential predictability of summer CAM precipitation is examined in the same way as for winter CAM precipitation described in Section 4.5, based on its relationship with tropical SSTs identified in Section 5.1. Figure 5.8 shows the anomaly correlation between observed precipitation and reconstructed precipitation in CAM based on the first two individual SVD SST time series, as well as both modes combined. Considerable potential predictability is found in Central America and the western coast of Mexico, associated with the warming of tropical SSTs (SVD mode 1, Figure 5.1a), and in central Mexico, associated with the tropical Pacific ENSO SST (SVD mode 2, Figure 5.1c). These regions align with those where precipitation exhibits strong correlations in the two leading SVD modes (Figures 5.1b, d). Significant anomaly correlations exceeding the 99% confidence level cover 36% and 22% of CAM for mode 1 and mode 2, respectively. When combining the two modes together (Figure 5.8c), anomaly correlations exceeding the 99% significance level cover 60% of the CAM region, lower than winter (82%). These results suggest a certain potential predictability of CAM summer precipitation based on the distribution of tropical SSTs.

5.6 Summary

This chapter examined the relationships between summer CAM precipitation and tropical SSTs in both observational data and AMIP simulations. Using the SVD analysis method, we identified two primary modes of covariability between tropical SSTs and CAM precipitation during the summer seasons. The first mode, characterized by tropical ocean warming, accounts for a substantial portion of the observed variance in both SST and precipitation, with a strong correlation to drought conditions over Central America. The second mode, related to the El Niño phenomenon, plays a secondary role, particularly affecting summer precipitation patterns in Mexico.

The analysis revealed that the summer precipitation patterns in CAM are influenced by both long-term trends in tropical SSTs and interannual fluctuations, especially those related to ENSO events. While the observed relationships between ENSO and precipitation in the region are robust, the SVD analysis showed that the summer link between tropical SSTs and precipitation differs from the winter season, with the warming trend in tropical SSTs dominating the covariability in summer. Additionally, the study highlighted the nonlinear relationship between summer precipitation and ENSO, with significant asymmetries in the precipitation response to strong and weak ENSO events.

In the AMIP simulations, the observed tropical SST–precipitation relationships were largely reproduced, with the model capturing the influence of both ENSO and long-term warming trends. However, there were notable differences between the model and observations, particularly in the dominance of ENSO in the first mode of the simulations. The model's lower explained variance in SSTs and higher explained variance in precipitation indicated differences in how the simulated atmosphere responds to tropical SST forcing compared to the observations.

Finally, the potential predictability of summer CAM precipitation was assessed, showing that regions with strong correlations to the leading SVD modes of tropical SSTs have a notable degree of predictability. Central America and the western coast of Mexico, areas most strongly influenced by the SST warming trend, exhibited the highest potential for predictability based on tropical SST anomalies. Overall, this chapter underscores the importance of tropical SSTs, particularly those in the Pacific and Atlantic, as key drivers of summer precipitation patterns in Central America and Mexico, with implications for seasonal precipitation prediction in the region.

Table 5.1 Statistics of the two leading SVD modes of summer (JJA) tropical Pacific/Atlantic SSTs and CAM precipitation (Pr) based on observational data from 1948 to 2024. These statistics include the percentage of covariance explained by each mode, the temporal correlation between pairs of SVD time series, and the variance explained by each mode for the individual fields.

SVD Mode	Covariance	Correlation	SST Variance	Pr Variance
Mode 1	66%	0.62	32%	25%
Mode 2	22%	0.56	22%	15%

Table 5.2 Number of summer (JJA) El Niño and La Niña events of different intensities based on the JJA Oceanic Nino Index (ONI) values, as defined by NOAA CPC. The ONI data is available at https://origin.cpc.ncep.noaa.gov/products/analysis_monitoring/ensostuff/ONI_v5.php.

ONI for El Niño	All Events ONI ≥ 0.5ºC	Strong Events ONI ≥ 1ºC	Weak Events 0.5 ≤ ONI < 1ºC
El Niño Events	17	7	10
ONI for La Niña	All Events ONI ≤ -0.5ºC	Strong Events ONI ≤ -1ºC	Weak Events -1 < ONI ≤ -0.5ºC
La Niña Events	19	5	14

Table 5.3 Statistics of the two leading SVD modes of summer (JJA) tropical Pacific/Atlantic SSTs and 18-member ensemble mean CAM precipitation (Pr) in AMIP simulations from 1957 to 2018. These statistics include the percentage of covariance explained by each mode, the temporal correlation between pairs of SVD time series, and the variance explained by each mode for the individual fields. Values in parentheses represent the averages from 18 SVD analyses using precipitation data from each member of the AMIP simulations.

SVD Mode	Covariance	Correlation	SST Variance	Pr Variance
Mode 1	53% (48%)	0.51 (0.44)	13% (14%)	45% (37%)
Mode 2	29% (28%)	0.57 (0.49)	24% (24%)	19% (15%)

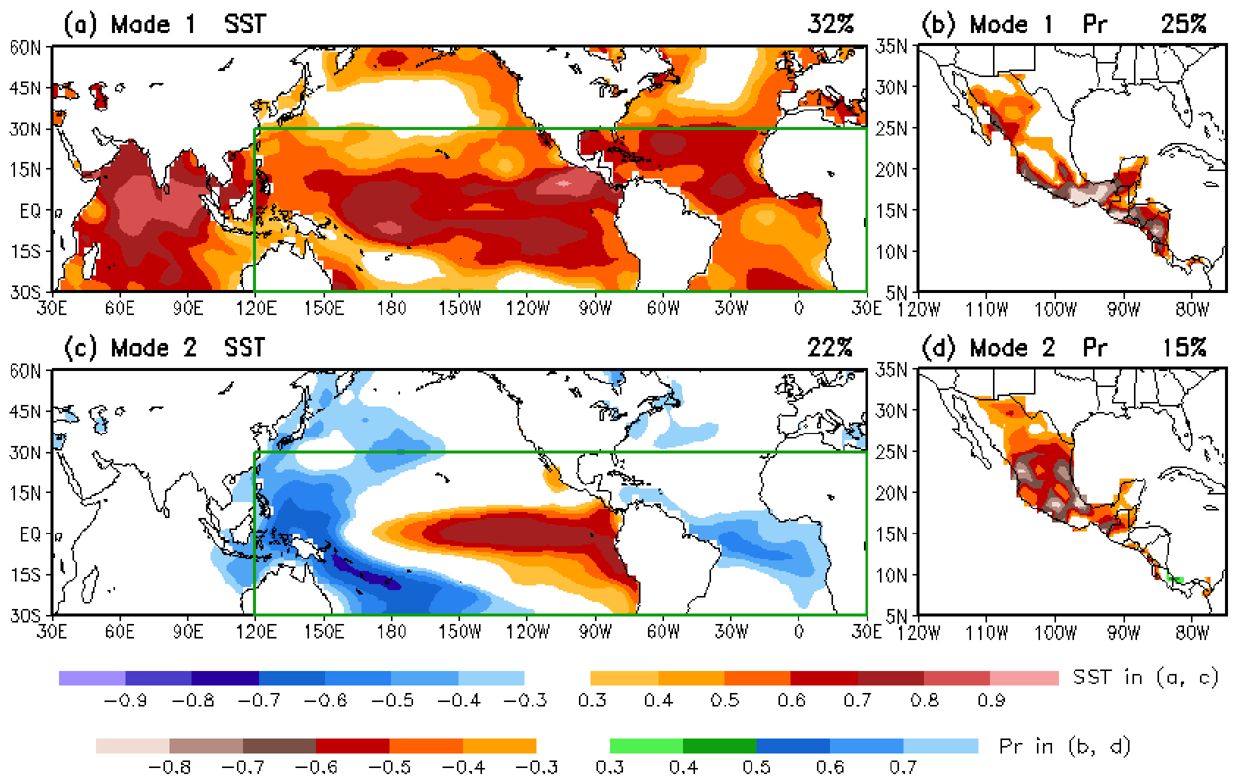

Figure 5.1 Homogeneous correlation maps of (a, b) the first and (c, d) second SVD modes between (a, c) summer (JJA) SSTs in the tropical Pacific and Atlantic and (b, d) precipitation in CAM, based on observational data. The correlations shown in shading (> 0.3) are statistically significant above the 99% confidence level. The percentage of total variance explained by each mode for SST (a, c) and precipitation (b, d) is displayed at the top right of each panel. The green box in (a, c) highlights the tropical Pacific and Atlantic regions where SST data are used in the SVD analysis.

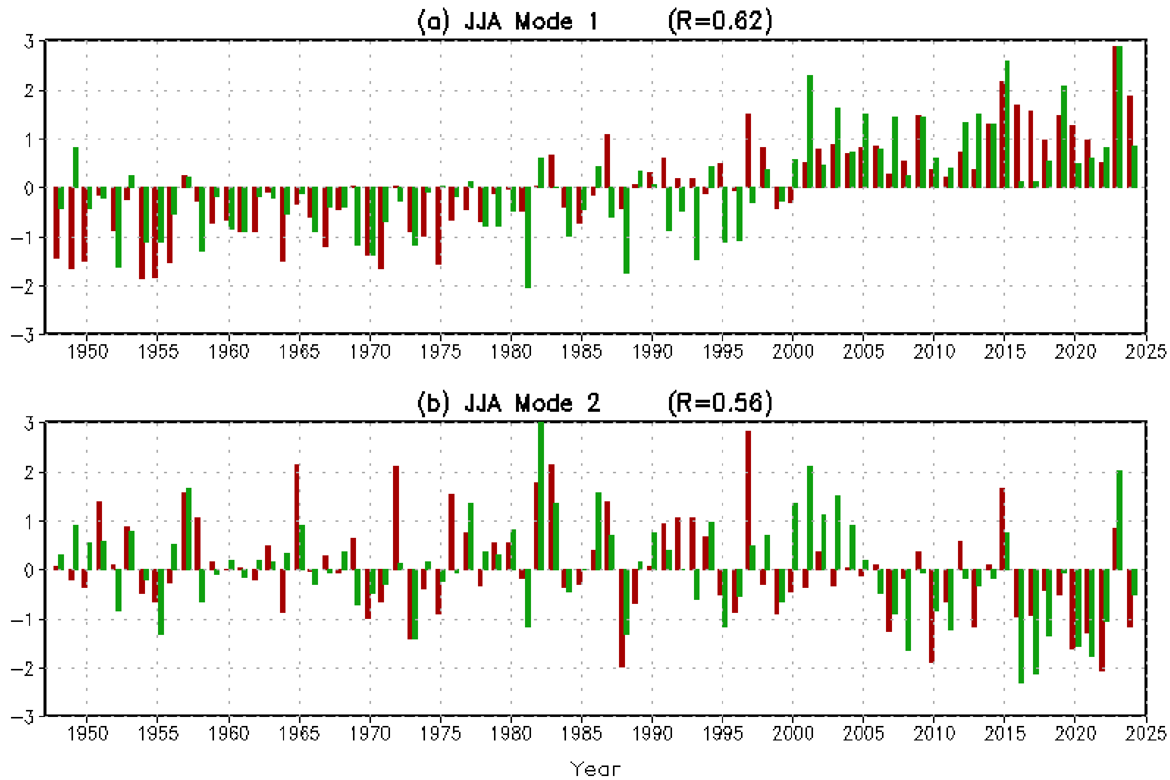

Figure 5.2 Normalized SVD time series of summer (JJA) SST (red bars) and precipitation (green bars) from 1948 to 2024 for (a) the first mode and (b) the second mode. The correlation (R) between each pair of SVD time series is provided at the top of each panel.

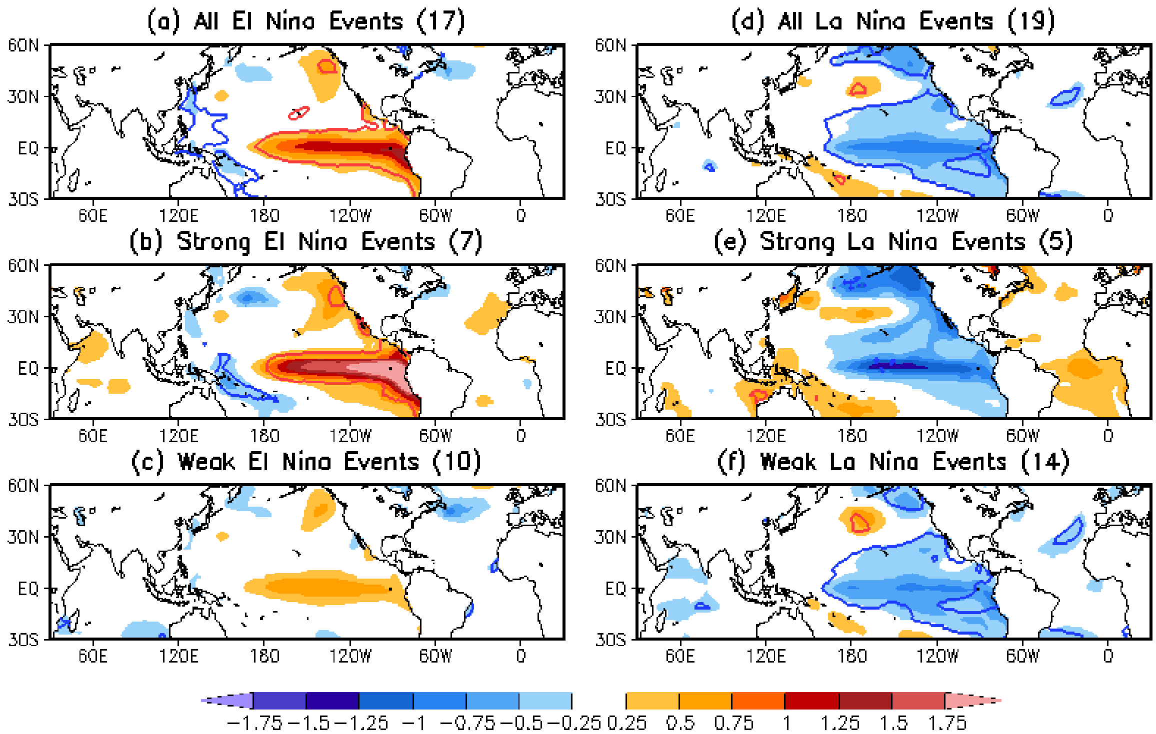

Figure 5.3 Composite of JJA seasonal mean SST anomalies (units: K) for (a) all El Niño, (b) strong El Niño, (c) weak El Niño, (d) all La Niña, (e) strong La Niña, and (f) weak La Niña events. The number of events for each ENSO category is indicated at the top of each panel (in parentheses), as defined by the JJA ONI (Table 5.2). Red and blue contours represent the 99% significance level for positive and negative anomalies, respectively, as determined by the Monte Carol test. To apply the Moving Block Bootstrap method for the Monte Carlo test, the 77 years of data are divided into 7 blocks, each containing 11 consecutive years.

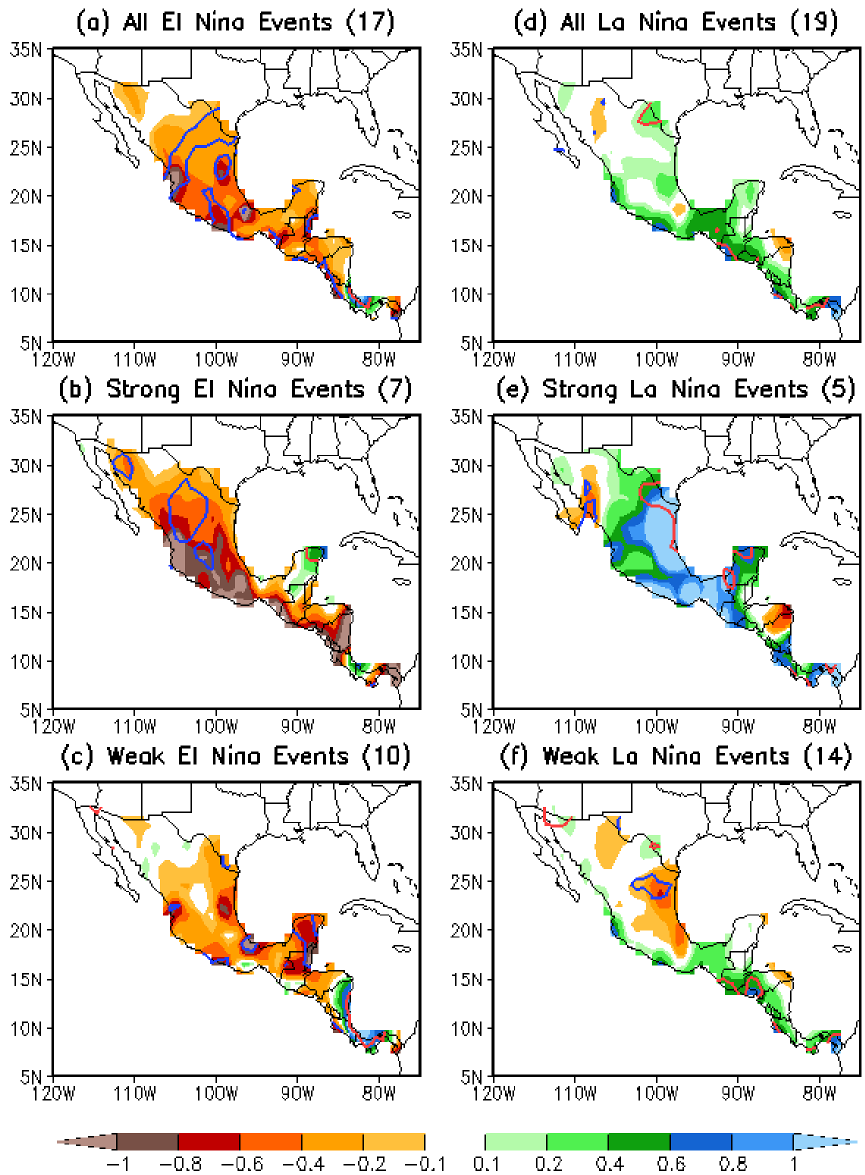

Figure 5.4 Composite of JJA seasonal mean precipitation anomalies (units: mm day^{-1}) for (a) all El Niño, (b) strong El Niño, (c) weak El Niño, (d) all La Niña, (e) strong La Niña, and (f) weak La Niña events. The number of events for each ENSO category is indicated at the top of each panel (in parentheses), as defined by the JJA ONI (Table 5.2). Red and blue contours represent the 99% significance level for positive and negative anomalies, respectively, as determined by the Monte Carol test. To apply the Moving Block Bootstrap method for the Monte Carlo test, the 77 years of data are divided into 7 blocks, each containing 11 consecutive years.

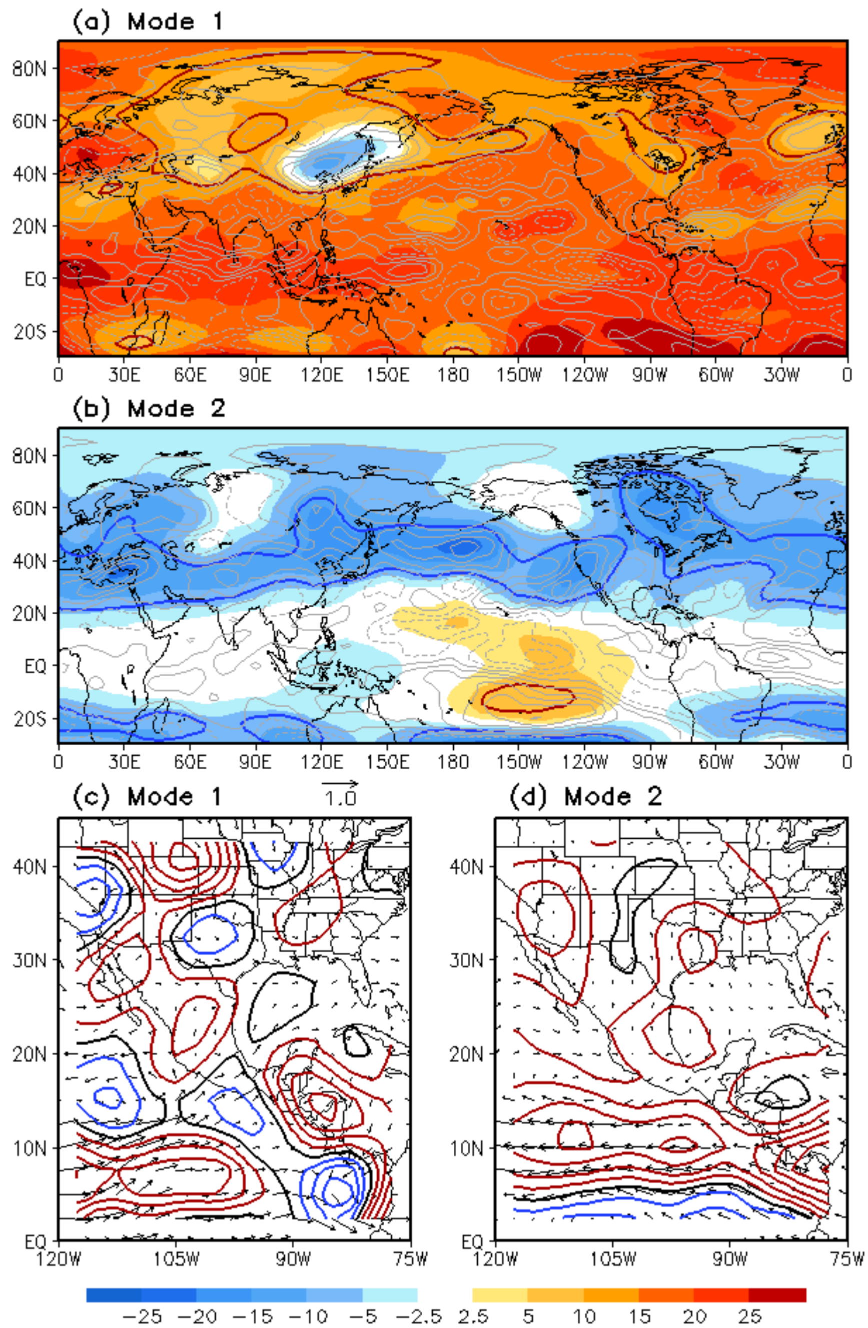

Figure 5.5 Summer (JJA) circulation anomalies of (a, b) 200-hPa height (shading, gpm) and vorticity (contour, s^{-1}), (c, d) 850-hPa wind (vector, m s^{-1}), and 925-hPa divergence (contour, s^{-1}) associated with one standard deviation of the SVD SST time series. The anomalies are obtained through linear regression against the SVD SST time series (red bars in Figure 5.2) for (a, c) mode 1 and (b, d) mode 2 using observational data. The contour interval in (a, b) is 1.0×10^{-6} s^{-1}, with negative values dashed. The contour interval in (c, d) is 2.0×10^{-7} s^{-1}, with positive values in red, negative values in blue, and the zero contour in thick black. The height anomalies circled by red

(positive) and blue (negative) lines in (a, b) are significantly correlated with the SVD SST time series at the 99% confidence level.

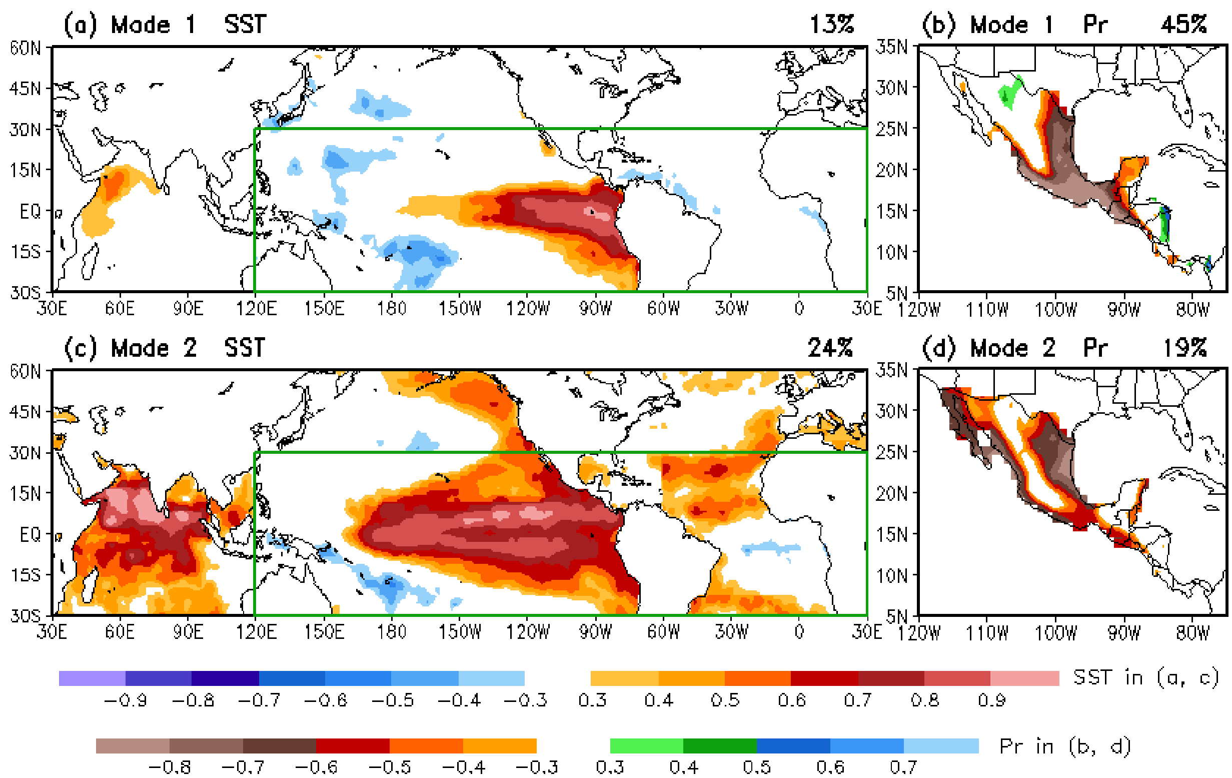

Figure 5.6 Homogeneous correlation maps of (a, b) the first and (c, d) second SVD modes between (a, c) summer (JJA) SST in the tropical Pacific and Atlantic and (b, d) precipitation in CAM based on the 18-member ensemble mean AMIP simulations from 1957 to 2018. The correlations, shown in shadings (> 0.3), are statistically significant above the 99% confidence level. The percentage of total variance explained by each mode for SST (a, c) and precipitation (b, d) is displayed in the top right corner of each panel. The green box in (a, c) highlights the tropical Pacific and Atlantic regions where SST data are used in the SVD analysis.

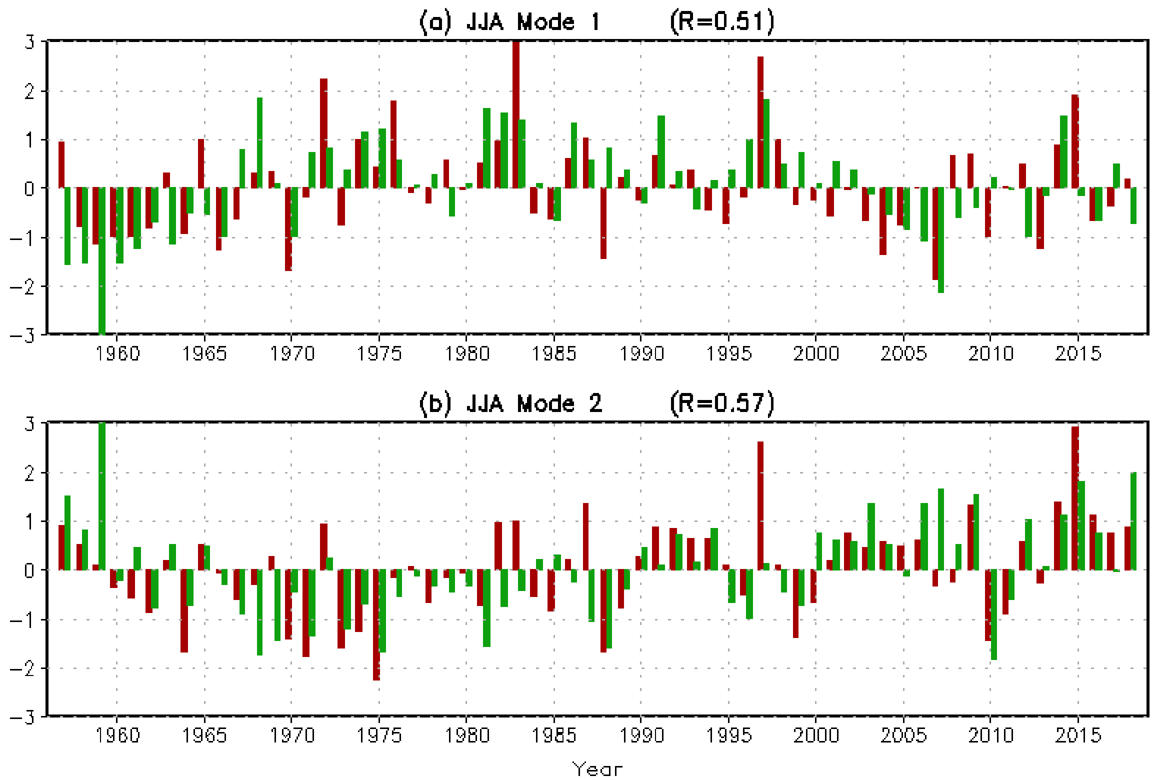

Figure 5.7 Normalized SVD time series of summer (JJA) SST (red bars) and precipitation (green bars) for (a) the first and (b) second modes from the 18-member ensemble mean data of the 1957–2018 AMIP simulations. The correlation (R) between each pair of SVD time series is displayed at the top of each panel.

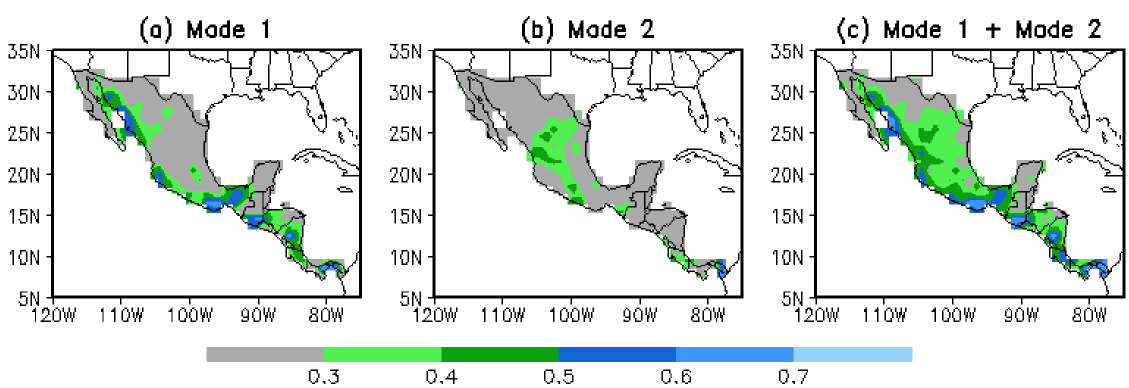

Figure 5.8 Anomaly correlation between observed 1948–2024 JJA precipitation and reconstructed precipitation anomalies based on (a) SVD mode 1 SST time series, (b) SVD mode 2 SST time series, and (c) both mode 1 and mode 2 SST time series. Color shadings denote the correlations greater than 0.3, which are above the 99% significance level.

Chapter 6: Characterizing Mid-Summer Drought in the Context of Seasonal Cycle

6.1 Introduction

The mid-summer drought (MSD) is a prominent climatic phenomenon over Central America and Mexico (CAM), characterized by a temporary reduction in rainfall during the middle of the rainy season, typically between July and August (Magaña et al. 1999). This rainfall reduction interrupts what is normally the peak of the wet season, creating a distinct bimodal precipitation pattern (García-Oliva and Pazos 2021). The MSD has significant consequences for agriculture, water resources, and ecosystems across the region (Curtis and Gamble 2008; Hidalgo et al. 2013; Maurer et al. 2022). Understanding its variability and drivers is crucial for improving climate adaptation strategies and optimizing resource management, particularly as the region faces increasing climate variability.

The seasonal evolution of the MSD exhibits considerable spatial and temporal variability, influenced by a complex interplay of local and large-scale atmospheric and oceanic conditions. Previous studies have linked the MSD to the seasonal migration of the Intertropical Convergence Zone (ITCZ; Small et al. 2007), variations in the strength and positioning of the North Atlantic Subtropical High (NASH; Gamble et al. 2008), and the thermal conditions of the surrounding oceans, particularly sea surface temperatures (SSTs) in the tropical Pacific and Atlantic (Magaña et al. 1999). These factors modulate the intensity and timing of the MSD, as well as its variability across different regions.

One of the primary drivers of MSD interannual variability is the El Niño-Southern Oscillation (ENSO), which affects local atmospheric circulation and SSTs in the tropical Pacific and Atlantic (Curtis 2002). El Niño and La Niña events can significantly alter precipitation patterns in CAM, influencing the onset, intensity, and duration of the MSD (Zhao et al. 2023). In addition to interannual variability, long-term trends related to climate change may be affecting the MSD's characteristics, yet these changes remain insufficiently understood.

Despite the importance of the MSD for regional climate and its economic and social impacts, many questions about its underlying mechanisms and predictability remain. Most notably, how the MSD evolves over the course of the rainy season and how its variations are linked to oceanic and atmospheric patterns have not been fully explored. Improved knowledge of these processes could provide valuable insights for mitigating the impacts of the MSD on agriculture, water resources, and disaster risk management and enhance seasonal forecasting capabilities.

The present study seeks to address these gaps by investigating the seasonal evolution of the MSD over CAM. Specifically, this research aims to: (a) describe the spatial and temporal characteristics of the MSD as part of the seasonal precipitation cycle, and (b) analyze the interannual variations of the MSD in relation to ENSO, as well as any long-term trends.

To achieve these goals, the study will employ empirical orthogonal function (EOF) analysis of total rainfall after removing the annual mean value. This method preserves the seasonal cycle of precipitation, allowing the MSD to be represented by the first two leading EOF modes. This approach simplifies the analysis, and studying the principal components (PCs) of these leading modes can reveal key characteristics of the MSD.

6.2 Data and Methods

The precipitation data used were sourced from the National Oceanic and Atmospheric Administration (NOAA) Climate Prediction Center (CPC) Global Unified Gauge-based Analysis of Daily Precipitation dataset (Chen et al. 2008), available on a $0.5^o \times 0.5^o$ (latitude × longitude) grid. The dataset spans a 42-year period from January 1, 1982, to December 31, 2023.

To examine both the spatial and temporal variations of the precipitation seasonal cycle, as well as the mid-summer drought over CAM, an empirical orthogonal function (EOF; Lorenz 1956) analysis was applied to precipitation over land within the domain 6^{o}N to 18^{o}N and 80^{o}W to 105^{o}W (box in Figure 6.1a). This analysis was based on rainfall variance metrics. Before the EOF analysis, daily precipitation data were smoothed using a 7-day moving average to eliminate high-frequency fluctuations while preserving the mid-summer drought. The EOF analysis was conducted on total rainfall with the climatological annual mean removed. As we will demonstrate, the two leading EOF modes effectively capture the key features of the seasonal cycle, including the reduced precipitation during July and August, which is characteristic of the MSD.

6.3 Seasonal Cycle CAM Precipitation and the Mid-Summer Drought

The climatological annual mean precipitation over CAM, shown in Figure 6.1a, highlights abundant rainfall in the southern region, with local maxima exceeding 5 mm day^{-1} around 6^{o}N and between 12^{o}N and 18^{o}N. In northern Mexico, precipitation is below 3 mm day^{-1} and generally decreases with latitude.

Figure 6.1b presents the annual cycle of the 7-day running mean climatological daily precipitation averaged south of 18^{o}N (solid line) and north of 18^{o}N (dashed line) from January 1 to December 31. The annual cycle of precipitation in southern CAM (solid line) shows a dry season (less than 2 mm day^{-1}) from December to May and a wet season (above 4 mm day^{-1}) from mid-May to early November. Additionally, the wet season has two peaks in June and September, with precipitation around or above 7 mm day^{-1}. Between the two peaks, there is an MSD with relatively dry conditions and minimum precipitation below 5 mm day^{-1} in July.

North of 18^{o}N, the area-average precipitation (Figure 6.1b, dash line) also shows wet and dry seasons, though their contrast is less pronounced. Summer peak precipitation reaches about 4.5 mm day^{-1}, considerably lower than the two peaks south of 18^{o}N.The relatively wet period, with precipitation above 2 mm day^{-1}, lasts from June to mid-October, which is about 1/3 of a year. During summer, the evolution of climatological mean precipitation is smooth and there is no MSD in northern Mexico.

Both the spatial pattern and temporal evolution of the precipitation seasonal cycle, as well as the MSD, are further quantified by the EOF analysis of 7-day running mean daily precipitation from January 1, 1982, to December 31, 2023, with the climatological annual mean removed. Figure 6.2 shows the spatial patterns of two leading EOF modes in the forms of correlation maps (top panels) and regression maps (bottom panels) of precipitation against the two PC time series, respectively. The correlation maps indicate how strong local precipitation is associated with each EOF mode, whereas the regression maps indicate the amount of precipitation related to the variation of each mode.

The spatial pattern of first EOF mode displays a monopole distribution with positive correlations across the CAM (Figure 6.2a), except Baja California. The highest correlations (> 0.6) are found in southern CAM. In contrast, the second mode is characterized by a dipole structure, with negative correlations south of 15^{o}N and positive correlations between 15^{o}N and 25^{o}N (Figure 6.2b). The largest negative correlations are along the east coast, while the largest positive correlations are along the west coast.

Associated with the one-standard-deviation increase in the PC1 time series, there is increase in precipitation up to 6 mm day^{-1} near the west coast around 15^{o}N (Figure 6.2c). In southern CAM, the amount of increase in precipitation ranges from 1 to 4 mm day^{-1}. In central and northern Mexico, the increase in precipitation is up to 3 mm day^{-1}, except for Baja California, where precipitation slightly decreases. For mode 2, one-standard-deviation increase in the PC2 time series leads to decrease in precipitation east of 90^{o}W and south of 20^{o}N (Figure 6.2d). The rainfall reduction can be as much as 3 mm day^{-1} along the east coast. Rest of CAM, precipitation increases with the largest amount of 3 mm day^{-1} in the west coast around 15^{o}N. Overall, the changes in precipitation associated with EOF2 are comparable to those with EOF1, and thus may modulate the EOF1 rainfall pattern when combining the two modes together.

The temporal evolution of the spatial patterns of the two leading EOF modes is described by their corresponding PC time series. To highlight the *climatological* seasonal cycle, the normalized daily PC time series are averaged over the 42 years (1982–2023) and are shown in Figure 6.3 from January 1 to December 31 for the two modes. The time series of PC1 (red line) exhibits a seasonal cycle with negative values (dry season) from November to May and positive values (wet season) from May to November. During summer, PC1 is characterized by two peaks in June and September and one pit in July, corresponding to the MSD. The temporal variation of PC1 is almost identical to the time series of climatological daily precipitation averaged over the southern CAM shown in Figure 6.1b (solid line). The first EOF mode accounts for 40% of daily precipitation variance with respect to the climatological annual mean, and well captures the seasonal cycle of precipitation over southern CAM, as well as the MSD.

The mean PC2 time series (blue line) is dominated by positive values from January to September, except for May, and negative values from October to January. Like PC1, during summer and early fall, PC2 also exhibits two peaks in June/July and August/September and one pit in July. This suggests that the second EOF mode can enhance the precipitation associated with mode 1 between 15^{o}N and 30^{o}N but lower the precipitation further south (Figure 6.2) during the peak rainy season. Therefore, it can modulate the rainfall pattern in the MSD period. The second mode explains 10% of the precipitation variance.

The EOF analysis of 7-day running mean daily precipitation (1982–2023) identifies two leading modes that capture the seasonal cycle and MSD. During the rainy season, the first mode increases precipitation in southern CAM, while the second mode reduces precipitation south of 15°N and enhances it north of 15°N. Both modes exhibit similar seasonal cycles with peaks in June/July and August/September, and a dip in July. Thus, the temporal variations of the two PCs effectively represent the evolution of both the precipitation seasonal cycle and MSD in CAM, simplifying their representation.

6.4 Influence of ENSO on the Intensity and Duration of the Mid-Summer Drought

The impact of ENSO on the MSD is assessed by compositing the PC time series of the two leading EOFs for different ENSO phases. Over the 42-year period (1982–2023), there were nine El Niño, nine La Niña, and 24 ENSO-neutral events during the summer season, based on JJA ONI values with thresholds of ±0.5ºC (CPC 2025). Figure 6.4 shows the composite PC time series for each ENSO category, along with the 42-year mean PC time series (black curve), which was previously displayed in Figure 6.3.

For the first EOF mode (Figure 6.4a), the ENSO-neutral composite (orange curve) closely follows the climatology (black curve) during the warm season (May–October). The El Niño composite (red curve) shows significant decreases in the PC1 value, particularly in August and September. These results suggest that El Niño enhances the MSD in July and August, reduces rainfall during the two peak periods of the rainy season, and extends the duration of the MSD. Its impact is greater in late summer than in early summer. Conversely, the La Niña composite exhibits nearly opposite effects, with increases in precipitation during both peak rainy seasons and the MSD period, thereby reducing the intensity of the MSD and shortening its duration.

For the second EOF mode (Figure 6.4b), the composites for different ENSO phases show high-frequency fluctuations, with less coherent patterns during the summer months. Significant composite signals at the 95% confidence level are observed for La Niña events from May to August (blue curve), with decreasing PC2 values. In the fall, El Niño tends to increase the PC2 value, while La Niña tends to decrease it, relative to the PC2 climatology. Overall, ENSO exerts a stronger influence on the first mode than on the second.

6.5 Long-Term Changes in the Seasonal Cycle of CAM Precipitation and the MSD

The long-term changes in the seasonal cycle of precipitation across CAM and the MSD from 1982 to 2023 are examined over three 14-year segments: 1982–1995, 1996–2009, and 2010–2023. Figure 6.5 presents the daily PC time series averaged over these three periods for both EOF modes.

For the first EOF mode (Figure 6.5a), the mean PC1 values in the early years (blue lines, 1982–1995) are lower from May to December compared to the 42-year climatology (black curve), particularly during the second rainy peak in September. The summer wet season is shorter, precipitation is reduced, and the MSD is drier and lasts longer. In the second 14-year period (orange curve, 1996–2009), the PC1 time series aligns more closely with the 42-year climatology, showing higher PC values in September and October, indicating increased precipitation during the second rainy season peak. In the final 14 years (red curve, 2010–2023), the mean PC1 values exceed the 42-year climatology from May to November, reflecting a consistent increase in precipitation throughout the rainy season, including during the MSD period. This also corresponds with a shortening of the MSD.

For the second EOF mode (Figure 6.5b), long-term changes are also observed across the 12 months of the year. The early years (blue curve, 1982–1995) exhibit higher PC values, which decrease over time, with the lowest values in the last 14 years (red curve, 2010–2023). This decrease is most pronounced in July, the first peak before the MSD, and smaller in September, the second peak after the MSD. These changes modulate the seasonal cycle of precipitation and the MSD across southern CAM (Figures 6.2b, d).

Over the past four decades, both PC values have fluctuated considerably from decade to decade, highlighting significant long-term changes in the seasonal cycle of CAM precipitation, as well as shifts in the intensity and duration of the MSD. The SSTs in both the tropical Pacific and Atlantic, as discussed in Chapters 4 and 5, along with CAM land surface air temperatures (not shown), have experienced consistent warming over this period. A recent study by Stewart et al. (2022) observed a general warming trend across CAM over the past 40 years, with a warming rate of 0.2–0.8°C per decade. Further investigation is needed to explore how the long-term changes in MSD documented in this dissertation might be related to this observed warming trend.

6.6 Summary

This chapter investigates the seasonal cycle of precipitation and the MSD over CAM from 1982 to 2023. The climatological analysis reveals distinct wet and dry seasons in CAM, with a dry period from December to May and a wet season from mid-May to early November. The wet season features two precipitation peaks in June and September, separated by the MSD in July, marked by a significant reduction in rainfall. The EOF analysis of 7-day running mean daily precipitation identifies two leading modes that capture the seasonal cycle and MSD. The first mode is characterized by increased precipitation in southern CAM and the second mode by a dipole structure that affects precipitation patterns north and south of 15°N. These two modes exhibit similar seasonal cycles with peaks in June/July and August/September and a dip in July, aligning with the MSD.

The impact of ENSO on the MSD is also examined, showing that El Niño events enhance the MSD by reducing rainfall and extending its duration, while La Niña events generally increase rainfall and shorten the MSD. The study further explores long-term changes in precipitation across three 14-year periods (1982–1995, 1996–2009, 2010–2023), highlighting an increase in precipitation and a shortening of the MSD in recent years. This shift suggests a significant change in the seasonal cycle and MSD intensity over the past four decades. The potential relationship between these long-term changes in precipitation patterns and regional warming requires further investigation.

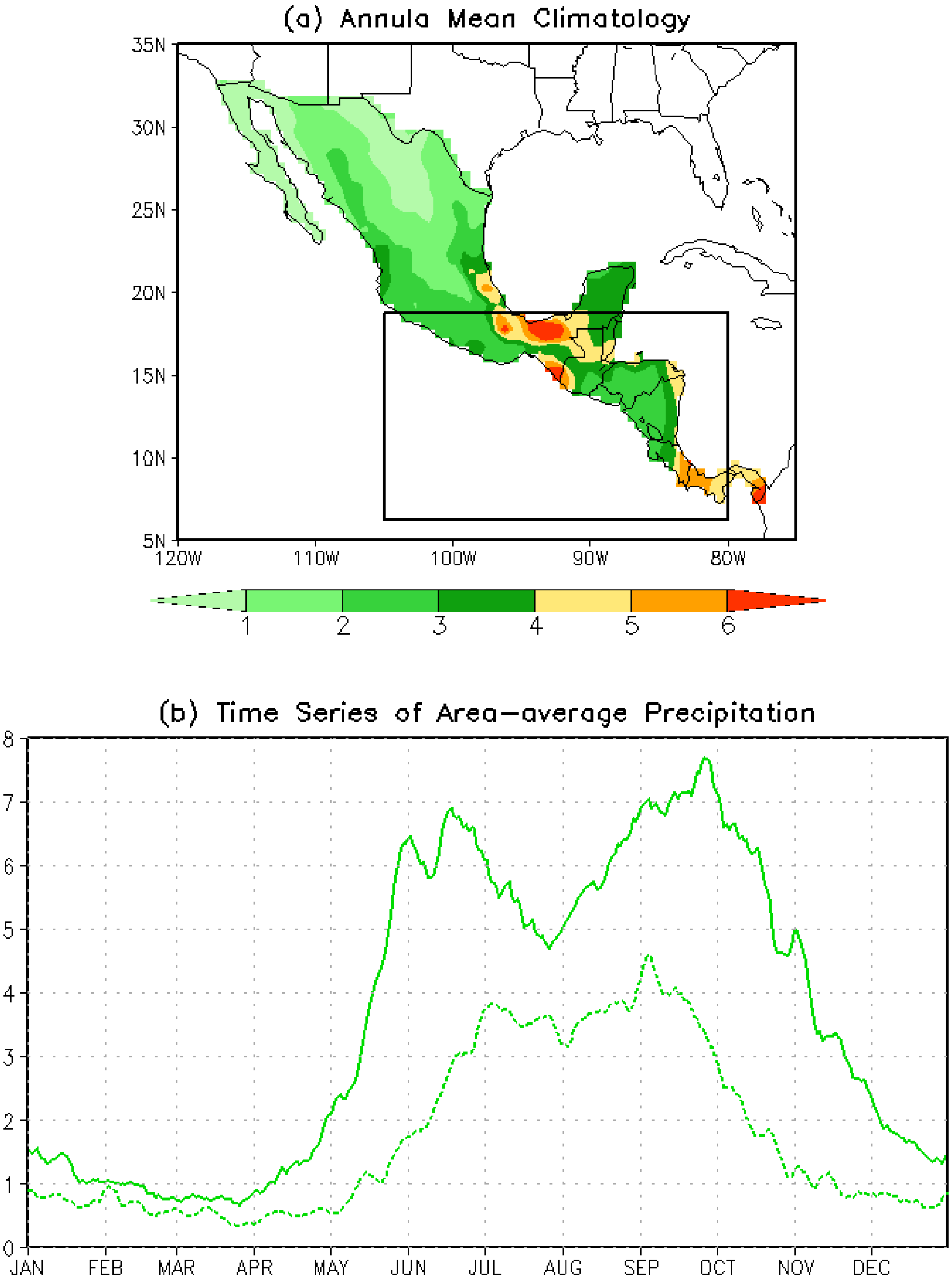

Figure 6.1 (a) Climatological annual mean precipitation (mm day^{-1}) in Central America and Mexico and (b) time series of 7-day running mean climatological daily precipitation (mm day^{-1}) area-averaged in the box (solid green) shown in (a) and that area-averaged north of 18ºN (dash green) based on 42-year (1982–2023) observational data.

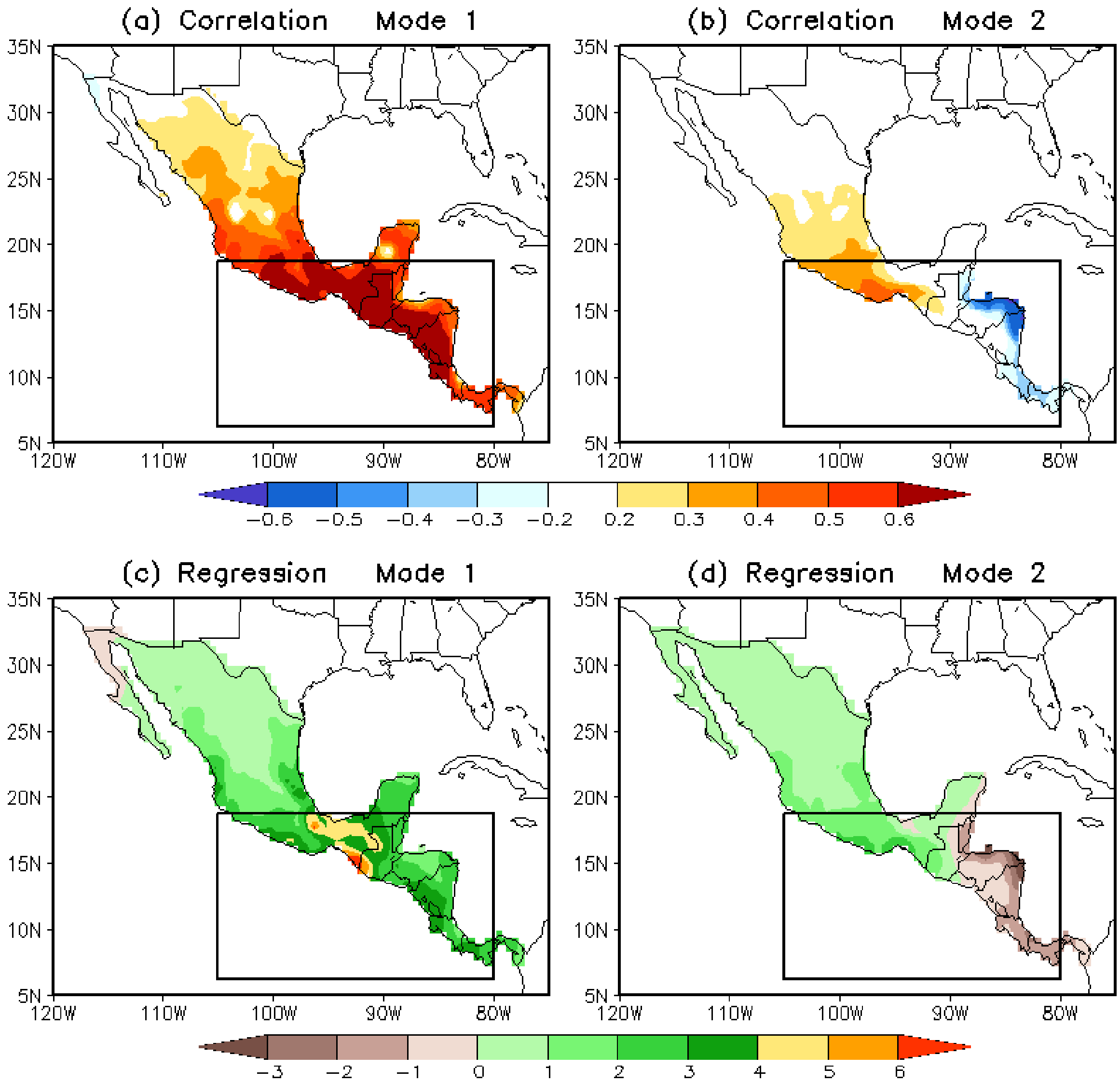

Figure 6.2 Spatial patterns of the two leading EOFs of precipitation over southern CAM in the form of correlation map for (a) mode 1 and (b) mode 2, and in the form of regression map (units: mm day^{-1}) for (c) mode 1 and (d) mode 2, respectively. Precipitation over land inside the box was used for the EOF analysis.

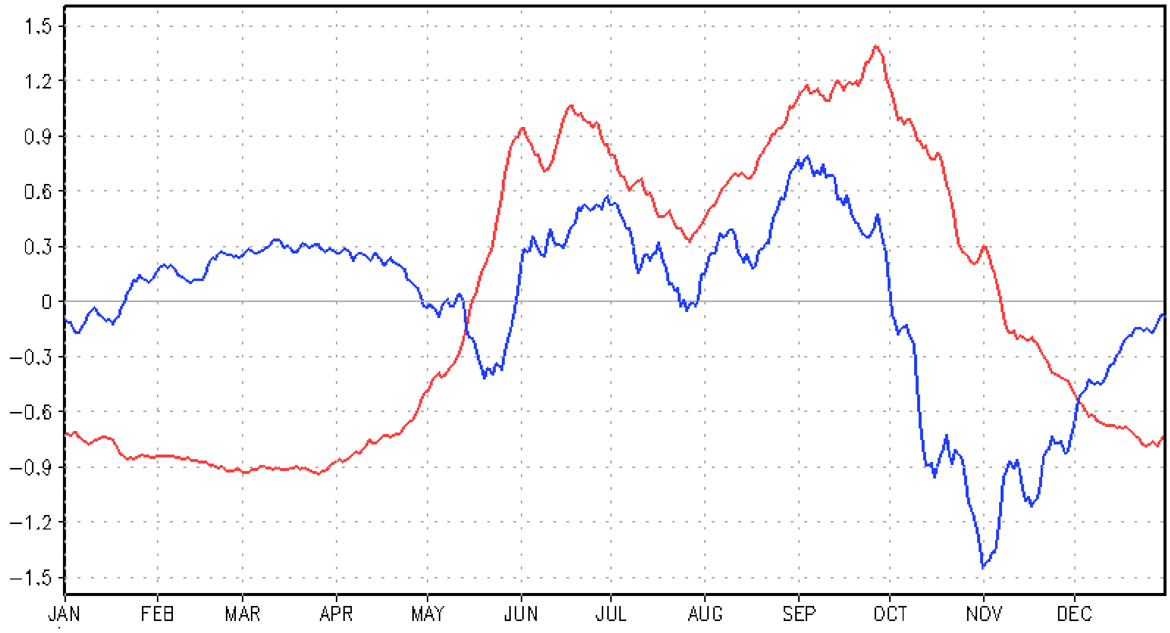

Figure 6.3 42-year (1982–2023) average of normalized daily PC time series from January 1 to December 31 for the first (red) and second (blue) EOF modes of southern CAM precipitation.

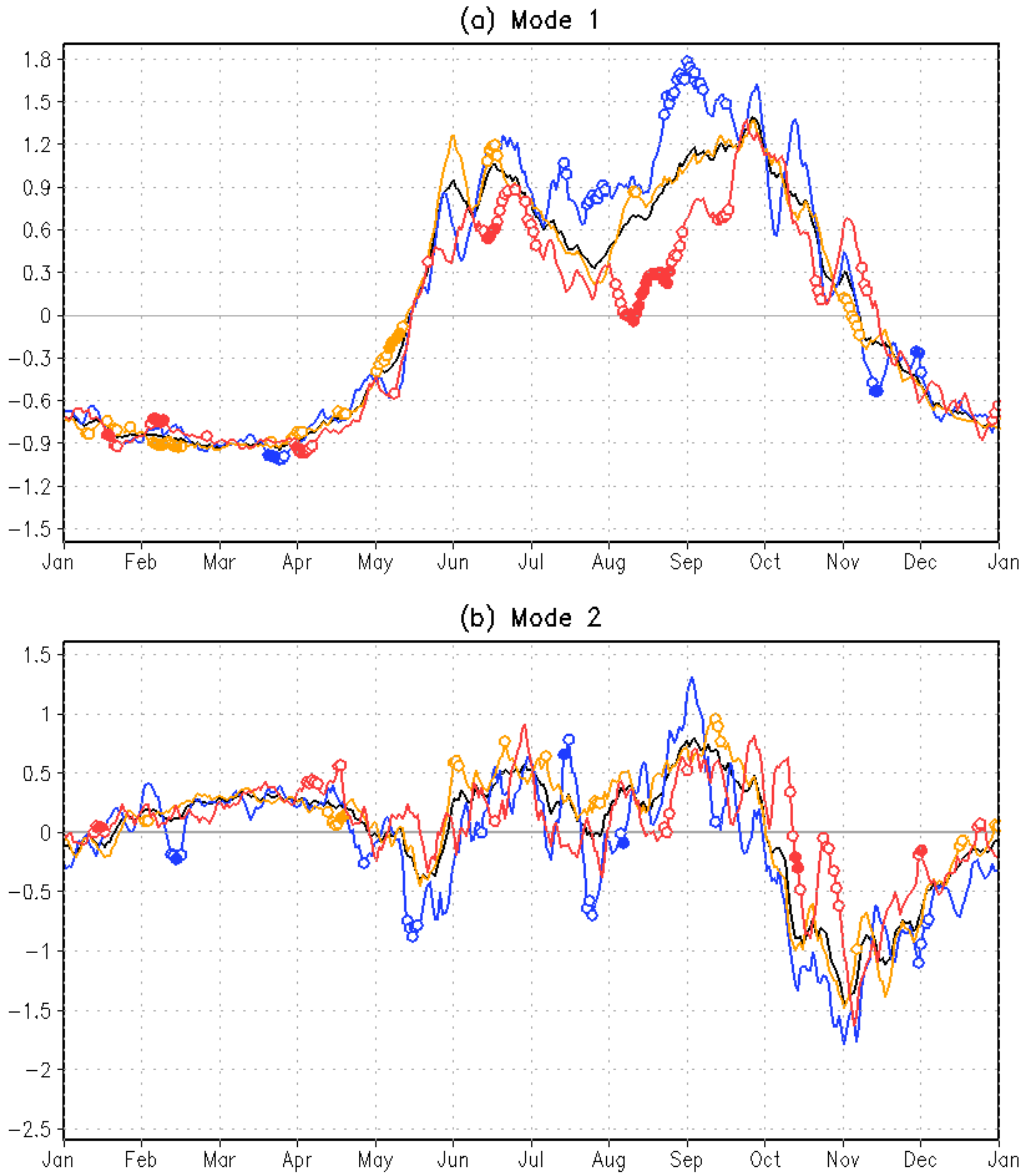

Figure 6.4 Composites of normalized daily PC time series from January 1 to December 31 for (a) mode 1 and (b) mode 2, based on nine El Niño years (red), nine La Niña years (blue), and 24 ENSO-neutral years (orange) during the 42-year period (1982–2023). The black curves represent the 42-year mean PC time series, as shown in Figure 6.3. Open and closed circles indicate composite values significantly different from the climatology (black) at the 95% and 99% confidence levels, respectively, as determined by the Monte Carlo tests. To apply the Moving Block Bootstrap method for the Monte Carlo test, the 42 years of data are divided into 7 blocks, each containing 6 consecutive years.

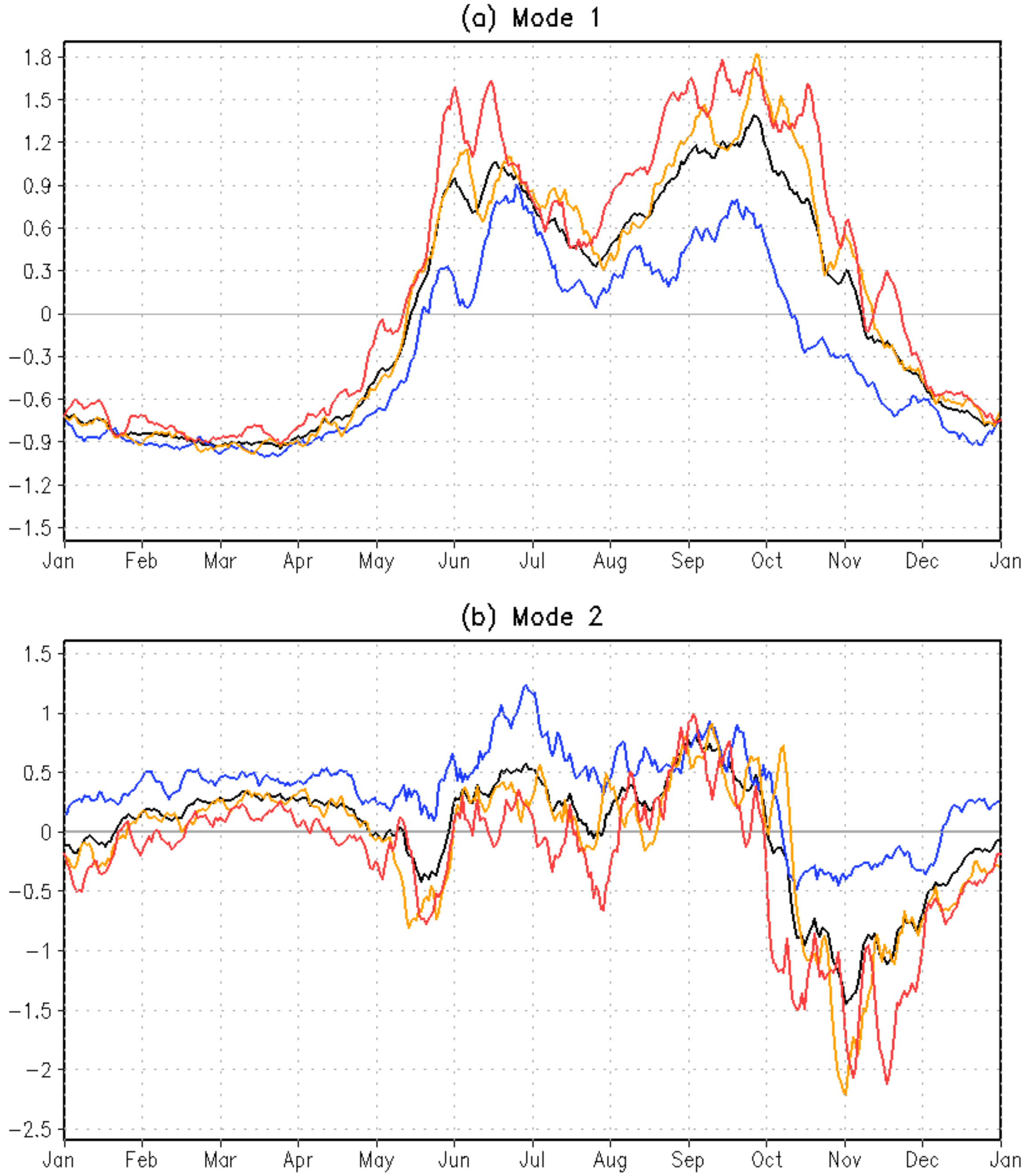

Figure 6.5 14-year average of the normalized daily PC time series over 1982–1995 (blue), 1996–2009 (orange), and 2010–2023 (red), respectively, for (a) mode 1 and (b) mode 2, from January 1 to December 31. The black curves represent the 42-year mean PC time series, as shown in Figure 6.3.

Chapter 7: Regional Hydrological Cycle: Present-day Climate vs. Future Warmer Climate

The observational analyses in Chapters 4 and 5 demonstrate that the tropical SST warming trend is linked to CAM rainfall deficits in both winter and summer. As global warming continues, understanding how CAM precipitation will change is critical for regional climate adaptation and resilience. The hydrological cycle in CAM is a key component of the region's climate system, significantly influencing precipitation patterns. Assessing this regional hydrological cycle is essential for anticipating future changes in precipitation, particularly under the influence of a warmer climate.

This chapter focuses on the analysis of simulations from CMIP5 (Taylor et al. 2012) and CMIP6 (Eyring et al. 2016), with a primary emphasis on two key time periods: the present-day climate (1980–2005, based on historical experiments) and future climate projections (2071–2098) under an intermediate greenhouse gas emissions scenario (RCP4.5 in CMIP5 and SSP2-4.5 in CMIP6). By examining both historical and future climate data, this chapter aims to explore how projected changes in precipitation, temperature, and other climatic variables may affect the regional hydrological cycle in CAM. These changes are expected to have significant implications for water availability, agriculture, and overall climate resilience in the region.

7.1 Precipitation in CAM Under Present-Day Climate

The ability of CMIP models to simulate the climatological seasonal mean precipitation in CAM is assessed first. Figure 7.1 shows the long-term mean (1980–2005) climatology of seasonal precipitation for both winter (DJF) and summer (JJA) derived from observational data (CRU), along with the multi-model ensemble (MME) means of CMIP5 and CMIP6. Compared to the observational precipitation climatology (Figures 7.1a, b), both CMIP5 (Figures 7.1c, d) and CMIP6 (Figures 7.1e, f) present-day climate simulations reasonably reproduce the observed winter and summer precipitation patterns in CAM. This provides confidence in using the same CMIP5 and CMIP6 model sets to project future rainfall changes in the CAM region.

7.2 Projected Climate Warming by the End of the 21st Century

Next, we examine the projected warming of the climate by the end of the 21st century, as forecasted by CMIP models. Figure 7.2 displays the climatology of winter and summer seasonal mean sea surface temperatures (SSTs) averaged over 1980–2005 and 2071–2098, based on the CMIP5 historical simulations and climate projections, respectively. It also shows the differences between these two climatologies. The historical simulations accurately capture both the western Pacific warm pool and the eastern Pacific cold tongue (Figures 7.2a, b). By the end of the 21st century, projected climatological SSTs could reach as high as 30°C in both the western Pacific warm pool and the Atlantic warm pool (Figures 7.2c, d). The differences in SST climatologies between these two periods indicate a projected warming of 1–2°C in tropical SSTs during both winter and summer (Figures 7.2e, f).

Projected warming over CAM land areas is expected to be stronger than the SST warming. Figure 7.3 presents the mean surface air temperature difference between the 2071–2098 and 1980–2005 periods for both winter (top panels) and summer (bottom panels), based on the CMIP5 (left panels) and CMIP6 (right panels) MME mean data. By the end of the 21st century (2071–2098), both CMIP5 and CMIP6 project a 1.5–3°C increase in surface air temperature over CAM during both winter and summer. Temperature increases are generally larger in summer than in winter and are more pronounced in northern Mexico compared to Central America. It is also notable that the projected temperature changes for CAM under CMIP6 are approximately 0.5°C higher than those projected by CMIP5.

Figure 7.4 shows CAM domain-averaged land surface air temperature anomalies from 1865 to 2095, relative to the 1980–2005 climatology and 10-year low-pass filtered, for both observations and simulations/projections from the CMIP5 and CMIP6 ensembles. The CAM regional temperature anomalies in the CMIP5 and CMIP6 historical simulations are comparable to observations in terms of long-term variations and amplitude. Progressive regional warming began around the 1960s in both winter and summer in the CMIP simulations. By the end of the 21st century, CMIP5 projects a 2°C warming above the 1980–2005 mean over CAM in winter (Figure 7.4a) and 2.5°C warming in summer (Figure 7.4c). In contrast, CMIP6 projects about 2.5°C warming in winter (Figure 7.4b) and 3°C warming in summer (Figure 7.4d). These results are consistent with those in Figure 7.3, but provide a longer-term context for the projected warming.

Given this projected warming, the next section will assess how precipitation patterns and the associated hydrological cycle over CAM might change, based on the future climate projections from the CMIP5 (RCP4.5) and CMIP6 (SSP2-4.5) scenarios.

7.3 Projected Changes in Regional Hydrological Cycle

The hydrological cycle includes key variables such as precipitation (P), evaporation (E), freshwater flux (P–E), soil moisture, and runoff (e.g., Mariotti et al., 2015). Projected regional changes in these variables by the end of the 21st century are assessed by comparing the mean differences between the 2071–2098 and 1980–2005 periods for both winter and summer, based on the CMIP5 and CMIP6 MME means for CAM. Additionally, the CAM domain-averaged anomaly time series from 1865 to 2095 are analyzed.

7.3.1 Precipitation

The spatial maps of the projected mean precipitation changes for 2071–2098 relative to 1980–2005 are shown in Figure 7.5. Distinct seasonal differences are observed. In winter (Figures 7a, b), the mean precipitation changes show drier conditions in central and northern Mexico, with large negative anomalies in the west (-0.3 to -0.6 mm day^{-1}) and smaller negative anomalies in the east (-0.1 to -0.2 mm day^{-1}). In Central America, CMIP6 (Figure 7.5b) indicates drier conditions (-0.1 to -0.4 mm day^{-1}) along the east coast, while CMIP5 (Figure 7.5a) shows no significant rainfall anomalies (-0.2 to 0.2 mm day^{-1}). In summer (Figures 7.5c, d), the largest decrease in precipitation (exceeding -0.5 mm day^{-1}) occurs in central and southern CAM, with no significant changes in CMIP5 and positive precipitation anomalies in CMIP6 over northern Mexico. The precipitation decrease is more pronounced in CMIP6 than in CMIP5. It is interesting to note the projected summer precipitation decrease (Figures 7.5c, d) collocates with the rainfall decrease associated with the SST warming trend seen in the SVD analysis (Figure 5.1b).

The time series of precipitation anomalies averaged over the CAM land region, relative to the 1980–2005 climatology, are shown in Figure 7.6. Both winter and summer precipitation anomalies display progressive drying trends over the 1865–2095 period. The downward trend is more pronounced in summer (Figures 7.6c, d) than in winter (Figures 7.6a, b), with the strongest trend observed in the CMIP6 simulations for summer (Figure 7.6d). Additionally, the uncertainty in precipitation changes (as indicated by inter-member spreads) is larger in CMIP5 models than in CMIP6 models in both seasons. No significant trend is observed in the observational CRU precipitation data.

7.3.2 Evaporation

The spatial maps of the projected mean evaporation changes for 2071–2100 relative to 1980–2005 are shown in Figure 7.7. As air temperature increases (Figure 7.3), the atmosphere's capacity to hold water vapor also rises. Evaporation over the tropical Pacific and Atlantic Oceans is projected to increase (not shown). Over land, evapotranspiration (ET) exhibits mixed changes. In the northern coastal regions during winter, ET increases in both CMIP5 and CMIP6 models (Figures 7.7a, b). Even though precipitation is projected to decrease in these regions (Figure 7.5a, b), coastal soils may still retain moisture for a time, and as this moisture is gradually used by plants, the ET rate remains elevated.

In summer, ET increases in southern Central America but decreases in northern Central America. Although precipitation is projected to decrease in Central America during summer (Figures 7.5c, d), the changes in ET are influenced not only by local precipitation but also by temperature, winds, and geographic factors. Southern Central America experiences rising temperatures (Figures 7.3c, d) and higher solar radiation during summer, both of which increase the potential for ET. Even with reduced precipitation, higher temperatures lead to more evaporation from the soil and vegetation. Additionally, stronger winds at low latitudes can enhance the evaporation process by removing moisture from the surface more quickly.

The decrease in ET over northern Central America is associated with reduced precipitation (Figure 7.5c, d), which lowers the soil moisture available for ET. This decrease is more pronounced in CMIP5 than in CMIP6. Overall, the projected spatial patterns of ET changes are consistent between CMIP5 and CMIP6 in both winter and summer.

Figure 7.8 shows the time series of ET anomalies averaged over CAM for the winter and summer seasons. By the end of the 21st century, ET slightly increases during winter in both CMIP5 and CMIP6 (Figures 7.8a, b), and also increases during summer in CMIP6 (Figure 7.8d). However, ET slightly decreases in CMIP5 (Figure 7.8c), likely due to the large negative ET anomalies in northern Central America (Figure 7.7c). Overall, the observational data (black lines) vary within the range of the CMIP model member spreads.

7.3.3 Freshwater Flux

The difference between precipitation (P) and evaporation (E), denoted as P–E, determines the surface downward freshwater flux. This difference has significant implications for water-sensitive systems and can pose considerable economic, ecological, and societal risks. For example, over land, P–E influences the water available for irrigation and other uses. Over the ocean, changes in P–E affect sea surface freshwater loss, which can lead to changes in salinity and potentially alter the thermohaline circulation. Therefore, the projected change in P–E serves as a critical indicator of future climate change.

Figure 7.9 shows the spatial maps of the projected mean P–E changes for 2071–2098 relative to 1980–2005 for both winter and summer. In winter (Figures 7.9a, b), the projected P–E decreases across central and northern Mexico, with values exceeding -5 mm day^{-1} in the west and -2 to -3 mm day^{-1} in the east. This decrease is primarily driven by reduced precipitation (Figures 7.5a, b). In contrast, the decrease in P–E during summer mainly occurs in Central America and southern Mexico, which aligns with the shift in rainfall change patterns from winter to summer (Figure 7.5). The decrease in P–E is similar in both CMIP5 and CMIP6 during winter, but the decrease is larger in CMIP6 than in CMIP5 during summer. Additionally, both CMIP5 and CMIP6 project an area near the Texas border with an increase in P–E during summer (Figures 7.9c, d).

Figure 7.10 shows the time series of P–E anomalies averaged over CAM for both winter and summer. In winter (Figures 7.10a, b), both the CMIP5 and CMIP6 MME averages show a downward trend in freshwater flux starting around the 1980s. However, in summer (Figures 7.10c, d), the downward trend is observed throughout the entire period (1865–2095), with a much stronger trend in CMIP6 compared to CMIP5. The black lines in Figure 7.10 represent the P–E changes estimated from observed P and E data over CAM. These fluctuations exhibit similar amplitudes to those seen in individual CMIP ensemble members.

7.3.4 Soil Moisture and Runoff

Figure 7.11 shows the spatial maps of the mean near-surface relative soil moisture changes for 2071–2098 compared to 1980–2005 for winter and summer. Relative change in soil moisture is used because land models in different CMIP models have varying vertical resolutions. As a result, soil moisture data from different models are measured at different depths and have different magnitudes. To account for this, the MME average is applied to the relative mean changes, which are calculated as the mean changes divided by the corresponding reference climatology. By the end of the 21st century, projected near-surface soil moisture decreases in many parts of CAM. The largest decreases occur in the north during winter (Figures 7.11a, b) and in the south during summer (Figure 7.11d), consistent with changes in precipitation (Figure 7.5). However, the projected changes in summer are much smaller in CMIP5 (Figure 7.11c) compared to CMIP6 (Figure 7.11d).

The time series of relative total soil moisture averaged over CAM are shown in Figure 7.12 for winter and summer. There are steady, progressive decreases in the CMIP5 MME mean relative soil moisture (Figures 7.12a, c) from 1865 to 2098. In contrast, the decrease in CMIP6 starts in the 1980s and aligns more closely with the observations (black lines) during the common period. The projected decrease in soil moisture is larger in CMIP5, with much greater uncertainty (-4% ± 6%) compared to CMIP6 (-3% ± 1%).

The corresponding time series of total runoff changes averaged over CAM are shown in Figure 7.13. In general, when soil moisture is low (i.e., during dry conditions), the soil has a greater capacity to absorb incoming rainfall, meaning more of the precipitation infiltrates the soil, resulting in lower surface runoff. As a result, the projected decrease in soil moisture is associated with a decrease in runoff. By the end of the 21st century, the projected runoff decrease is 10% in both winter and summer for CMIP5 (Figures 7.13a, c) and 2% in winter and 20% in summer for CMIP6 (Figures 7.13b, d).

7.4 Summary

This study examines changes in the CAM regional water cycle under a warming climate, based on the MME mean of the CMIP5/CMIP6 historical and RCP4.5/SSP2-4.5 simulations. The results indicate a warmer and drier mean state in CAM by the end of the 21st century compared to the present-day climate, with surface air temperature increases of 1.5–3°C and precipitation decreases of about 0.1–0.5 mm day^{-1}. The combined effects of changes in precipitation (P) and evaporation (E) suggest significant alterations to the water cycle. By 2071–2098, the projected mean surface downward freshwater flux (P–E) is expected to decrease by 0.1–0.6 mm day^{-1} relative to present-day values, alongside a 5% decrease in soil moisture and a 10–20% reduction in runoff.

It is important to note that the projected changes are not homogeneous and exhibit strong seasonality and geographic variation. The most prominent changes occur between winter and summer, as well as between northern and southern CAM. Over land, precipitation is the primary driver of the land surface hydrological cycle. As precipitation changes, other major hydrological elements, such as soil moisture, runoff, and evapotranspiration, also adjust correspondingly. Decreased precipitation leads to reductions in soil moisture and runoff, further lowering evapotranspiration. Conversely, warmer surface temperatures promote higher land evapotranspiration. The combined effects of precipitation and temperature changes ultimately determine the direction of land evapotranspiration changes, as discussed in Section 7.3.2.

Overall, the projected changes in the regional hydrological cycle from CMIP5 and CMIP6 are consistent with each other. Given that the ten hottest years have occurred in the past decade and global warming continues to accelerate, the projected decrease in precipitation over CAM may already be underway, as identified by the SVD analysis in Chapters 4 and 5. Further analysis of observational data and CMIP5/CMIP6 simulations is needed to better understand the physical processes behind the projected hydrological changes in CAM.

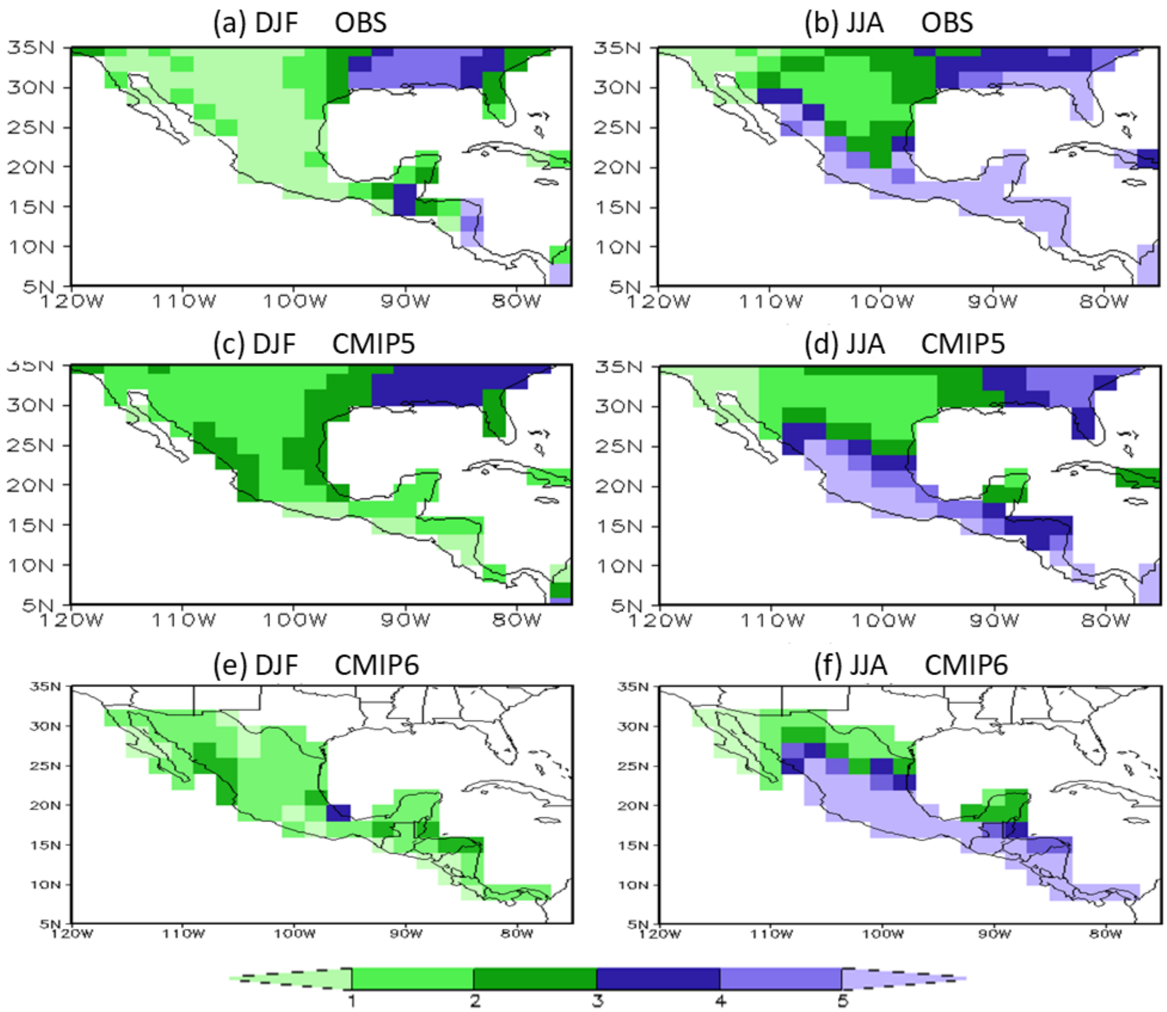

Figure 7.1 Long-term (1980–2005) mean seasonal precipitation (units: mm day^{-1}) for (a, c, e) winter (DJF) and (b, d, f) summer (JJA) derived from (a, b) CRU observations, (c, d) CMIP5, and (e, f) CMIP6. The model precipitation climatology is based on the multi-model ensemble mean, with the modes listed in Tables 2.1 and 2.2 for CMIP5 and CMIP6, respectively.

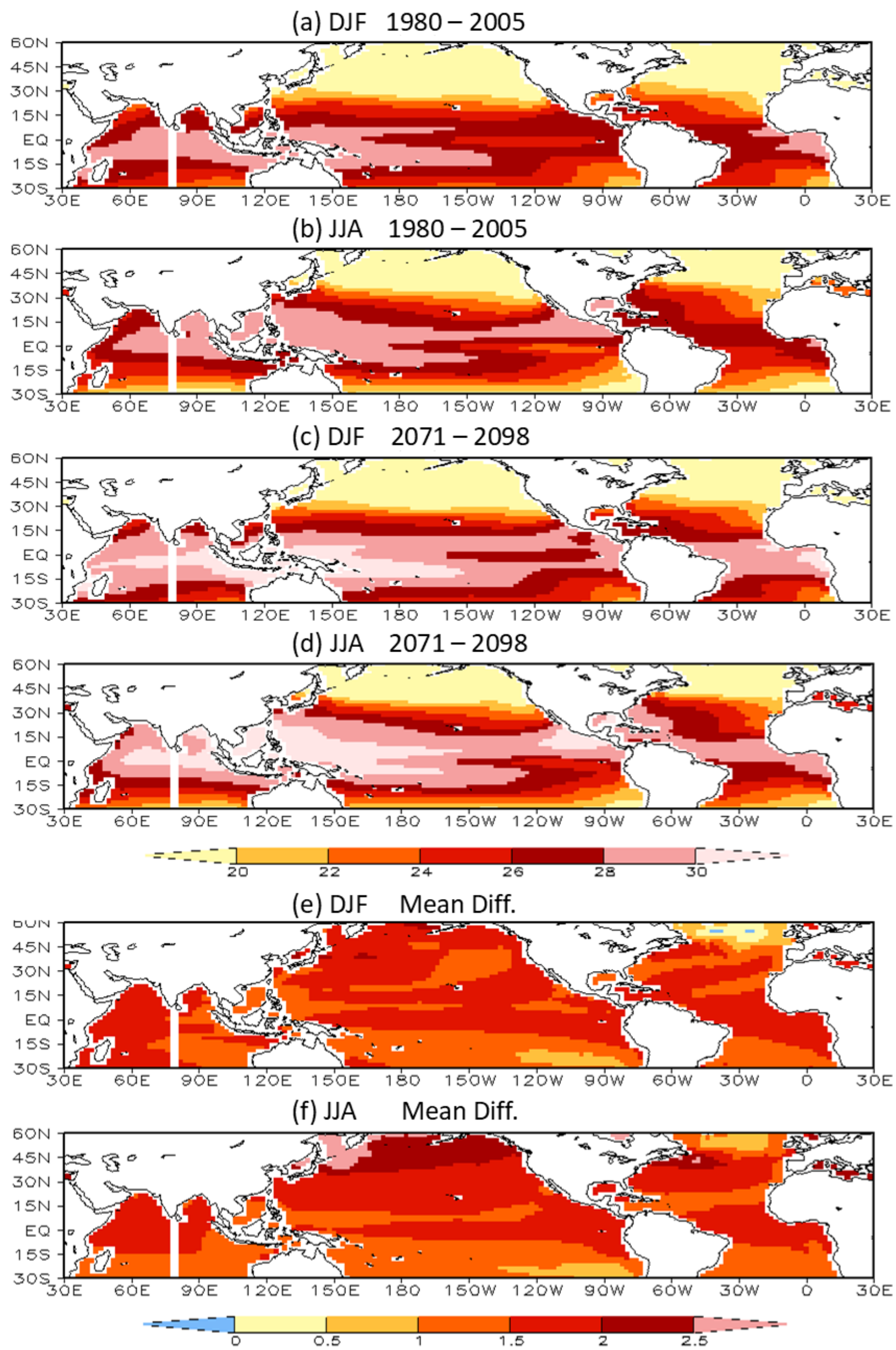

Figure 7.2 Long-term mean seasonal SST (units: °C) for (a, c) winter (DJF) and (b, d) summer (JJA) derived from the CMIP5 historical simulations for (a, b) the present-day climate (1980–2005) and (c, d) future climate projections (2071–2098), and their difference (projected change) for (e) winter and (f) summer.

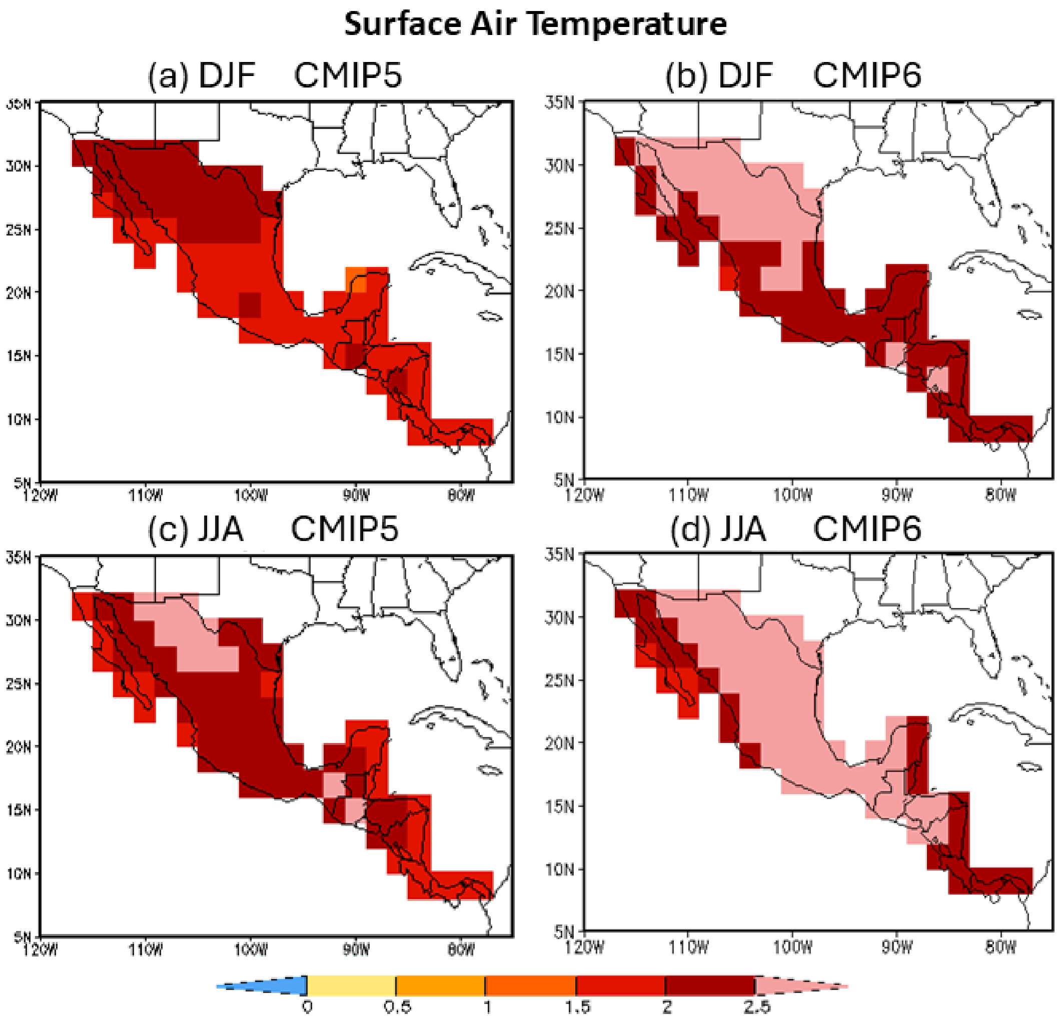

Figure 7.3 Projections of surface air temperature change (units: °C) over the 2071–2098 period relative to the 1980–2005 reference period as depicted by (a, c) the CMIP5 and (b, d) CMIP6 ensemble means. They represent the differences between the mean temperatures averaged over the 2071–2098 and 1980–2005 periods for (a, b) winter and (c, d) summer.

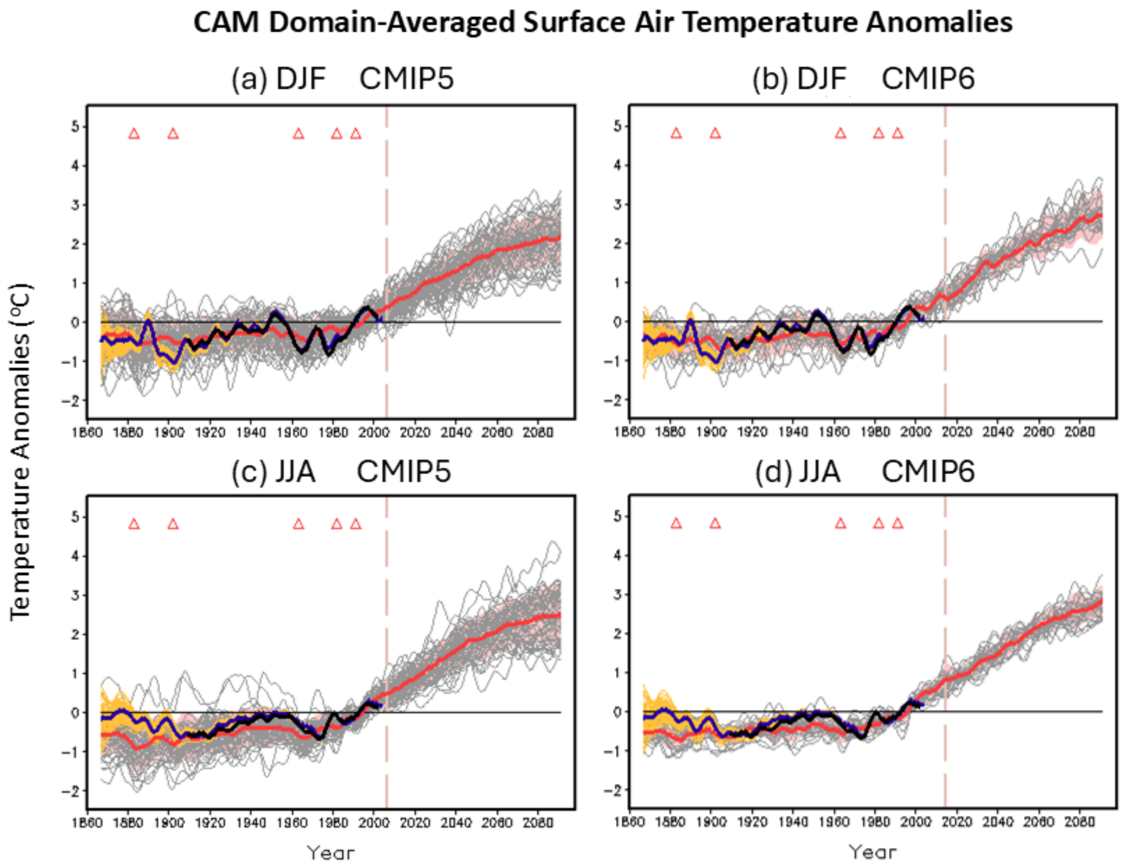

Figure 7.4 CAM domain-averaged surface air temperature anomalies (units: °C) over the period 1865–2095 for (a, b) winter (DJF) and (c, d) summer (JJA), derived from the (a, c) CMIP5 and (b, d) CMIP6 MME means, relative to the1980–2005 climatology. Gray lines represent individual model members (10-year low-pass filtered), while red lines indicate the multi-model means. Vertical dashed lines in 2005 separate historical simulations from projections for CMIP5, and in 2014 for CMIP6. Pink shading represents one standard deviation of inter-member spreads around the MME means. Dark blue and black lines correspond to observed temperature anomaly estimates based on the HadCRUT4 and CRU data, respectively. Yellow lines represent the 100 individual members of the HadCRUT4 observations. Red triangles at the top of each panel indicate the years of major tropical volcanic eruptions (Driscoll et al. 2012).

Precipitation

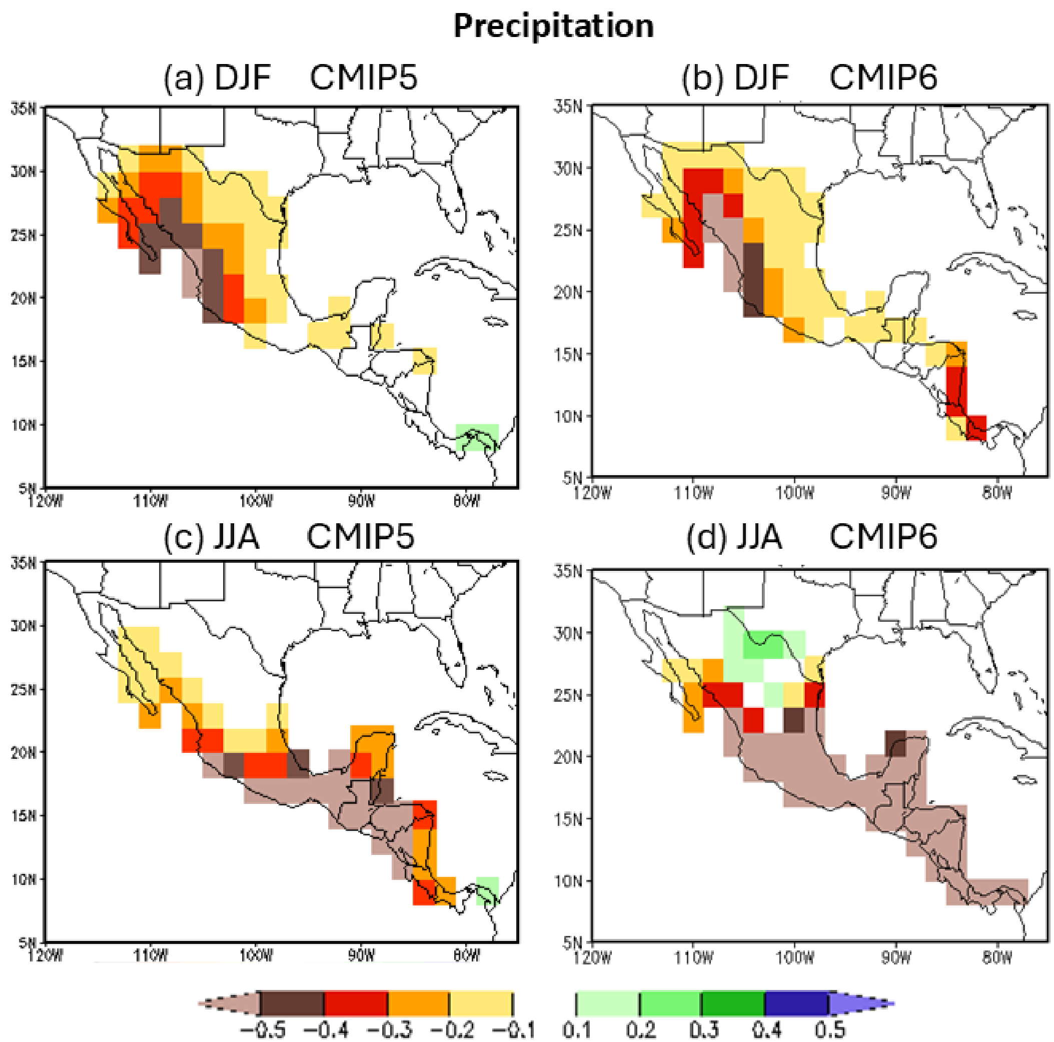

Figure 7.5 Projections of precipitation change (units: mm day^{-1}) over the 2071–2098 period relative to the 1980–2005 reference period as depicted by (a, c) the CMIP5 and (b, d) CMIP6 ensemble means. They represent the differences between the mean precipitation averaged over the 2071–2098 and 1980–2005 periods for (a, b) winter and (c, d) summer.

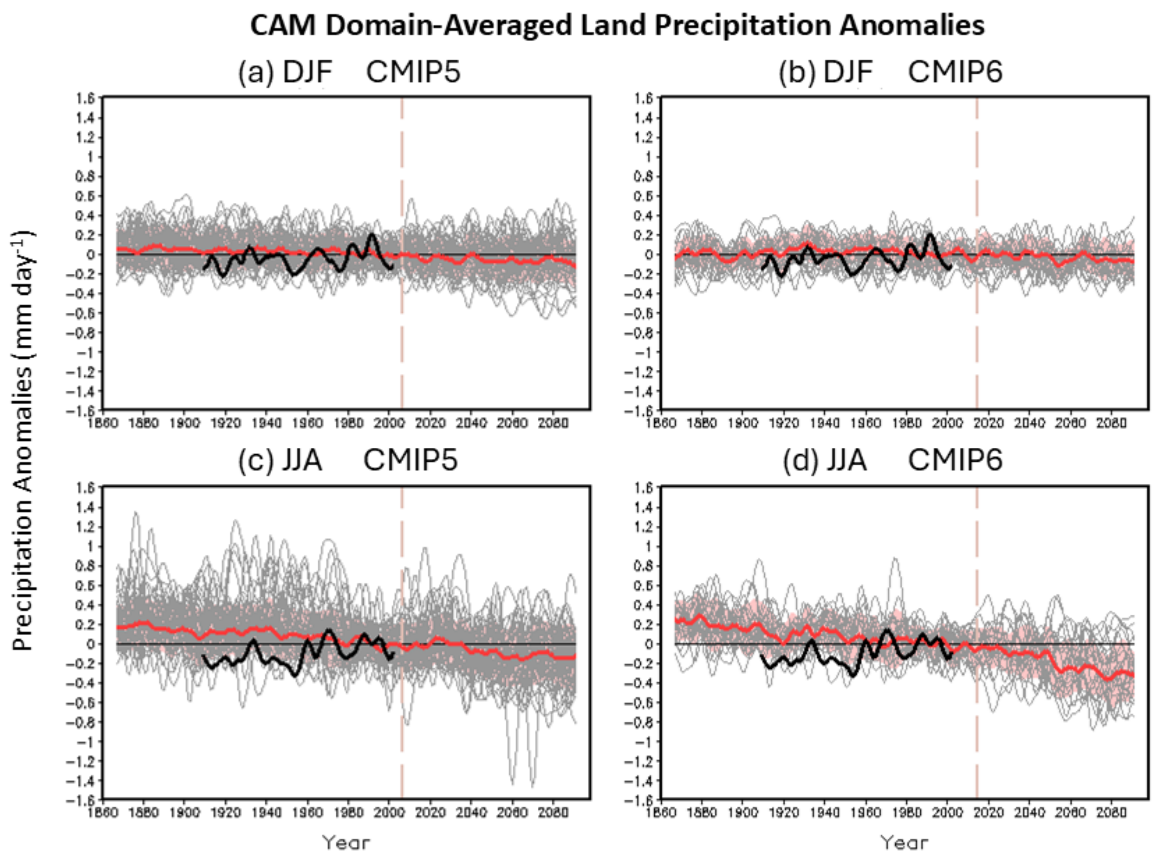

Figure 7.6 CAM domain-averaged precipitation anomalies (units: mm day^{-1}) relative to the 1980–2005 climatology, from 1865 to 2095 for (a, b) winter and (c, d) summer. Panels (a) and (c) show the CMIP5 MME means (red lines), while panels (b) and (d) display the CMIP6 MME means (red lines). CRU observations are represented by black lines. Gray lines indicate individual model members, and pink shading represents one standard deviation of the inter-member spread around the MME means.

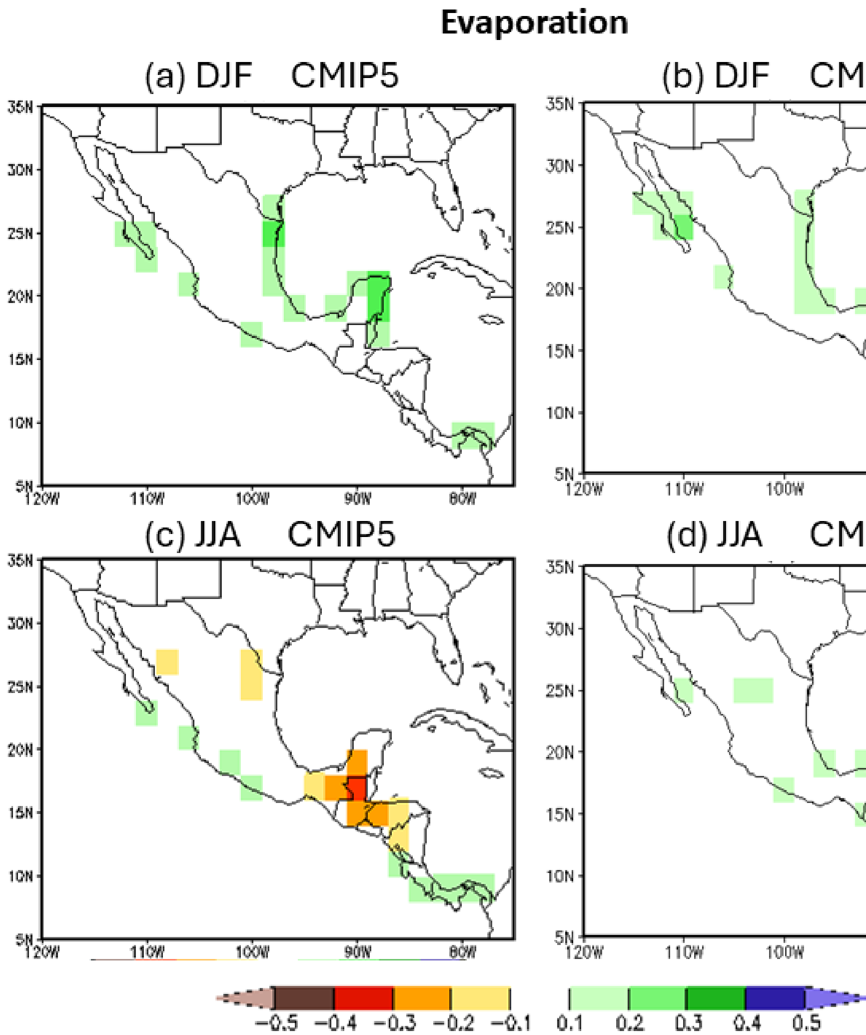

Figure 7.7 Projections of evaporation change (units: mm day^{-1}) over the 2071–2098 period relative to the 1980–2005 reference period as depicted by (a, c) the CMIP5 and (b, d) CMIP6 ensemble means. They represent the differences between the mean evaporation averaged over the 2071–2098 and 1980–2005 periods for (a, b) winter and (c, d) summer.

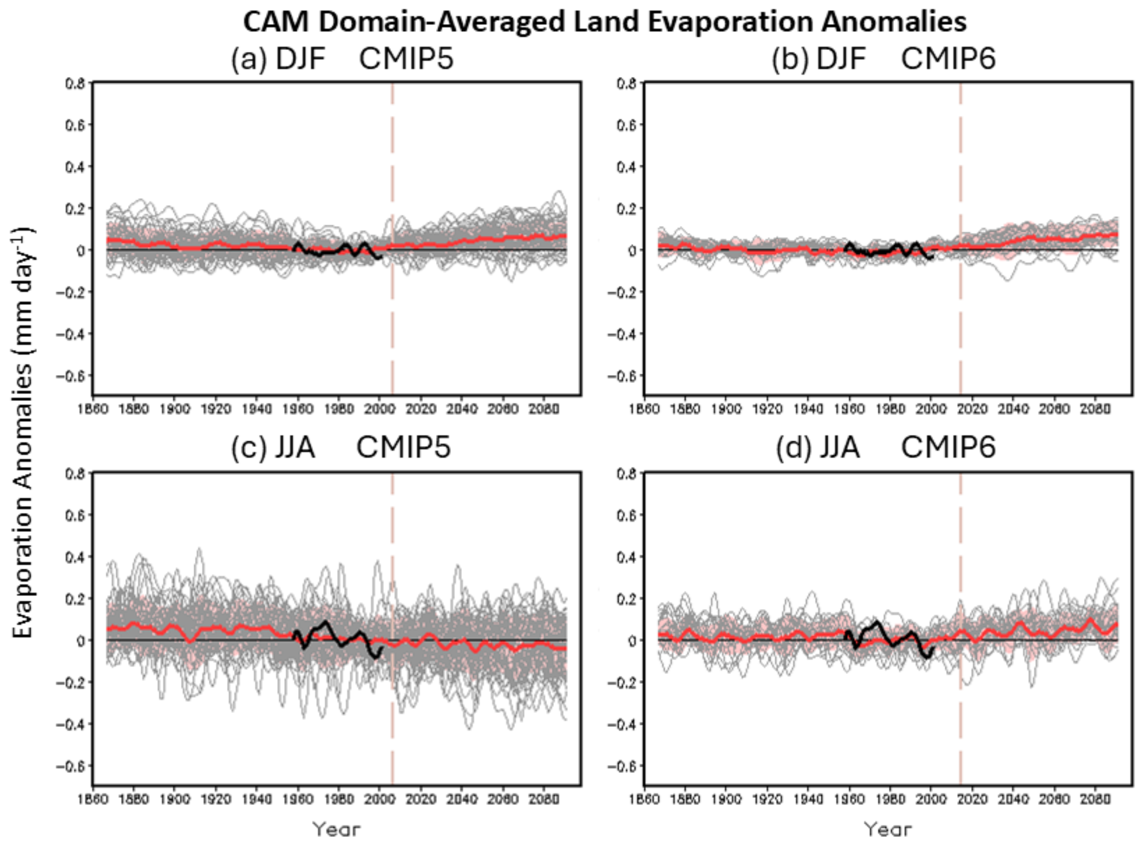

Figure 7.8 CAM domain-averaged evaporation anomalies (units: mm day^{-1}) relative to the 1980–2005 climatology, from 1865 to 2095 for (a, b) winter and (c, d) summer. Panels (a) and (c) show the CMIP5 MME means (red lines), while panels (b) and (d) display the CMIP6 MME means (red lines). CNRM observations are represented by black lines. Gray lines indicate individual model members, and pink shading represents one standard deviation of the inter-member spread around the MME means.

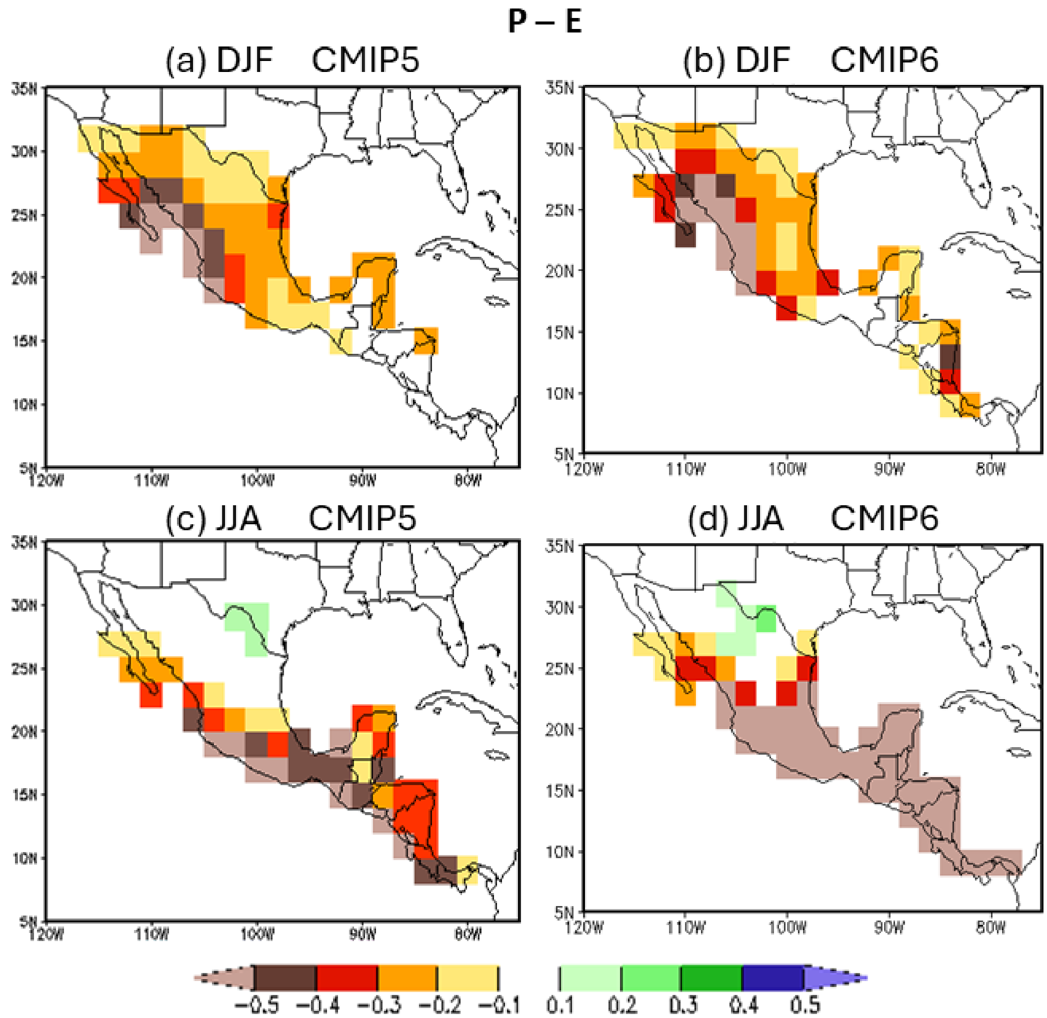

Figure 7.9 Projections of P–E change (units: mm day^{-1}) over the 2071–2098 period relative to the 1980–2005 reference period as depicted by (a, c) the CMIP5 and (b, d) CMIP6 ensemble means. They represent the differences between the mean P–E averaged over the 2071–2098 and 1980–2005 periods for (a, b) winter and (c, d) summer.

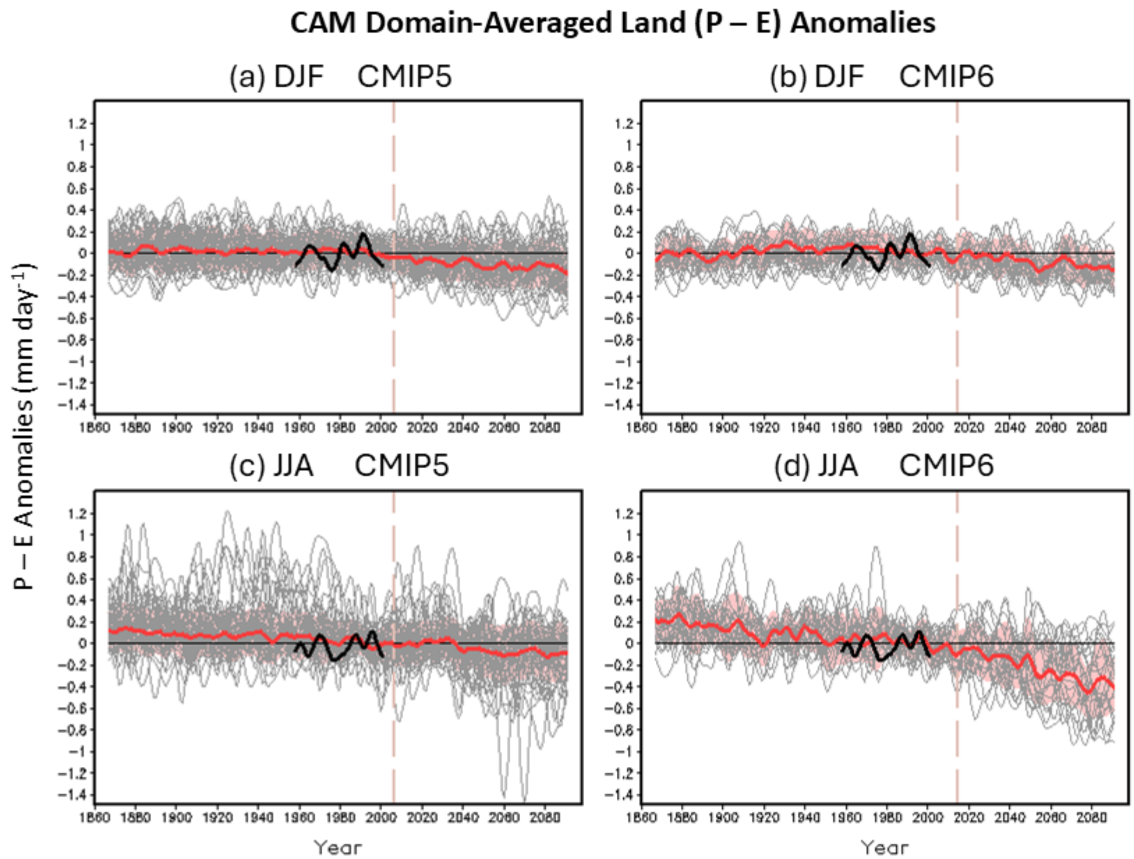

Figure 7.10 CAM domain-averaged P–E anomalies (units: mm day^{-1}) relative to the 1980–2005 climatology, from 1865 to 2095 for (a, b) winter and (c, d) summer. Panels (a) and (c) show the CMIP5 MME means (red lines), while panels (b) and (d) display the CMIP6 MME means (red lines). CUR/CNRM observations (precipitation/evaporation) are represented by black lines. Gray lines indicate individual model members, and pink shading represents one standard deviation of the inter-member spread around the MME means.

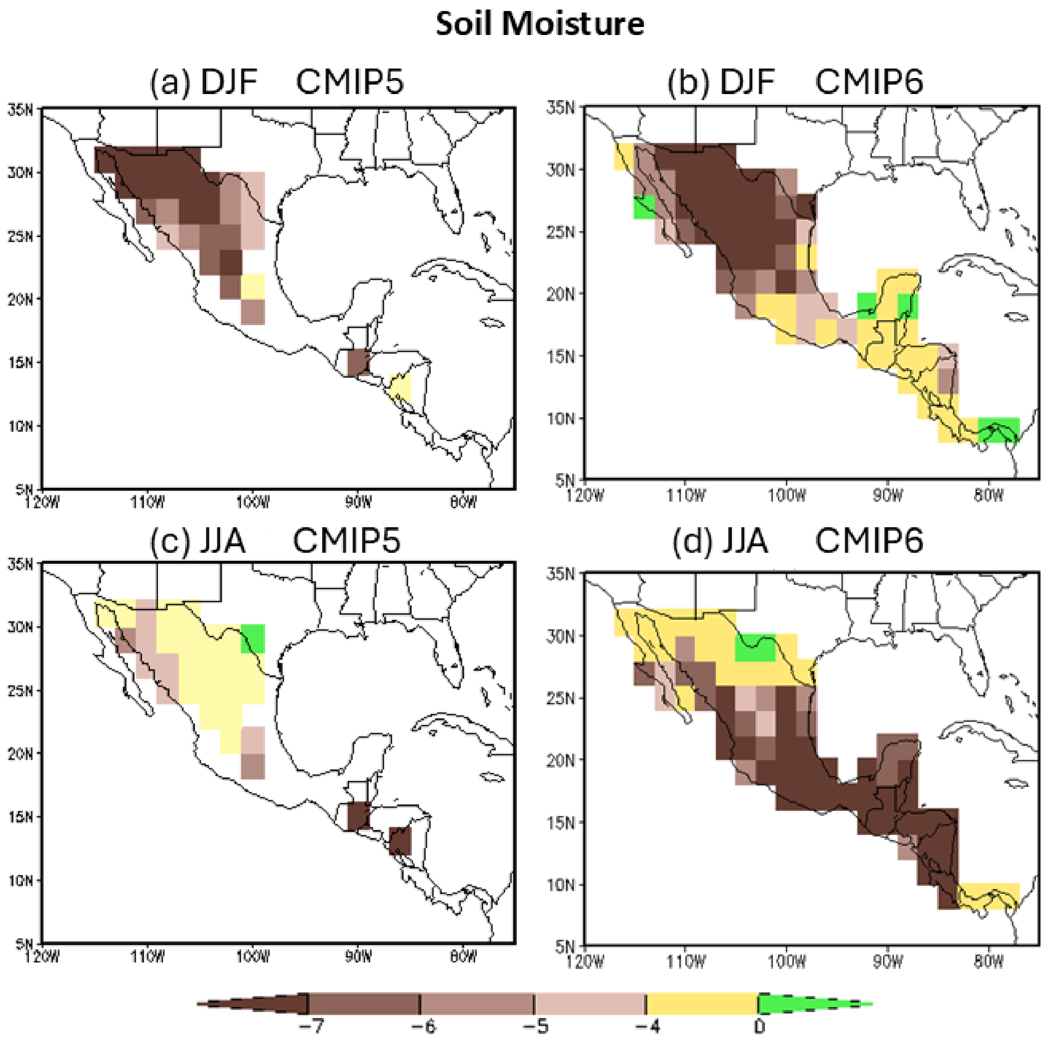

Figure 7.11 Projections of soil moisture change (units: %) over the 2071–2098 period relative to the 1980–2005 reference period as depicted by (a, c) the CMIP5 and (b, d) CMIP6 ensemble means. They represent the differences between the mean soil moisture averaged over the 2071–2098 and 1980–2005 periods for (a, b) winter and (c, d) summer.

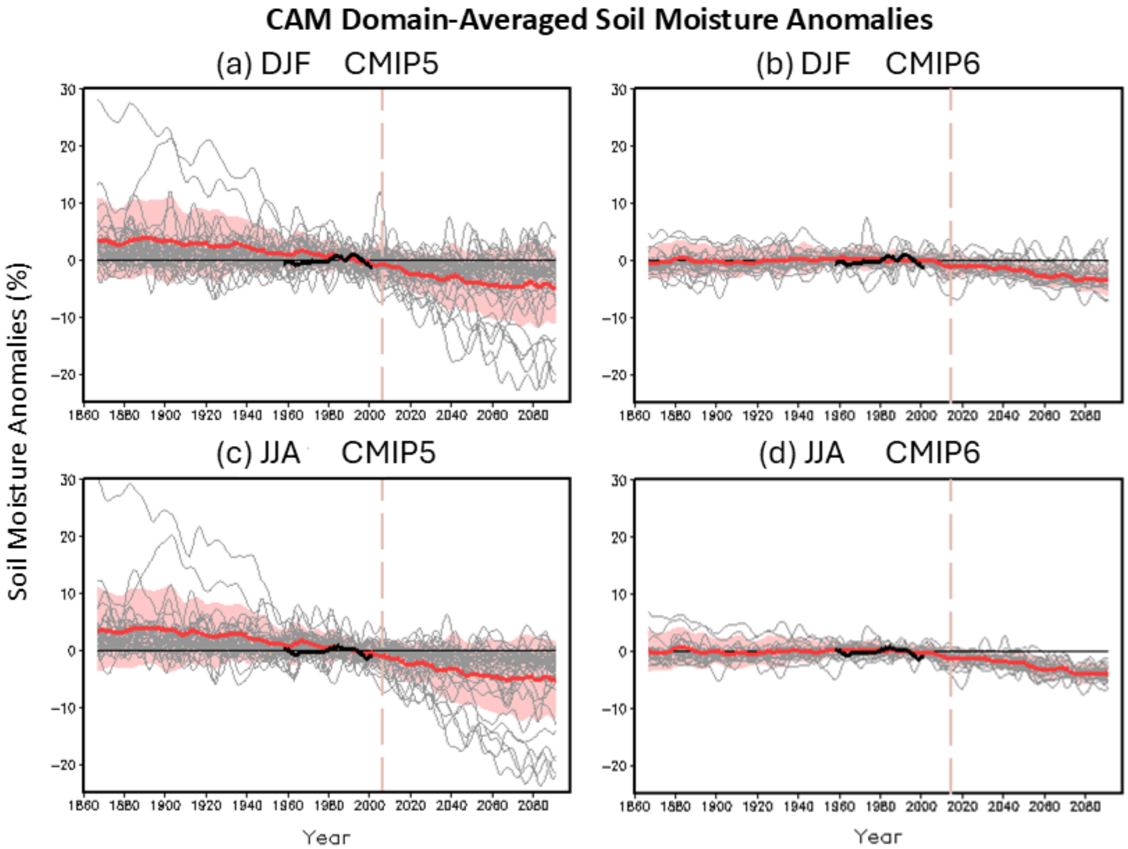

Figure 7.12 CAM domain-averaged relative total soil moisture anomalies (units: %) relative to the 1980–2005 climatology, from 1865 to 2095 for (a, b) winter and (c, d) summer. Panels (a) and (c) show the CMIP5 MME means (red lines), while panels (b) and (d) display the CMIP6 MME means (red lines). CNRM observations are represented by black lines. Gray lines indicate individual model members, and pink shading represents one standard deviation of the inter-member spread around the MME means.

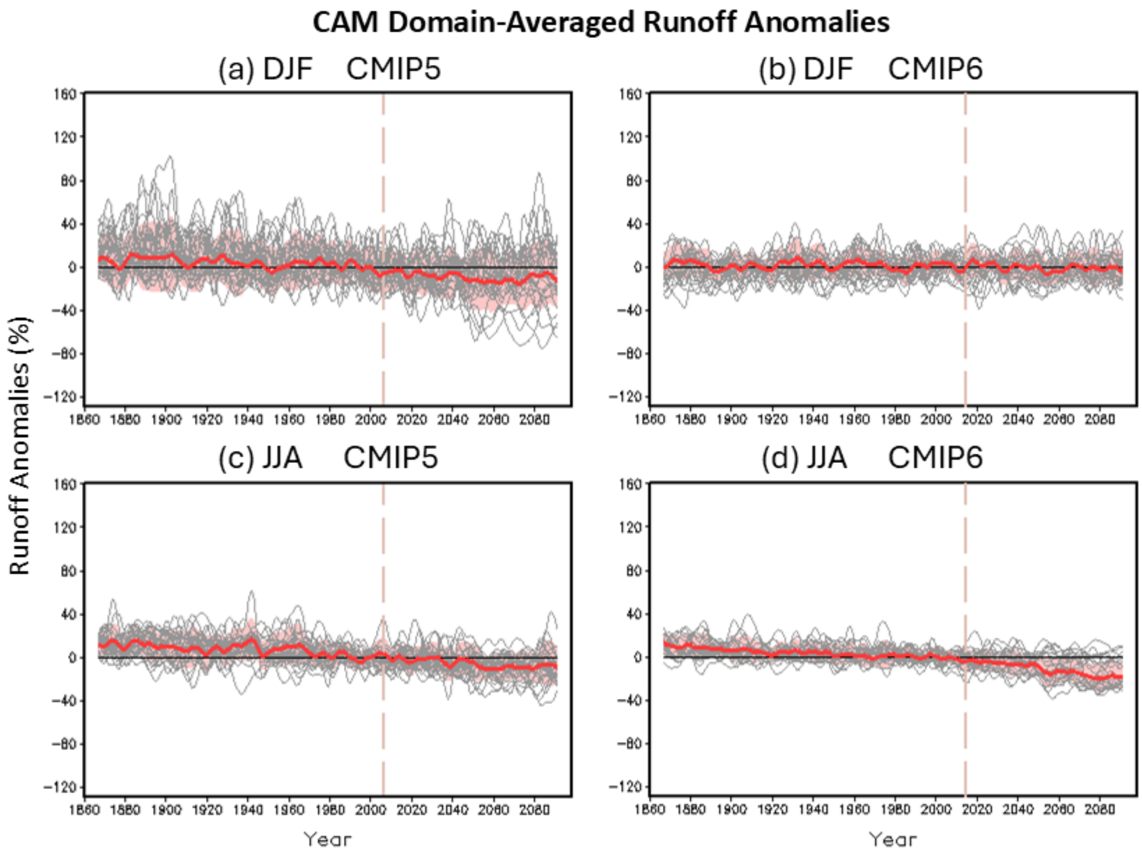

Figure 7.13 CAM domain-averaged total runoff anomalies (units: %) relative to the 1980–2005 climatology, from 1865 to 2095 for (a, b) winter and (c, d) summer. Panels (a) and (c) show the CMIP5 MME means (red lines), while panels (b) and (d) display the CMIP6 MME means (red lines). CNRM observations are represented by black lines. Gray lines indicate individual model members, and pink shading represents one standard deviation of the inter-member spread around the MME means.

Chapter 8: Conclusions and Future Work

This dissertation has explored the intricate relationships between tropical sea surface temperatures (SSTs) and precipitation in the Central America-Mexico (CAM) region, with a focus on both winter and summer seasons. Through extensive analysis of historical data, model simulations, and climate projections, several key findings have emerged that contribute to our understanding of regional climate variability, particularly under the influence of global warming. In this final chapter, we summarize the main conclusions and suggest directions for future research.

8.1 Key Findings

1. **Seasonal Precipitation and SST Relationships:** The study confirmed that both tropical Pacific and Atlantic SSTs significantly influence CAM precipitation patterns, with different dynamics at play during winter and summer. In the winter, ENSO-related SST variations in the Pacific Ocean are a key driver of precipitation variability, with La Niña conditions contributing to droughts in northern Mexico, and warming in the tropical Atlantic influencing precipitation in Central America. In the summer, tropical SSTs, especially warming in the Atlantic and Pacific Oceans, were identified as the primary drivers of precipitation, with ENSO events playing a secondary, but still important, role.
2. **Mid-Summer Drought (MSD) Trends:** The MSD, a prominent feature of CAM's seasonal cycle, was shown to be sensitive to both short-term ENSO fluctuations and long-term trends. The study highlighted that El Niño events tend to exacerbate the MSD, reducing rainfall and extending its duration, while La Niña conditions usually increase rainfall and shorten the MSD. Moreover, the recent trend towards a shortened MSD and

increased precipitation over the past few decades suggests a shift in regional climate dynamics that warrants further exploration.

3. **Impact of Global Warming on Precipitation and Hydrological Cycles:** The projected impacts of global warming on the CAM region were analyzed through simulations of future climate scenarios (RCP45/SSP245). The results indicate a warmer and drier future for CAM, with surface air temperature increases of 1.5–3°C and significant reductions in precipitation. These changes, coupled with alterations in evaporation, runoff, and soil moisture, suggest that the regional hydrological cycle will undergo significant adjustments, potentially leading to reduced water availability and exacerbating existing challenges related to water management, agriculture, and food security.
4. **Tropical SSTs as Predictors for Seasonal Precipitation:** The study demonstrated that tropical SSTs, particularly those in the Pacific and Atlantic Oceans, serve as valuable predictors for CAM seasonal precipitation. The application of statistical methods such as Singular Value Decomposition (SVD) has revealed robust patterns of covariability that could enhance the predictability of regional precipitation and provide critical information for seasonal forecasting.

8.2 Future Work

While this dissertation provides valuable insights into the relationships between tropical SSTs and CAM precipitation, several areas warrant further research:

1. **Long-Term Trends:** The observed shifts in the seasonal cycle, such as the shortening of the MSD, suggest regional climate changes in response to global warming. Future work should explore the causes of these changes and their links to climate processes like the multi-decadal SST variability in the Atlantic.

2. **Climate Modeling:** Advancing climate models to better capture the interactions between SSTs and regional precipitation is essential. High-resolution AMIP models would improve understanding of how SSTs influence CAM precipitation in a warming climate.
3. **Regional Feedback Mechanisms:** More research is needed to investigate feedback between precipitation, soil moisture, runoff, and evapotranspiration, especially under projected warming scenarios. Understanding these processes will be crucial for water availability projections and assessing climate risks.
4. **Regional Climate Variability:** Future studies should explore other climate drivers, such as the North Atlantic Oscillation (NAO) and various ENSO flavors, to better understand their role in shaping CAM precipitation patterns.
5. **Climate Change Impacts on Communities:** Finally, research should focus on the socio-economic impacts of changing precipitation and the hydrological cycle, especially for agriculture, water resources, and food security. Collaboration with local governments and organizations can help apply these findings to climate adaptation strategies.

8.3 Concluding Remarks

This dissertation has made significant strides in elucidating the relationships between tropical SSTs and CAM precipitation, offering insights that are essential for understanding regional climate variability and for improving the predictability of seasonal precipitation. The findings underscore the need for continued research on the role of SSTs in shaping regional climate dynamics, especially in light of ongoing global warming. By advancing our understanding of these complex interactions, we can better prepare for the challenges posed by a changing climate and ensure the resilience of communities in the CAM region.

Bibliography

Alessandri, A., M. D. Felice, N. Zeng, A. Mariotti, Y. Pan, A. Cherchi, J.-Y. Lee, B. Wang, K.-J. Ha, P. Ruti, V. Artale, 2014: Robust assessment of the expansion and retreat of Mediterranean climate in the 21st century. *Sci. Reports*, **4,** 7211.

Alkama R., B. Decharme, H. Douville, M. Becker, A. Cazenave, J. Sheffield, A. Voldoire, S. Tyteca, and P. Le Moigne, 2010: Global evaluation of the ISBA-TRIP continental hydrologic system. Part 1: A twofold constraint using GRACE Terrestrial Water Storage estimates and in-situ river discharges. *J. Hydrometeor.*, **11,** 583–600.

Angelo, P. J., 2022: Climate Change and Regional Instability in Central America. Prospects for Internal Disorder, Human Mobility, and Interstate Tensions. Council on Foreign Relations, Washington, DC, 47 pp.

Barrett, O.-L., 2019: Central America: climate, drought, migration and border. The Center for Climate and Security, 17 April 2019. [Available at https://climateandsecurity.org/2019/04/17/central-america-climate-drought-migration-and-the-border/]

Bateman, J., 2025: 2024 was the world's warmest year on record. NOAA, 10 January 2025. [Available at https://www.noaa.gov/news/2024-was-worlds-warmest-year-on-record]

Bhattacharya, T., J. C. H. Chiang, 2014: Spatial variability and mechanism underlying El Niño-induced droughts in Mexico. *Climate. Dyn.*, **43,** 3309–3326.

Bnamericans, 2016: Mexico to face severe drought in 2017, warns water authority. Bnamericas, 20 October 2016. [Available at https://www.bnamericas.com/en/news/mexico-to-face-severe-drought-in-2017-warns-water-authority]

Bretherton, C. S., C. Smith, J. M. Wallace, 1992: An intercomparison of methods for finding coupled patterns in climate data. *J. Climate*, **5,** 541–560.

Cavazos, T., S. Hastenrath, 1990: Convection and rainfall over Mexico and their modulation by the southern oscillation. *Int. J. Climatol.*, **10,** 377–386.

Chen, M, W. Shi, P. Xie, V. B. S. Silva, V. E. Kousky, R. W. Higgins, J. E. Janowiak, 2008: Assessing objective techniques for gauge-based analyses of global daily precipitation. *J. Geophys. Res. Atmos.*, **113,** D04110.

Chen, M., P. Xie, J. E. Janowiak, and P. A. Arkin, 2002: Global land precipitation: A 50-yr monthly analysis based on gauge observations. *J. Hydrometeor.*, **3,** 249–266.

Climate Reality, 2018: How is climate change affecting Mexico? The Climate Reality Project, 15 February 2018. [Available at https://www.climaterealityproject.org/blog/how-climate-change-affecting-mexico]

CPC, 2025: Historical El Niño/La Niña episodes (1950–present): Cold and warm episodes by season. NWS, CPC [Available at https://origin.cpc.ncep.noaa.gov/products/analysis_monitoring/ensostuff/ONI_v5.php]

Curtis, S., 2002: Interannual variability of the bimodal distribution of summertime rainfall over Central America and tropical storm activity in the far-eastern Pacific. *Climate Res.*, **22,** 141–146.

Curtis, S., D. W. Gamble, 2008: Regional variations of the Caribbean mid-summer drought. *Theor. Appl. Climatol.*, **94,** 25–34.

Douville, H., B. Decharme, A. Ribes, R. Alkama, J. Sheffield, 2012: Anthropogenic influence on multi-decadal changes in reconstructed global evapotranspiration. *Nature Climate Change*, doi: 10.1038/NCLIMATE 1632.

Driscoll, S., A. Bozzo, L. J. Gray, A. Robock, G. Stenchikov, 2012: Coupled Model Intercomparison Project 5 (CMIP5) simulations of climate following volcanic eruptions. *J. Geophys. Res.*, Doi:10.1029/2012JD017607.

Duchon, C. E., 1979: Lanczos filter in one and two dimensions. *J. Appl. Meteorol.*, **18,** 1016–1022.

Enfield, D. B., 1996: Relationship of inter-American rainfall to tropical Atlantic and Pacific SST variability. *Geophys. Res. Lett.*, **23,** 3305–3308.

Enfield, D. B., E. J. Alfaro, 1999: The dependence of Caribbean rainfall on the interaction of the tropical Atlantic and Pacific Oceans. *J. Climate*, **12,** 2093–2103.

Enfield, D. B., A. M. Mestas-Nuñez, and P.J. Trimble, 2001: The Atlantic multidecadal oscillation and its relationship to rainfall and river flows in the continental U.S. *Geophys. Res. Lett.*, **28,** 2077–2080.

Eyring, V., S. Bony, G. A. Meehl, C. A. Senior, B. Stevens, R. J. Stouffer, K. E. Taylor, 2016: Overview of the Coupled Model Intercomparison Project Phase 6 (CMIP6) experimental design and organization. *Geosci. Model Dev.*, **9,** 1937–1958.

Fion, F., 2018: Central America: drought, resulting crop losses threaten food security of two million people, UN warns. *UN News*, Economic Development, 24 August 2018. [Available at https://news.un.org/en/story/ 2018/08/1017712]

Fuentes-Franco R., E. Coppola, F. Giorgi, E. G. Pavia, G. T. Diro, and F. Graef, 2015: Inter-annual variability of precipitation over southern Mexico and Central America and its relationship to sea surface temperature from a set of future projections from CMIP5 GCMs and RegCM4 CORDEX simulations. *Climate Dyn.*, **45,** 425–440.

Gamble, D. W., D. B. Parnell, S. Curtis, 2008: Spatial variability of the Caribbean mid-summer drought and relation to north Atlantic high circulation. *Int. J. Climatol.*, **28,** 343–350.

García-Oliva, L. C., E. Pazos, 2021: The mid-summer drought spatial variability over Mesoamerica. *Atmósfera*, **34,** 227–232.

Giannini, A., Y. Kushnir, M. A. Cane, 2000: Interannual variability of Caribbean rainfall, ENSO, and the Atlantic Ocean. *J. Climate*, **13,** 297–311.

Handoh, I. C., A. J. Matthews, G. R. Bigg, and D. P. Stevens, 2006: Interannual variability of the tropical Atlantic independent of and associated with ENSO: Part 1. The north tropical Atlantic. *Int. J. Climatol.*, **26,** 1937–1956.

Hidalgo, H. G., J. A. Amador, E. J. Alfaro, B. Quesada, 2013: Hydrological climate change projections for Central America. *J. Hydrol.*, **495,** 94–112.

Huang, B., and Coauthors, 2017: Extended Reconstructed Sea Surface Temperature, Version 5 (ERSSTv5): Upgrades, validations, and intercomparisons. *J. Climate*, **30,** 8179–8205.

Huang, B., C. Liu, V. Banzon, E. Freeman, G. Graham, B. Hankins, T. Smith, H.-M. Zhang, 2021: Improvements of the daily optimum interpolation sea surface temperature (DOISST) version 2.1. *J. Climate*, **34,** 2923–2939.

Igini, M., 2024: 2024. Hottest year on record, marks 'Decade of deadly heat'. Earth.Org, 30 December 2024, [Available at https://earth.org/2024-hottest-year-on-record-marks-decade-of-deadly-heat/]

IPCC, 2007: Climate Change 2007: The Physical Science Basis, Contribution of Working Group I to the Third Assessment Report of the Intergovernmental Panel on Climate Change. Solomon S et al. Eds, Cambridge Univerity Press, Cambridge, 996 pp.

Jones, P. D., D. H. Lister, T. J. Osborn, C. Harpham, M. Salmon, and C. P. Morice, 2012: Hemispheric and large-scale land surface air temperature variations: An extensive revision and an update to 2010. *J. Geophys. Res.*, **117,** D05127.

Kalnay, E., and Coauthors, 1996: The NCEP–NCAR 40-Year Reanalysis Project. *Bull. Amer. Meteor. Soc.*, **77,** 437–471.

Kanamitsu, M., W. Ebisuzaki, J. Woollen, S.-K. Yang, J. J. Hnilo, M. Fiorino, G. L. Potter, 2002: NCEP–DOE AMIP-II Reanalysis (R-2). *Bull. Amer. Meteor. Soc.*, **83,** 1631–1643.

Karnauskas, K. B., A. J. Busalacchi, 2009: The role of SST in the East Pacific warm pool in the interannual variability of Central American rainfall. *J. Climate*, **22,** 2605–2623.

Kumar, A., M. P. Hoerling, 1995: Prospects and limitations of atmospheric GCM climate predictions. *Bull. Amer. Meteor. Soc.*, **76,** 335–345.

Linke, A., S. Leutert, J. Busby, M. Duque, M. Shawcroft, S. Brewer, 2023: Dry growing seasons predicted Central American migration to the US from 2012 to 2018. *Sci. Rep.*, **13**, 18400.

Lorenz, E. N., 1956: Empirical orthogonal functions and statistical weather prediction. *J. Atmos. Sci.*, **13,** 1–13.

Magana, V., J. A. Amador, S. Medina, 1999: The midsummer drought over Mexico and Central America. *J. Climate*, **12,** 1577–1588.

Magaña, V. O., J. L. Vázquez, J. L. Pérez, J. B. Pérez, 2003: Impact of El Niño on precipitation in Mexico. *Geofisica Internacional*, **42,** 313–330.

Mariotti, A., Y. Pan, N. Zeng, A. Alessandri, 2015: Long-term climate change in the Mediterranean region in the midst of decadal variability. *Climate Dyn.*, **44,** 1437–1456.

Maurer, E. P., I. T. Stewart, K. Joseph, H. G. Hidalgo, 2022: The Mesoamerican mid-summer drought: the impact of its definition on occurrences and recent changes. *Hydrol. Earth Syst. Sci.*, **26,** 1425–1437.

McGillivray, B., D. Salisbury, 2023: Climate change driven crop failure in Central America. University of Richmond. [Available at https://storymaps.arcgis.com/stories/e0d52fa5d69b42bc8ffd2040e4e9971f/print]

Mendez, M., V. Magana, 2010: Regional aspects of prolonged meteorological droughts over Mexico and Central America. *J. Climate,* **23,** 1175–1188.

Morice, C. P., J. J. Kennedy, N. A. Rayner, P. D. Jones, 2012: Quantifying uncertainties in global and regional temperature change using an ensemble of observational estimates: The HadCRUT4 dataset. *J. Geophys. Res.*, **117,** D08101.

OCHA, 2014: Drought in Central America, Situation Report No. 1. United Nations' Region Office for Latin America and the Caribbean, 10 December 2014. [Available at https://reliefweb.int/report/guatemala/drought-central-america-situation-report-no-01-december-10-2014]

Pan, Y., 2013: Mediterranean hydrological change projections for the 21st century assessed from CMIP5 simulations. M.S. Thesis, Department of Atmospheric and Oceanic Science, University of Maryland, 39 pp.

Pan, Y., N. Zeng, A. Mariotti, H. Wang, A. Kumar, R. L. Sanchez, B. Jha, 2018: Covariability of Central America/Mexico winter precipitation and tropical sea surface temperatures. *Climate Dyn.*, **50,** 4335–4346.

Pavia, E. G., F. Graef, J. Reyes, 2006: PDO–ENSO effects in the climate of Mexico. *J. Climate*, **19,** 6433–6438.

Rasmusson, E. M., T. H. Carpenter, 1982: Variations in tropical sea surface temperature and surface wind fields associated with the Southern Oscillation/El Niño. *Mon. Wea. Rev.*, **110,** 354–384.

Rayner, N. A., D. E. Parker, E. B. Horton, C. K. Folland, L. V. Alexander, D. P. Rowell, E. C. Kent, A. Kaplan, 2003: Global analysis of sea surface temperature, sea ice, and night marine air temperature since the late nineteenth century. *J. Geophys. Res.*, **108,** 4407.

Reynolds, R. W., N. A. Rayner, T. M. Smith, D. C. Stokes, W. Wang, 2002: An improved in situ and satellite SST analysis for climate. *J. Climate*, **15,** 1609–1625.

Robjhon, M., W. Thiaw, 2015: The 2014 Primera drought over Central America. *Sci. Tech. Infusion Climate Bull.*, NOAA NWS, 40th NOAA Annual Climate Diagnostics and Prediction Workshop, Denver, CO, 26–29 October 2015.

Rodriguez, O. R., 2012: North Mexico drought worst on record. *Huffington Post*

Saha, S., and Coauthors, 2010: The NCEP Climate Forecast System Reanalysis. *Bull. Amer. Meteor. Soc.*, **91,** 1015–1058.

Saha, S., and Coauthors, 2014: The NCEP Climate Forecast System Version 2. *J. Climate*, **27,** 2185–2208.

Salazar, F., O. R. Rodriguez, 2011: Mexico drought is worst in 70 years. SFGate, 3 December 2011. [Available at https://www.sfgate.com/world/article/Mexico-drought-is-worst-in-70-years-2345008.php]

Seager, R., M. Ting, M. Davis, M. Cane, N. Naik, J. Nakamura, C. Li, E. Cook, D. W. Stahle, 2009: Mexican drought: an observational modeling and tree ring study of variability and climate change. *Atmosfera*, **22,** 1–31.

Small, R. J. O., S. P. de Szoeke, S.-P. Xie, 2007: The Central American midsummer drought: Regional aspects and large-scale forcing. *J. Climate*, **20,** 4853–4873.

Snedecor, G. W., W. G. Cochran, 1989: Statistical Methods, 8 ed. Iowa State Univ. Press, pp503.

Steffens, G., 2018: Changing climate forces desperate Guatemalans to migrate. National Geographic, 23 October 2018. [Available at https://www.nationalgeographic.com/environment/2018/10/drought-climate-change-force-guatemalans-migrate-to-us/]

Stewart, I. T., E. P. Maurer, K. Stahl, K. Joseph, 2022: Recent evidence for warmer and drier growing seasons in climate sensitive regions of Central America from multiple global datasets. *Internatl. J. Climatol.*, **42,** 1399–1417.

Taylor, K. E, R. J. Stouffer, G. A. Meehl, 2012: An overview of the CMIP5 and the experiment design. *Bull. Amer. Meteor. Soc.*, **93,** 485–498.

Terray, P., S. Masson, C. Prodhomme, M. K. Roxy, K. P. Sooraj, 2016: Impacts of Indian and Atlantic oceans on ENSO in a comprehensive modeling framework. *Climate Dyn.*, **46,** 2507–2533.

Thiem, H., 2024: Multi-year drought and heat waves across Mexico in 2024. NOAA Climate.Gov. [Available at https://www.climate.gov/news-features/event-tracker/multi-year-drought-and-heat-waves-across-mexico-2024]

Ting, M., Y. Kushnir, R. Seager, and C. Li, 2011: Robust features of Atlantic multi-decadal variability and its climate impacts. *Geophys. Res. Lett.*, **38,** L17705, doi:10.1029/2011GL048712.

UNDRR, 2024: Central America drought, 2023 – Forensic analysis., United Nations Office for Disaster Risk Reduction, 12 September 2024. [Available at https://www.undrr.org/resource/central-america-drought-2023-forensic-analysis]

Wagner, J., E. R. Mega, S. Sengupta, 2024: Mexico City has long thirsted for water. The crisis is worsening. The New York Times, 18 May 2024. [Available at https://www.nytimes.com/2024/05/18/world/americas/mexico-city-water.html

Wallace, J. M., C. Smith, C. S. Bretherton, 1992: Singular value decomposition of wintertime sea surface temperature and 500-mb height anomalies. *J. Climate,* **5,** 561–576.

Wang, H., A. Kumar, W. Wang, 2013: Characteristics of subsurface ocean response to ENSO assessed from simulations with the NCEP Climate Forecast System. *J. Climate*, **26,** 8065–8083.

Wang, H., M. Ting, M. Ji, 1999: Prediction of seasonal mean United States precipitation based on El Niño sea surface temperatures. *Geophys. Res. Lett.*, **26,** 1341–1344.

Wilks, D. S., 1995: Statistical Methods in the Atmospheric Sciences. Academic Press, 467 pp.

WMO, 2025: WMO confirms 2024 as warmest year on record at about 1.55 °C above pre-industrial level. World Meteorological Organization, 10 January 2025. [Available at https://wmo.int/

news/media-centre/wmo-confirms-2024-warmest-year-record-about-155degc-above-pre-industrial-level]

Wright, K. T., and Coauthors, 2022: Precipitation in northeast Mexico primarily controlled by the relative warming of Atlantic SSTs. *Geophys. Res. Lett.*, **49,** e2022GL098186.

Xue, Y., M. Chen, A. Kumar, Z.-Z. Hu, W. Wang, 2023: Prediction skill and bias of tropical Pacific sea surface temperatures in the NCEP Climate Forecast System version 2. *J. Climate*, **26,** 5358–5378.

Zhao, Z., M. Han, K. Yang, N. J. Holbrook, 2023: Signatures of midsummer droughts over Central America and Mexico. *Climate Dyn.*, **60,** 3523–3542.

Zhu, J., B. Huang, A. Kumar, J. L. Kinter III, 2015: Seasonality in prediction skill and predictable pattern of tropical Indian Ocean SST. *J. Climate*, **28,** 7962–7984.